AD-A033 729 TRW DEFENSE AND SPACE SYSTEMS GROUP REDONDO BEACH CAL--ETC F/G 10/2
STUDY ON ELECTROFLUID DYNAMIC POWER GENERATION.(U)
JUL 76 M N HUBERMAN, H SHELTON, W KRIEVE F33615-75-C-4085
UNCLASSIFIED AFAPL-TR-76-31 NL

1 OF 2
AD A033729

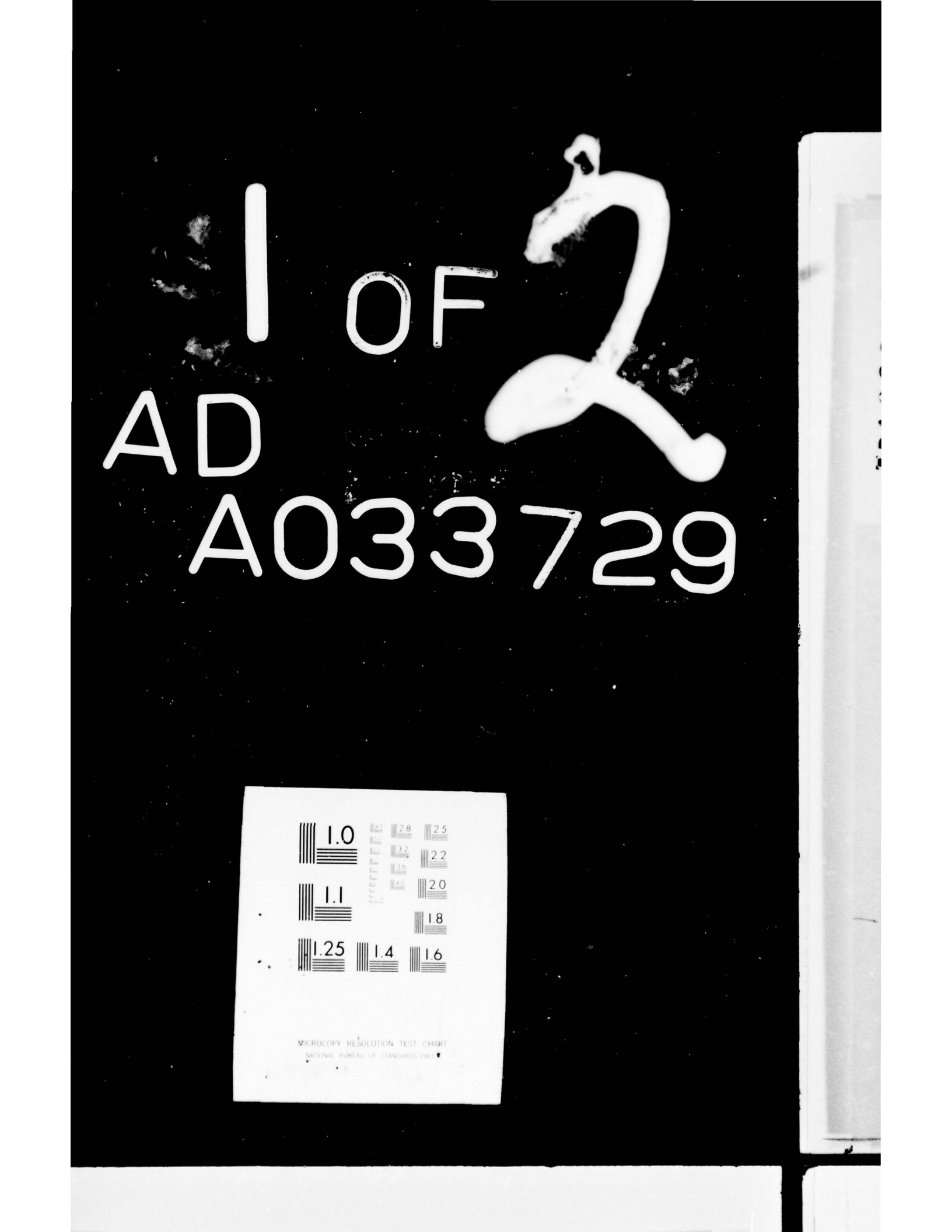
1 OF 2
AD
A033729
1.0
1.1
1.25
1.4
1.6
2.8
3.2
3.6
4.0
2.5
2.2
2.0
1.8
MICROCOPY RESOLUTION TEST CHART
NATIONAL BUREAU OF STANDARDS-1963-A

ADA033729

AFAPL-TR-76-31

(12)

STUDY OF ELECTROFLUID DYNAMIC POWER GENERATION

TRW SPACE AND DEFENSE SYSTEMS
PROPULSION AND COMBUSTION SYSTEM DEPT.
ONE SPACE PARK – REDONDO BEACH – CALIF. 90278

409 979

JULY 1976

TECHNICAL REPORT AFAPL-TR-76-31
FINAL REPORT FOR PERIOD 23 APRIL 1973 - 23 JANUARY 1976

DDC
RECEIVED
DEC 14 1976
A

Approved for public release; distribution unlimited

AIR FORCE AERO-PROPULSION LABORATORY
AIR FORCE WRIGHT AERONAUTICAL LABORATORIES
AIR FORCE SYSTEMS COMMAND
WRIGHT-PATTERSON AIR FORCE BASE, OHIO 45433

NOTICE

When Government drawings, specifications, or other data are used for any purpose other than in connection with a definitely related Government procurement operation, the United States Government thereby incurs no responsibility nor any obligation whatsoever; and the fact that the government may have formulated, furnished, or in any way supplied the said drawings, specifications, or other data, is not to be regarded by implication or otherwise as in any manner licensing the holder or any other person or corporation, or conveying any rights or permission to manufacture, use, or sell any patented invention that may in any way be related thereto.

This final report was submitted by TRW Space and Defense Systems, under Contract F33615-73-C-4085. The effort was sponsored by the Air Force Aero Propulsion Laboratory, Air Force Systems Command, Wright-Patterson AFB, Ohio under Project 7116, Task 01 and Work Unit 66 with Maurice O. Lawson, POP, Project Engineer In-Charge. Marshall N. Huberman of TRW Systems was technically responsible for the work. The TRW Project Team was:

M. N. Huberman	Program Manager
H. Shelton	Channel Geometry and Electrical Breakdown
W. F. Krieve	Charged Droplet Formation
C. L. Dailey	Analysis - Fluid Dynamics

This report has been reviewed by the Information Office, (ASD/OIP) and is releasable to the National Technical Information Service (NTIS). At NTIS, it will be available to the general public, including foreign nations.

This technical report has been reviewed and is approved for publication.

Maurice O. Lawson

MAURICE O. LAWSON
Project Engineer

FOR THE COMMANDER

Philip E. Stover

PHILIP E. STOVER
Chief
Power Distribution Branch

Copies of this report should not be returned unless return is required by security considerations, contractual obligations, or notice on a specific document.

AIR FORCE - 29 NOVEMBER 76 - 200

SECURITY CLASSIFICATION OF THIS PAGE (When Data Entered)

REPORT DOCUMENTATION PAGE

READ INSTRUCTIONS BEFORE COMPLETING FORM

1. REPORT NUMBER: AFAPL-TR-76-31	2. GOVT ACCESSION NO.
3. RECIPIENT'S CATALOG NUMBER	
4. TITLE (and Subtitle): STUDY ON ELECTROFLUID DYNAMIC POWER GENERATION.	5. TYPE OF REPORT & PERIOD COVERED: Final Technical Report, 23 Apr 1973-23 Jan 1976
6. PERFORMING ORG. REPORT NUMBER	
7. AUTHOR(s): M.N. Huberman, H. Shelton, W. Krieve C.L. Dailey	8. CONTRACT OR GRANT NUMBER(s): F33615-73-C-4085
9. PERFORMING ORGANIZATION NAME AND ADDRESS: TRW Systems gives address not One Space Park, Redondo Beach, California 90278	10. PROGRAM ELEMENT, PROJECT, TASK AREA & WORK UNIT NUMBERS: 61102F
11. CONTROLLING OFFICE NAME AND ADDRESS: Air Force Aero Propulsion Laboratory, Air Force Systems Command, Wright-Patterson AFB, Ohio 45433	12. REPORT DATE: July 1976 13. NUMBER OF PAGES: 115
14. MONITORING AGENCY NAME & ADDRESS (if different from Controlling Office): 116p.	15. SECURITY CLASS. (of this report): Unclassified 15a. DECLASSIFICATION/DOWNGRADING SCHEDULE

16. DISTRIBUTION STATEMENT (of this Report)

Approved for public release - distribution unlimited

7116 01

17. DISTRIBUTION STATEMENT (of the abstract entered in Block 20, if different from Report)

18. SUPPLEMENTARY NOTES

19. KEY WORDS (Continue on reverse side if necessary and identify by block number)

Energy Conversion
Electrofluid Dynamic Energy Conversion
Colloid Nucleation
Gas Breakdown
High Voltage

20. ABSTRACT (Continue on reverse side if necessary and identify by block number)

A three-year program to develop and advance Electrofluid Dynamic (EFD) Power Generation technology is described. A range of axisymetric EFD channel sizes from 1/12 inch operating with inlet pressures of 700 psig to the 1/48 inch channel designed to operate with 3000 psig were experimentally studied. Failure of gas-breakdown scaling laws prevented the designed 70 watts from being achieved with the small sizes at high pressure. Experimental work on the high voltage breakdown of high pressure gases including air, Hydrogen,

DD FORM 1 JAN 73 1473 EDITION OF 1 NOV 65 IS OBSOLETE

SECURITY CLASSIFICATION OF THIS PAGE (When Data Entered)

409 979 LB

SECURITY CLASSIFICATION OF THIS PAGE(When Data Entered)

10 to the 8th power

20.

SF_6, Argon, Nitrogen CO_2, and mixtures using various Freons shows a degradation of anticipated strength at about 10^8 V/M. Theoretical analyses and experimental measurements have been made on the droplet size and density in EFD generators using humid air for EFD channel sizes from 1/4 inch to 1/48 inch. Analyses also include nucleation and growth of Mercury and steam. A preliminary design study of the short duration airborne 6 MW power conversion system and a long duration 1 KW and 100 KW ground based system using EFD is included.

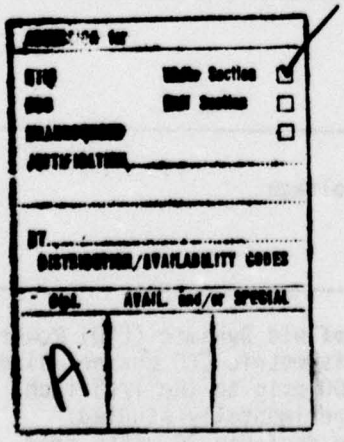

SECURITY CLASSIFICATION OF THIS PAGE(When Data Entered)

TABLE OF CONTENTS

SECTION		PAGE
I	INTRODUCTION	1
	1. Electrofluid-Dynamic (EFD) Power Generation	1
	a. Charge Carrier	1
	b. Conversion of Enthalpy into Electric Energy	1
	c. Gas Breakdown Strength	1
	2. Axisymmetric Generator with Recirculating Flow	2
	a. Gas Flow	2
	b. Dimensions	4
	3. Aim of the Study	4
	a. Experimental Generator Study	4
	b. Experimental and Analytical Study of Charged Droplets	5
	c. Gas Breakdown Experiments	5
	d. EFD Generating Systems Analysis	5
	4. Structure of Report	5
II	EXPERIMENTAL GENERATOR STUDY	7
	1. Experimental Apparatus	7
	2. 1/12 Inch EFD Generator Data	10
	3. Typical Data for Smaller Geometries	10
	a. Maximum Kinetic Efficiency, Maximum Power, and Maximum Enthalpy Removal	15
	b. Small Primary Areas and High Primary Mach Numbers	16
	4. Noteworthy Generator Considerations	16
	a. EMI Noise	16
	b. Humidity Measurement	16
	c. Nozzle Mounting and Contour	17
	d. Alignment	17
	e. Insulator	17
III	EXPERIMENTAL AND ANALYTICAL STUDY OF CHARGED DROPLETS	23
	1. Description of Experimental Apparatus	23
	2. System Calibration and Equations used to Determine Drop Size and Density	28
	3. Experimental Results	30
	4. Mach Number Profiles from Pitot Tube Scans	33
	5. Electrohydrodynamic Spraying of Water Droplets	33
	a. Analysis	33
	b. Experiments	38
	6. Charged Particle Production Analysis	40
	a. Condensation Process	40
	b. Kinetic Conditions - Nucleation and Growth Rates	45

TABLE OF CONTENTS (Continued)

SECTION PAGE

III EXPERIMENTAL AND ANALYTICAL STUDY OF CHARGED DROPLETS (continued)

7. Expansion of Steam..... 57
8. Conclusions..... 63

IV GAS BREAKDOWN EXPERIMENTS..... 65

1. Experimental Apparatus..... 65
2. General Qualitative Observations..... 65
3. Data - Breakdown Strength of Various High Pressure Gases..... 65
   a. Air with No Additive..... 68
   b. Hydrogen..... 68
   c. Freon 13 and Freon 21 - Nitrogen Mixture..... 68
   d. Carbon Dioxide..... 68
   e. Sulfur-Hexafluoride and SF_6 - Air Mixtures..... 68
   f. Argon, Argon-Oxygen, and Argon-SF_6..... 72
   g. Nitrogen-Oxygen Mixtures..... 72
   h. Steam..... 76
4. EFD Generator Improvement by Gas Selection..... 76

V EFD GENERATING SYSTEMS..... 79

1. Airborne High Power and High Energy EFD Systems..... 79
   a. Pump Power..... 79
   b. Choice of Operating Parameters..... 80
   c. Weight of Fluid..... 80
   d. Pressure Vessel..... 81
   e. Heat Addition and Gas Control..... 82
   f. Water to Cool and Humidify Secondary Flow..... 82
   g. Stacked EFD Cylindrical Generator..... 82
   h. Overall System - Weight and Volume..... 89
2. Ground Based EFD Generator..... 89
   a. Parameters Selected and Assumptions..... 89
   b. Description of Generator..... 90
   c. Unattended Continuous Operation for 1 Year..... 90
   d. 100 kW Ground-Package for 6 Month Operation..... 92
3. Analysis Involving Mixing of Two Fluid Streams..... 94
   a. Constant Area Mixing Relations..... 94
   b. Generator Efficiency..... 97
   c. Analysis of Experiments..... 98
   d. Performance Calculation Procedure..... 101
   e. Calculated Efficiencies for a Mercury/Hydrogen System..... 104
   f. Calculated Efficiencies for a Single Fluid System..... 106

VI CONCLUSIONS..... 109

LIST OF EFD REPORTS

BIBLIOGRAPHY

LIST OF ILLUSTRATIONS

FIGURE		PAGE
1	Scale Drawing of the AX1 - Symmetrical EFD Generator	3
2a	High Voltage Termination Sphere Mounting	8
2b	Photograph of EFD Test Console	8
3	Photograph of Humidifier Systems	9
4	Operating Characteristics at 95 Percent RH. 82 Watts Output Power	11
5	Operating Characteristics of 1/17 Inch EFD Rig Over Range of Pressures	12
6	1/24 Inch Channel Operation Showing Degraded Performance Due to Needle Erosion	13
7	1/24 Inch Channel Output Power versus Primary Pressure	14
8	Collector Current versus Voltage for the 1/48 Inch Channel at 1/2 Design Pressure	15
9	High Pressure Water Flow-Meter	18
10	High Temperature, High Pressure, Dew-Point Sight-Glass	19
11	Nozzle Modification to Allow Easy Replacement of Reworked Pieces.	20
12	Insulator Designed to Eliminate Surface Breakdown at High Temperature and Humidity	21
13	Charged Droplet Experiment	24
14a	Light Trap	25
14b	Pressure Probe and Traversing Head	25
15a	Photograph of 1/4 Inch Experimental Channel	26
15b	Laser Beam Scattering Experimental Apparatus	26
16a	Primary Gas Thermal and Equilibrating Bath and Heat Exchangers	27
16b	Experimental Channel Humidifier System	27
17	Scattered Light Intensity Scan Profiles Across the Channel Colloid Beam	30
18	Scatter Light Intensity Scan Profile with and without Corona at Low Relative Humidity	32
19	Air Flow Stream Mach No. and Simultaneous Tertiary Pressure Profiles with a Primary Mach No. of 1.05 and No Corona Pin	34
20	Air Flow Stream Mach No. and Simultaneous Tertiary Pressure Profiles with a Primary Mach No. of 1.08 and No Corona Pin	35
21	Air Flow Stream Mach No. and Simultaneous Tertiary Pressure Profiles with a Primary Mach No. of 1.05 and the Corona Pin	36
22	Air Flow Stream Mach No. and Simultaneous Tertiary Pressure Profiles with a Primary Mach No. of 1.08 and the Corona Pin	37

LIST OF ILLUSTRATIONS (Continued)

FIGURE		PAGE
23	Relationship of Charge, Radius, Charge-to-Mass Ratio, Surface Electric Field Strength, and Rayleigh Limit for Water Droplets..	39
24	Current of Electrohydrodynamically Sprayed Water Droplets versus Retarding Collector Voltage.....	41
25	Water Droplet Vapor Pressure as a Function of Droplet Radius....	43
26	Critical Condensation Pressure for Water.....	46
27	Expansion of Near Critical Water Vapor.....	47
28	Condensation Kinetics in a 1/12 Inch Channel with Gradual Expansion (80% Relative Humidity).....	52
29	Condensation Kinetics in a 1/24 Inch Channel.....	53
30	Computer Predicted Drop Size and Density at 245°F.....	54
31	Condensation Characteristics of Water at 70°F, Relative Humidity 80% and Mach 1.24.....	55
32	Condensation Characteristics of Water at 70°F, Relative Humidity 40.3% and Mach 1.24.....	56
33a	Partially Assembled Gas Breakdown Cell.....	66
33b	Fully Assembled Gas Breakdown Cell.....	66
34	Gas Breakdown Cell Design.....	67
35	Breakdown Voltage in Air versus Pressure for Two Pd Products....	69
36	Repeat V_{Br} versus P After Cleaning Electrodes.....	70
37	Breakdown Characteristics of Nitrogen, Doped Nitrogen and Freon 13 for a Spacing of ~ 0.020".....	71
38	Breakdown Voltages in Sulfur Hexafluoride (SF_6).....	72
39	Breakdown Voltages in High Pressure Air with Small Percentages of SF_6.....	73
40	Breakdown Voltage in High Pressure Argon with Various O_2, SF_6 Mixtures.....	74
41	Breakdown Voltage of High Pressure N_2-O_2 Mixtures.....	75
42	Breakdown Voltage of Steam and Air versus Pressure.....	77
43	Detail of the Clamping Seal Between the Metal Dome and the Cylindrical Plastic Tank.....	83
44	Schematic of the 6MW Airborne Power System Using an EFD Generator Operating with Hydrogen.....	84
45	Single Primary Nozzle and Corona Disc.....	86
46	Sketch Showing Arrangement of the Electrodes and the Flow Paths..	87
47	Sketch of the Assembled 6/8 MW EFD Generator.....	88

LIST OF ILLUSTRATIONS (Continued)

FIGURE		PAGE
48	Sketch of 1 KW EFD Generator using Mercury Rankine Cycle Driving hydrogen.....	91
49	Auxiliary Electric System to Charge Battery Supply, Extractor Power, and Power the Mercury Pump.....	93
50	Stations in a Constant Area Mixing Channel.....	94
51	Mach Number 2 Mercury Driver, Hydrogen Driven Flow, for Two Area Ratios (T_{s1} = 1150°K, T_{s2} = 320°K).....	105
52	Performance of Single Fluid Generator (A_1/A_2 = 0.01, γ =1.4)....	107
53	Performance of Single Fluid Generator (A_1/A_2 = 0.02, γ =1.4)....	108

SECTION I

INTRODUCTION

This section introduces the concept of electrofluid-dynamic power generation and describes the geometry of the generator used in this study.

1. ELECTROFLUID-DYNAMIC (EFD) POWER GENERATION

An EFD generator is an electrostatic generator similar to the better known Van de Graaff generator. The electric charge is imbedded in a gas flow that pushes it against an electric field, and, when collected, furnishes a current at a high voltage. The braking action on the charges slows down the gas converting its kinetic energy directly into electrical energy. The EFD generator, in common with all electrostatic generators, creates very high voltages. The equipment used in this study operated at approximately 200 kV, although higher or lower voltages could be obtained by altering the geometry.

a. Charge Carrier

The most manageable charge carrier for an EFD generator is a small colloid particle containing one electronic charge. In this study the particle is a water droplet of radius about 10^{-8} meter (about 10^{5} molecules) to which is attached an electron from a corona discharge at a needle point. These particles have low mobility[a] so that they are effectively imbedded in the gas, and move in with little slip. Thus a single charge is pushed by the gas molecules near it in addition to the particle to which it is attached. The water droplets are generated by condensing water vapor in the supersonic expansion of humid air.

b. Conversion of Enthalpy into Electric Energy

The thermal energy of a gas is converted into kinetic energy by expansion through a nozzle, with a corresponding drop in temperature and pressure. When charged water droplets are added to the gas an electric current is carried to a collector at high negative voltage. In this way, the enthalpy stored in the gas is converted first to kinetic energy then to electrical energy.

c. Gas Breakdown Strength

Electrical breakdown through the gas limits the operating voltage. High pressure operation is attractive because both the maximum voltage and the maximum current increase with increasing pressure so that the available electric power increases as the pressure squared while the gas kinetic energy is only proportional to the pressure. A factor of two pressure increase quadruples the power output while the kinetic energy only doubles. At the start of the program, air was used at a pressure of about 250 psig (approximately 17 atm) in the conversion region. The main thrust of the experimental

work was to find a better gas and to increase the operating pressure. This required that the experiments be performed within high pressure vessels.

2. AXISYMMETRIC GENERATOR WITH RECIRCULATING FLOW

Figure 1 is a 10:1 scale drawing of the electrodes in the generator that was used in this study. This generator is the outgrowth of many years of work at the Air Force Research Laboratories at Dayton, Ohio. One of two identical generators was supplied to TRW by the Air Force in order for TRW to proceed in parallel with the Air Force in-house program. All elements in Figure 1 are symmetrical about the central axis. The corona pin is in the center of a sonic nozzle through which high pressure air is expanded and accelerated up through the attractor towards the collector. The corona pin and primary nozzle are operated at ground potential while the attractor is at potentials ranging up to about +25 kV. The collector is operated at voltages up to about -200 kV and is attached to a cable that carries the high voltage current out of the pressure vessel.

a. Gas Flow

Humidified air is supplied to the primary nozzle at a pressure, P_p. An equal amount of air is removed from the generator at a lower secondary pressure, P_s ($P_s \approx 1/2\ P_p$). The region between the attractor and collector is sealed by a large insulator that supports the collector. A tertiary flow exists in this region, outside of the high speed primary and secondary streams, at a pressure P_t that is smaller than P_s. It is this pressure difference that accelerates the secondary flow. Thus, three flows exist: (1) the supersonic primary flow into which all the charge is injected, (2) the secondary flow of cool moist air surrounding the primary flow and traveling at about two-thirds the speed of sound, and (3) the tertiary flow, (an eddying flow driven by the friction of the secondary flow). One of the useful functions of the secondary flow of recirculating air is the elimination of solid insulation walls surrounding the primary flow that cause uncontrollable breakdown problems.

Parametric labels in the charts and on the graphs throughout this report are usually the three pressures (in psig or psia), and the corresponding three Mach numbers based on these pressures, for the isentropic expansion of air. The Mach number that is given most often is "M_p". It is a fictitious Mach number that would result if gas were expanded isentropically from P_p to P_s. This number is often about 1.05 (for a pressure ratio of about 2:1). The actual M_p is that of the primary flow around the corona needle. This is about 1.25 due to further expansion after leaving the sonic primary nozzle. M_s is derived from the ratio of P_s and P_t and is usually 0.65. This results from the dimensions chosen and the inherent mixing losses. Lower values are sometimes observed due to excessive losses resulting from damaged, dirty or misaligned nozzles.

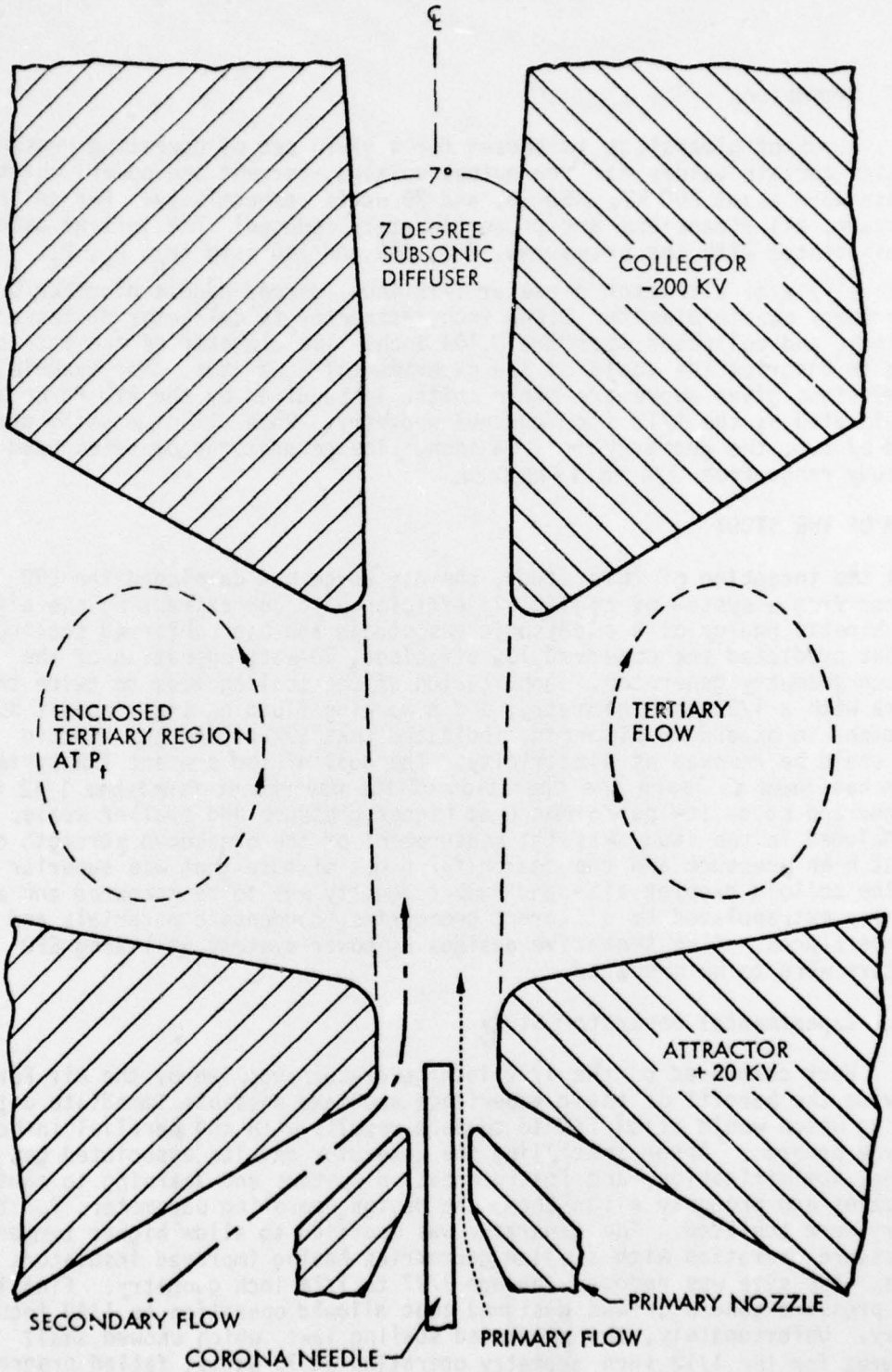

Figure 1. Scale Drawing of the ARL - Symmetrical EFD Generator

b. Dimensions

A set of dimensions is chosen for a given set of operating pressures. This gives certain values for the output voltage, current and power, which in this case were about 200 kV, 350 μa, and 70 watts respectively. For an increase in pressure, all dimensions are proportionately reduced. The initial dimensions associated with the pressures, 700, 350 and 240 psig (P_p, P_s, P_t, respectively) are: attractor diameter 1/12 inch, corona needle diameter 0.020 inch, primary nozzle diameter 0.046 inch, attractor to collector distance 0.275 inch, and collector aperture 0.104 inch. The diameter of the attractor is used to describe the scale of the experimental apparatus. For example, the dimensions given above are those initially supplied by the Air Force and are designated as the 1/12 inch channel geometry. When all dimensions are reduced by two, the geometry is 1/24 inch. The generator geometries used in this study range from 1/4 to 1/48 inch.

3. AIM OF THE STUDY

At the inception of this study, the Air Force had developed the EFD generator from a system of negligible efficiency to one extracting one eighth of the kinetic energy of a supersonic gas stream and had confirmed scaling laws that predicted the observed 13% efficient, 70-watt operation of the 1/12 inch geometry generator. Application of the scaling laws to twice the pressure with a 1/24 inch geometry, and a working fluid having a modest 50% improvement in breakdown strength, indicated that 50% of the gas kinetic energy could be removed as electricity. The goal of the present TRW Systems program has been to learn the operation of the government-furnished 1/12 inch generator and study its performance at higher pressure and smaller scale. Also included in the study was the measurement of the breakdown strength of gases at high pressure and the search for a gas mixture that was superior to air. The colloid droplet size and number density was to be measured and analytically extrapolated to different geometries, condensate materials and gas temperatures. Also tentative designs of power systems utilizing EFD generators were to be prepared.

a. Experimental Generator Study

Work commenced on the 1/12 inch generator supplied by the Air Force to provide the benefit of their experience and make possible immediate data gathering which would allow TRW to compare results with the parallel in-house Air Force program. After installing the generator and its associated gas handling, humidification, and instrumentation systems and learning to contour the nozzles and properly align them, the design operating parameters for this geometry were achieved. The generator was modified to allow higher temperature and pressure operation with smaller geometries having improved insulators and methods. The size was reduced through 1/17 to 1/24 inch geometry. Finally a high pressure generator was designed that allowed operation to 1/48 inch geometry. Unfortunately, the predicted scaling laws, which showed small departures for the 1/12 inch geometry operating at 70 watts, failed progressively for the smaller geometries. Also corona erosion became more severe.

b. Experimental And Analytical Study of Charged Droplets

Experimental studies on a 1/4 inch geometry with Rayleigh-scattered laser light made possible the measurements of droplet size and density. These measurements confirmed the theoretical model which was used to analytically predict sizes and number densities that would be achieved at other temperatures and pressures and with other condensates, such as mercury and steam. This study clearly indicated that the water droplets are spontaneously nucleated and grown from the highly supersaturated, supersonic gas flow before reaching the corona tip where negative charges drift onto them and become attached.

c. Gas Breakdown Experiments

During the program 11 gas mixtures were tested for high voltage breakdown over a range of high pressures, usually to 1000 psig and occasionally to 1500 psig (100 atmospheres). A range of electrode materials and shapes and gas flow conditions were studied. Stainless steel electrodes were then selected for the remainder of the work and most of the subsequent testing was done at a constant P d product.

The study showed that all of the gases investigated showed a linear increase in breakdown strength with increasing pressure up to an electric field of about 10^8 V/M where electrode field emission appears to degrade the insulating strength. Electron attaching gases, such as the oxygen in air, suffer less from this effect than other gases. Consequently, at very high pressures, air is one of the best insulating gases.

d. EFD Generating Systems Analysis

A mixing theory using the equations of compressible gas flow confirmed the predictions of M. Lawson of the Air Force that for single gas systems using high Mach numbers, enthalpy removal of about 8% can be obtained, and that a two-fluid system of mercury and hydrogen does form an attractive closed system using mercury in a Rankine cycle.

Design of a 1 minute, 6 Mw airborne system using stored liquid hydrogen is based on this analysis. Also propane-burning, ground-based power packages of 1 and 100 KW using mercury and hydrogen were designed to operate unattended for 1 year.

4. STRUCTURE OF REPORT

The six sections of this final report are the introduction, followed by each of the four tasks of the study and ending with the conclusions that can be drawn from this study. Briefly summarized these conclusions are: (1) Humidified air EFD generators extract less than 10% of the enthalpy of a low temperature gas, thus limiting its consideration as a practical energy conversion system, (2) mercury-hydrogen EFD generators show promise of a reasonable enthalpy conversion of a gas at a much higher temperature but involve many unsolved problems (in particular, the technique of charge carrier generation).

SECTION II

EXPERIMENTAL GENERATOR STUDY

1. EXPERIMENTAL APPARATUS

The EFD generator components shown in Figure 1 are housed in the pressure vessel shown in Figure 2a suspended on its mounting frame. Access to the generator components is through both the top and the bottom and involves removal of many high strength bolts. The high voltage output comes out of the pressure vessel through a 0.9-inch OD polyethylene cable which connects to a variable resistance load-bank (not shown) within a large corona-inhibiting sphere.

Tests are run remotely from the console shown in Figure 2b. The attractor voltage control is on the left. Pressure regulator controls vary the primary and secondary pressures which are read on precisely calibrated dial gauges. The tertiary pressure is also monitored on a dial gauge. Temperature and humidity are controlled and monitored on the right. The generator output current is monitored by a panel-mounted microammeter that reads the load current returned to ground.

Air is piped into the laboratory from an outside tank array, replenished at intervals by a vendor. The air pressure is dropped to the desired value by a regulator and heated and humidified by the system shown in Figure 3. Heat is created in the walls of 1/4 inch diameter stainless steel tubing by direct passage of current from a transformer. About 1 gram of filtered, deionized water per minute is injected as a fine stream down the center of the air flow. The air is excessively heated and then cooled to assure rapid and complete water evaporation that prevents accumulation on surfaces. Means are provided to vary the amount of water and measure the resulting humidity. The humidity was kept at a standard value of 80% when it was not being varied to study its influence. For the 1/12 inch geometry, this injection rate and humidity required operation at about 125°F.

For the smaller geometries used later, the same water injection rate into the lower volume flow rate required higher temperatures, up to 240°F. For these temperatures, insulation was required around the piping and generator. The generator was heated by wrap-around tape heaters to the temperature of the inlet air before operation, to prevent water condensation.

The output power was dissipated in a resistive load that could be altered in discreet steps from 0 to 800 megohms in 100 megohm steps. The output characteristics of the generator were taken with these different loads. A typical procedure for obtaining data is given. Following the change of some parameter, such as primary nozzle to attractor spacing, the generator was reassembled, aligned, and allowed to reach the required equilibrium temperature. The primary pressure was brought up, the secondary pressure was established and the air temperature and humidity were stabilized. With zero resistance load connected, the attractor voltage was applied and increased to its maximum value (indicated by the onset of arcing) to determine the maximum short circuit current. Typically this current is over 400 μa with about 50 μa of current being collected on the attractor. The above procedure was repeated

PRECEDING PAGE BLANK-NOT FILMED

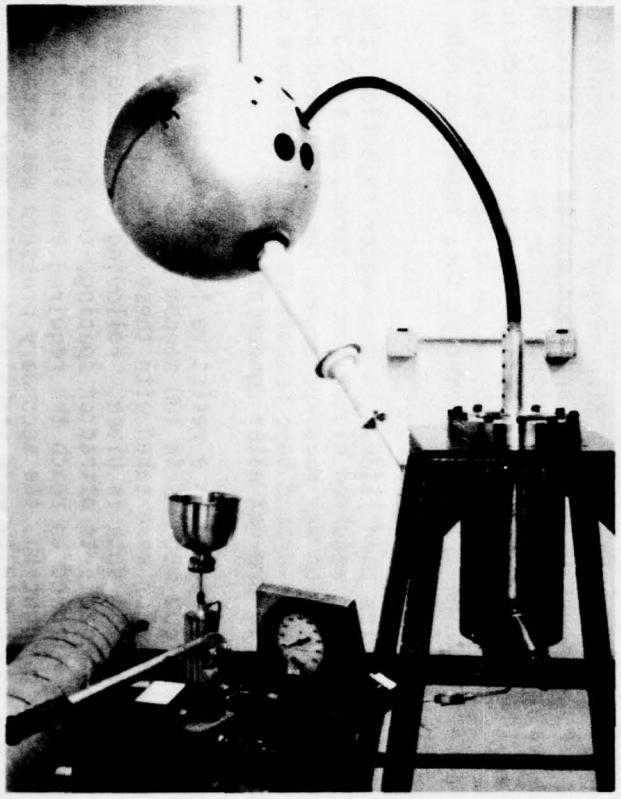

Figure 2a. High Voltage Termination Sphere Mounting (Equipment in foreground is the hydrostatic test rig).

Figure 2b. Photograph of EFD Test Console

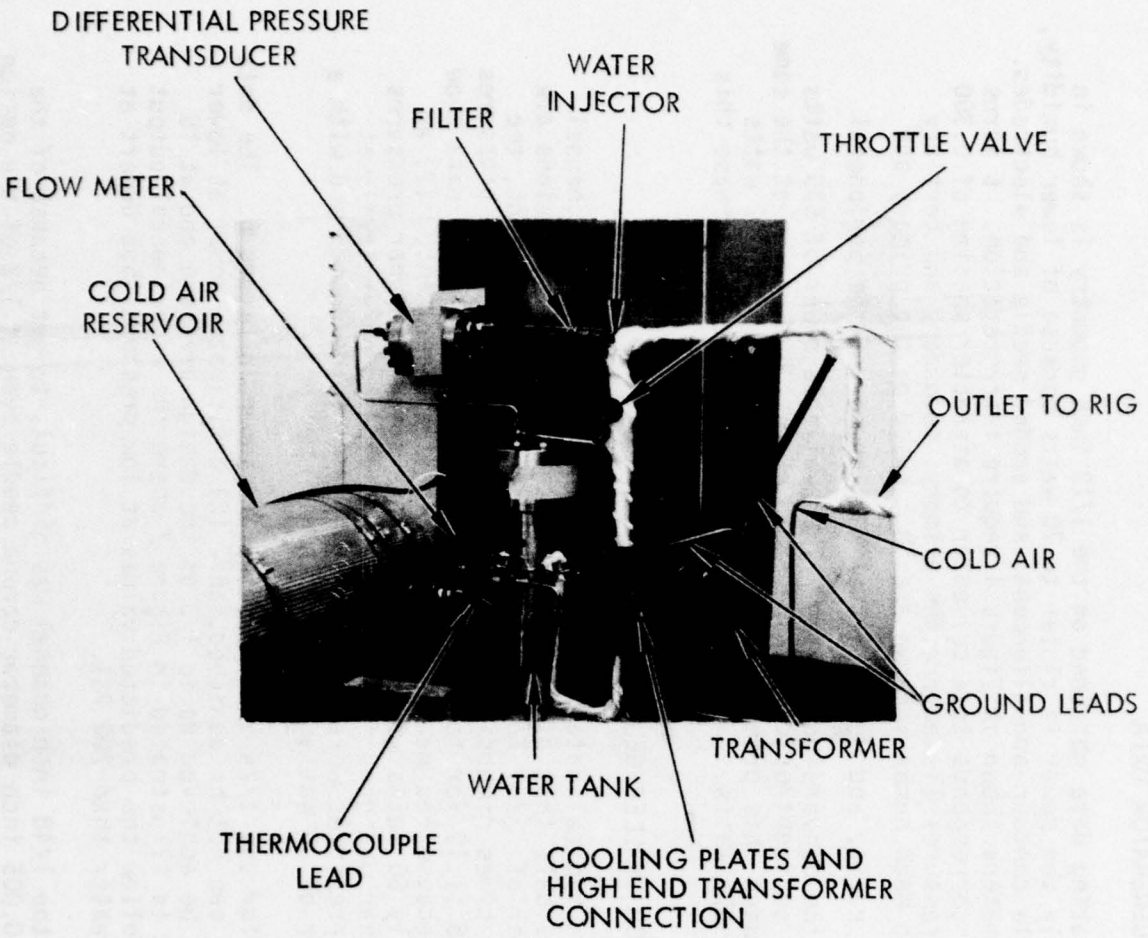

Figure 3. Photograph of Humidifier Systems

with increasing numbers of load resistors (by removing shorting wires across them). As the output voltage increased the maximum current decreased. This was due initially to reduction of the permissible space charge before breakdown resulting from the increased field and subsequently to collector to attractor breakdown.

2. 1/12-INCH EFD GENERATOR DATA

The best operating data obtained on the 1/12 inch geometry is shown in Figure 4. Typically the power is closer to 70 watts because of lower humidity, less accurate nozzle contour and alignment, and eroded needle and electrodes. The operating parameters shown in Figure 4 require interpretation. 6 turns (at 20 turns/inch) corresponds to a collector to attractor spacing of 0.300 inch. The three pressures listed are the primary, secondary and tertiary pressures. The two Mach numbers shown are "M_p" based on the primary and secondary pressure ratio, and M_s the actual Mach number of the peripheral secondary flow in the conversion section. The available power of 575 watts is the shaft power an isentropic turbine could extract by working at the same mass flow rate between this primary and secondary pressure. The 82 watts output is 14.2% of 575 watts. The goal of this program was to increase this efficiency to 50%.

3. TYPICAL DATA FOR SMALLER GEOMETRIES

Figure 5 shows typical data for the 1/17 inch channel. This channel has an area that is half that of the 1/12 inch channel - all dimensions are reduced by a factor of $\sqrt{2}$. To keep the breakdown voltage constant, the product of density times dimension is held constant by raising all pressures by a factor of 1.55 (1.10 for temperature and 1.414 for size). The data show (1) more scatter because the needle eroded during the experiment, (2) an output power of only 60 watts was achieved by operating at higher pressures and Mach numbers than designed for, and (3) anticipated power levels at lower than design pressures were achieved up to 3/4 of the design and with a corresponding power of 30 watts.

Typical data for the 1/24 inch geometry are shown in Figure 6. The data show (1) 60 watts can not be achieved, and (2) anticipated power at lower pressures can only be achieved up to 1/2 of the design pressure and at 15 watts. This trend is illustrated in Figure 7 where the experimental output power is seen to follow the predicted values at low pressures but depart at input pressures greater than 700 PSI.

The data for the 1/48 inch channel was difficult to get because of the rapid wear of the 0.005 inch diameter corona needle even at 1/2 of the design pressure. The data are shown as scatter bands. For example, Figure 8 shows the typical scatter band for the 1/48 inch geometry working at a little less than 1/2 of its design pressure. The measured power was much less than the anticipated power.

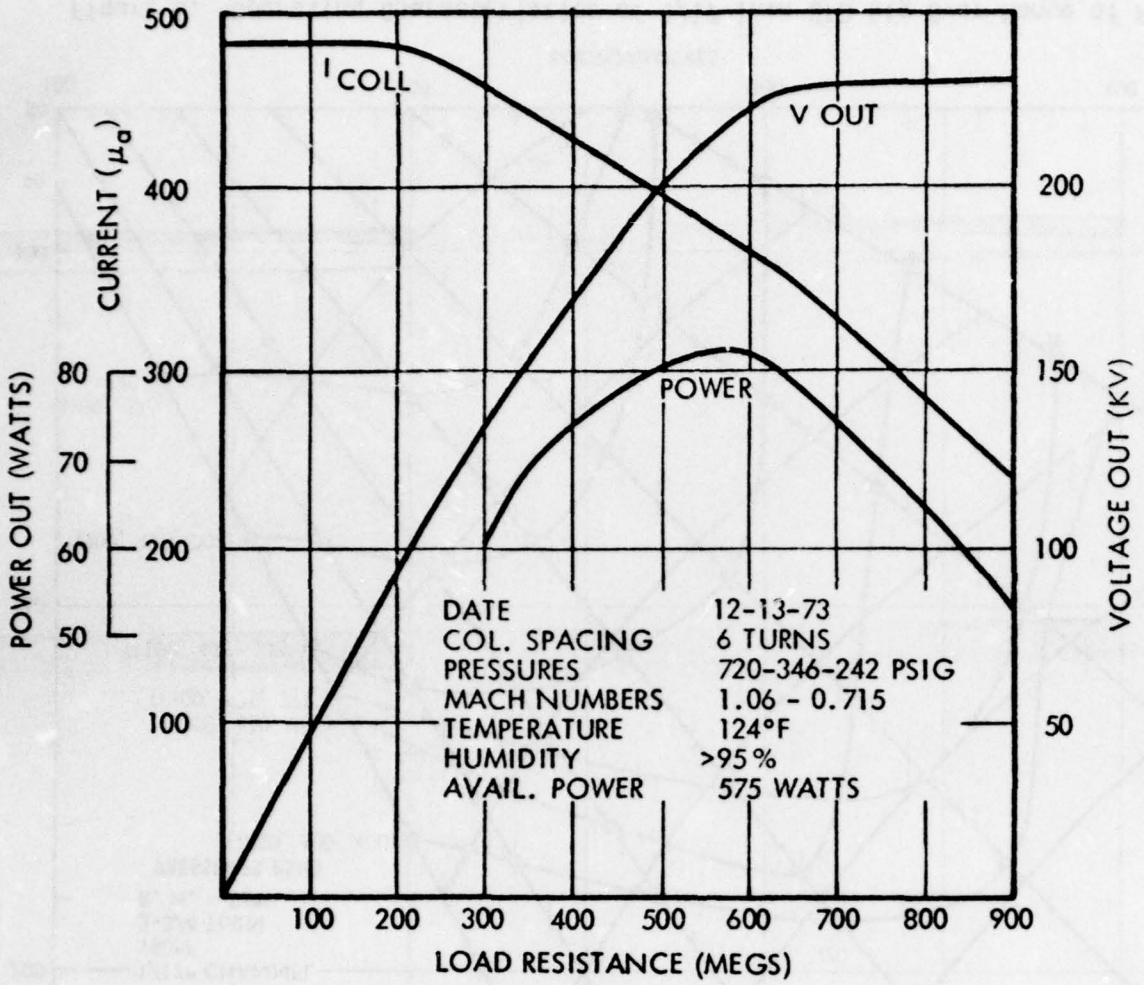

Figure 4. Operating Characteristics at 95 Percent RH. 82 Watts Output Power

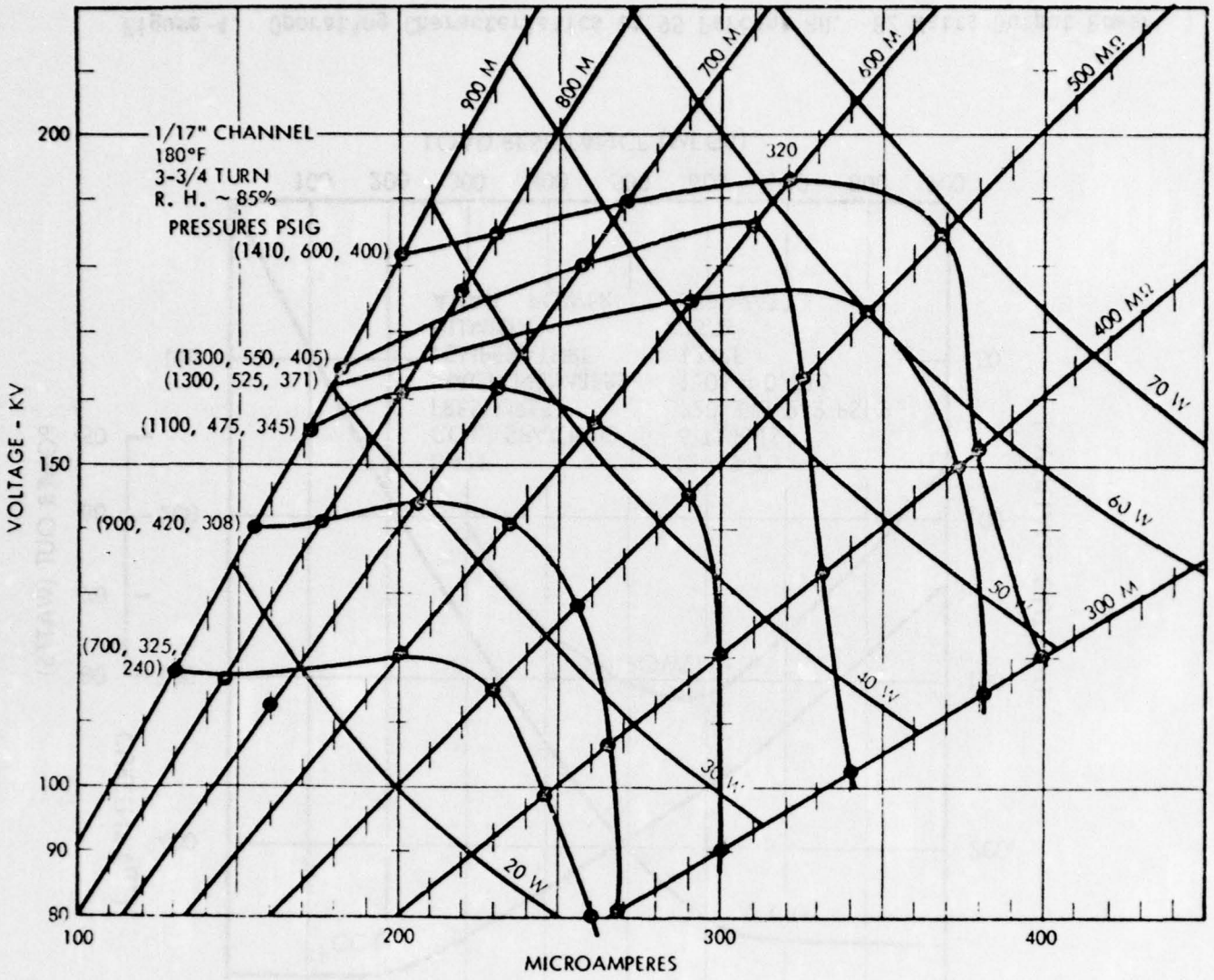

Figure 5. Operating Characteristics of 1/17 Inch EFD Rig Over Range of Pressures

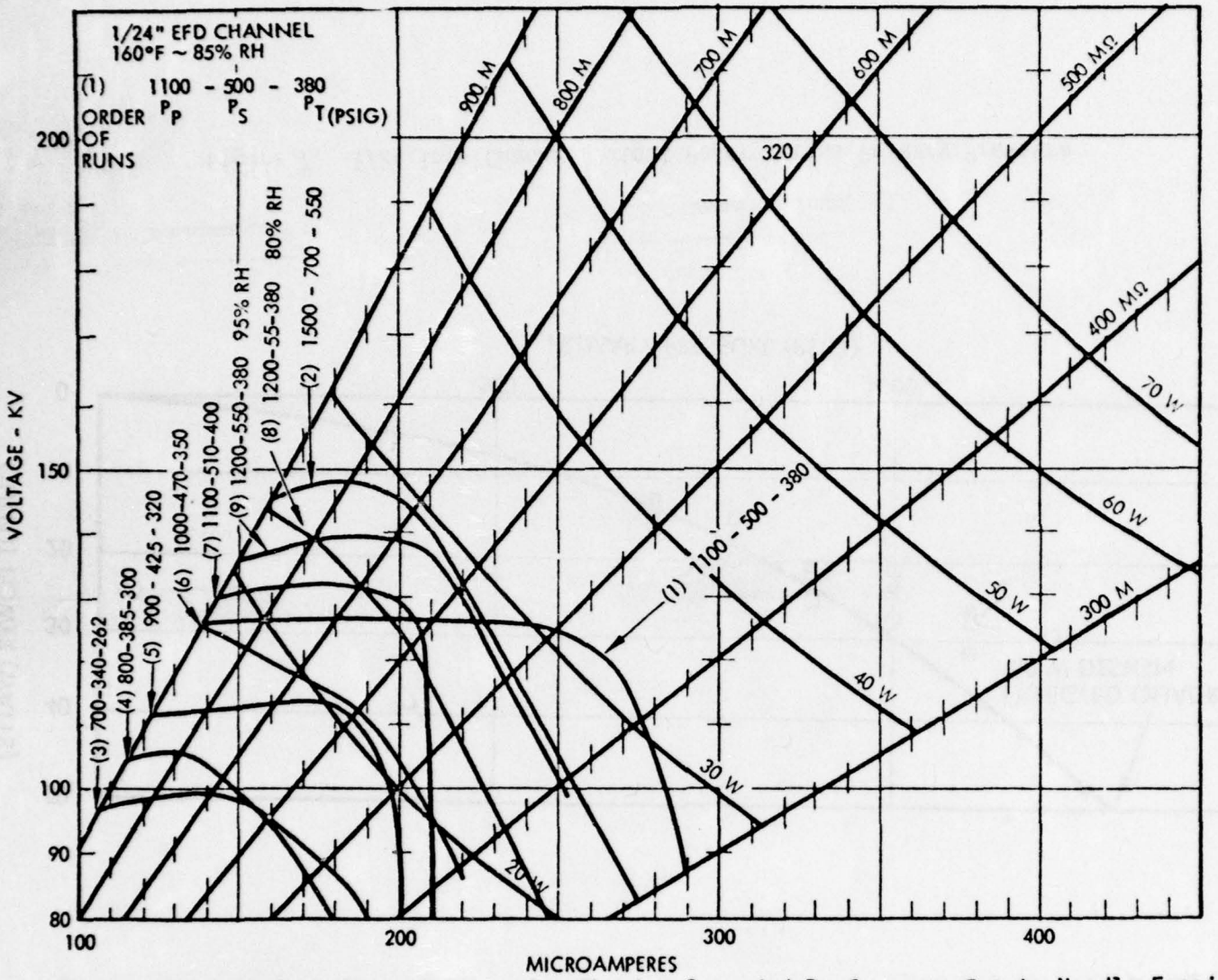

Figure 6. 1/24 Inch Channel Operation Showing Degraded Performance Due to Needle Erosion

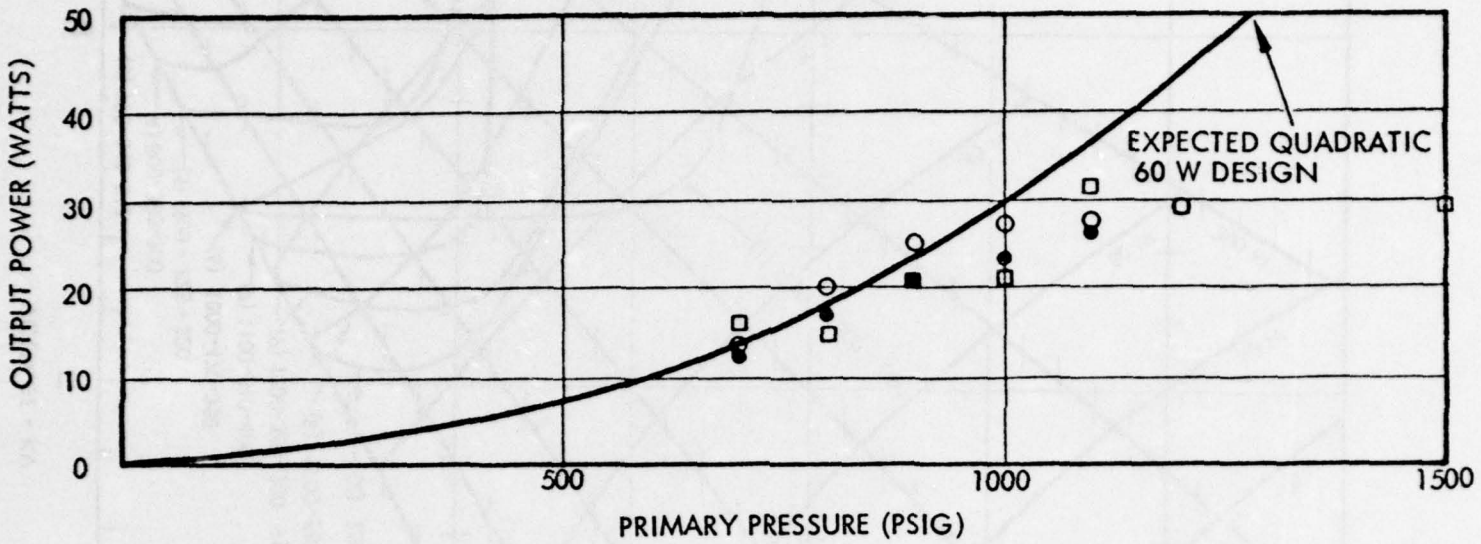

Figure 7. 1/24 Inch Channel Output Power Versus Primary Pressure

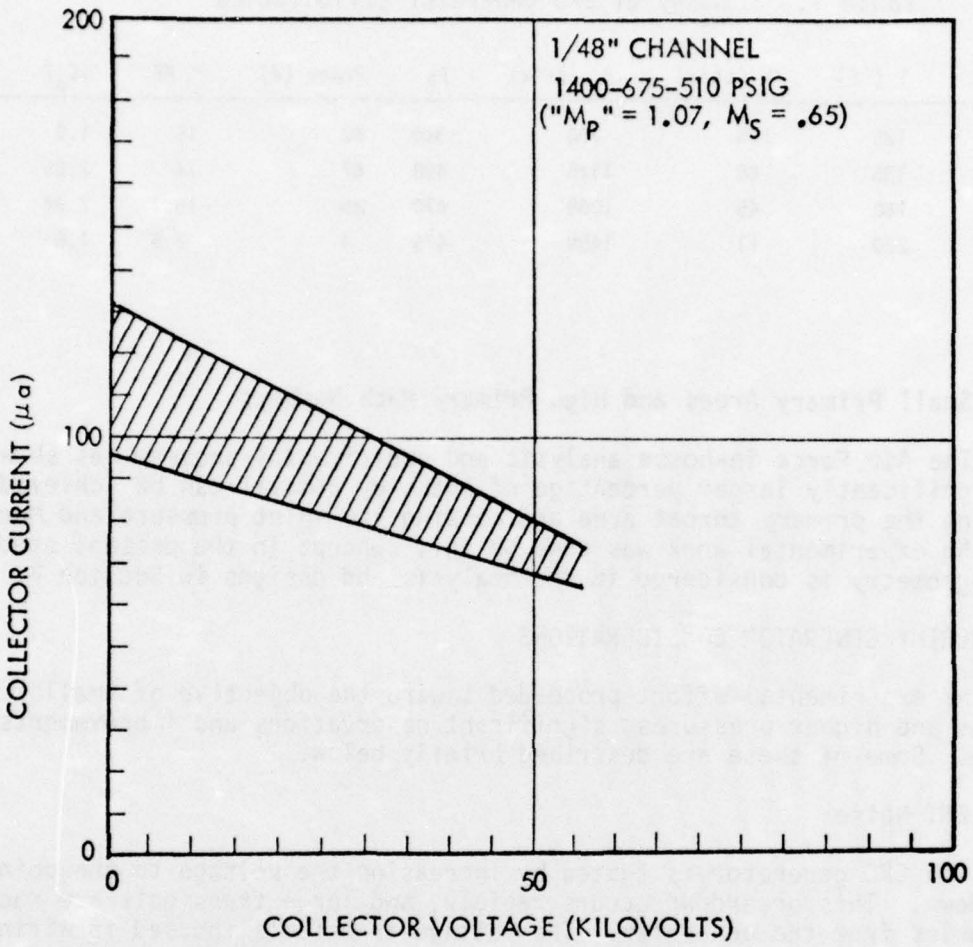

Figure 8. Collector Current versus Voltage for the 1/48 Inch Channel at 1/2 Design Pressure

a. Maximum Kinetic Efficiency, Maximum Power, and Maximum Enthalpy Removal

For a given generator geometry and a given primary plenum pressure, maximum power output (corresponding to maximum enthalpy removal) occurs at an output pressure that provides adequate mach numbers for droplet formation and at the same time adequate gas density to allow high output voltage. As the primary plenum pressure is raised, a point is reached where this maximum obtainable output power increases only linearly (instead of quadratically) with pressure. This marks the point of maximum percentage enthalpy removal. This point of operation is desired for operation in a single stage, blowdown, system. In a closed system or a staged system where the remaining enthalpy is important, an operation point at slightly higher output pressure is desirable which produces lower mach numbers and higher kinetic efficiencies. In this program parameters were chosen to maximize the kinetic efficiency. Table I shows the maximum kinetic efficiency anc associated parameters and entholpy removal for geometrics tested.

Table 1. Summary of EFD Generator Efficiencies

Size (in)	T (°F)	V (cc/s)	P_0 (psia)	Ps	Power (W)	% KE	$\%C_pT$
1/12	125	175	700	340	82	15	1.9
1/17	135	88	1115	490	67	14	2.85
1/24	180	45	1000	470	25	16.7	2.34
1/48	220	11	1400	675	4	5.5	1.0

b. Small Primary Areas and High Primary Mach Numbers

The Air Force in-house analytic and experimental program has shown that a significantly larger percentage of enthalpy removal can be achieved by reducing the primary throat area and raising the inlet pressure and Mach number. No experimental work was done on this concept in the present study, but this geometry is considered in the analysis and designs in Section V.

4. NOTEWORTHY GENERATOR CONSIDERATIONS

As the experimental effort proceeded toward the objective of smaller geometries and higher pressures, significant observations and improvements were made. Some of these are described briefly below.

a. EMI Noise

The EFD generator is tested by increasing the voltage to the point of breakdown. This breakdown occurs rapidly, and large transients are radiated by the cables from the generator. The voltage transients induced in wiring throughout the building are large enough to cause arcs in the power lines, trigger sensitive scopes and instruments, and burn out most of the instruments (controllers, etc.) that utilize sensitive solid state devices. Repeated failure of local equipment was prevented by properly placed input capacitors. However, the only satisfactory solution to the overall problem was to place current limiting resistors in the leads before they were brought out of the pressure chamber. This was done on the generator as well as on the gas breakdown experiment and worked well.

b. Humidity Measurement

Careless humidity control can produce droplets in flows having less than 100% relative humidity. This causes poor, erratic generator operation because the large droplets grow at the expense of the uniformly distributed small ones in the supersonic expansion. Various techniques have evolved that allow molecular (droplet-free) flow up to 100% relative humidity by initially overheating the air and then cooling it. Exact temperature control and monitoring are required. The quantitative value of relative humidities less than 100% is determined by measuring the ratio of water flow rate to that corresponding to the onset of erratic operation.

Two useful tools that were developed to accurately measure humidity are sketched in Figures 9 and 10. These involve quantitative water flow measurements with a stop watch and exact observation of the onset of 100% humidity by observing condensation. The technique works at primary pressures in excess of 1000 psi.

c. Nozzle Mounting and Contour

The most critical item in the EFD Generator is the primary nozzle. It must be contoured properly, clean, polished, and free of nicks. The best performing nozzle has a constant sonic exit area about 1 diameter long, blending smoothly into a 60 degree taper. The nozzles are machined on a jeweler's lathe and for ease of replacement, are mounted as shown in Figure 11. The corona needle shown here is for the 1/24 inch geometry. The 1/12 inch geometry uses the full 0.020 inch diameter of the Pt-Ir wire.

The attractor nozzles and diffuser were also machined on the jewelers lathe and inserted into the larger electrodes. Thus scale size was readily changed by simply inserting different components.

d. Alignment

The generator efficiency falls quite rapidly if the axes of all three nozzles are not collinear. This becomes more difficult to control for the smaller geometries. Precision machining was never relied upon to achieve the alignment. Instead, the parts were moved around until proper alignment was indicated by the lowest tertiary pressure (tested with atmosphere secondary pressure). Stability of alignment was important as the parts were handled, heated, and pressurized.

e. Insulator

The best insulator in the EFD generator is the high pressure air; at 20 atmospheres it is over 1500 volts/mil, exceeding all bulk solids. The solid materials in the generator, more commonly called insulators, can stand off the voltage only by being much longer than the electrode spacing. Consequently, the electrodes are reentrant shapes extending inside the insulator. Plastics have higher breakdown strength, especially at high humidity, than glasses. Plastic insulators worked well at the lower temperatures. The use of ceramics, to allow higher pressures and temperatures, caused severe insulator breakdown and leakage problems. These were solved by having an outside vendor make the insulators sketched in Figure 12. These worked well up to 250°F but were inadequate at 500°F in steam because of excess alkali impurity in the alumina and glass glaze.

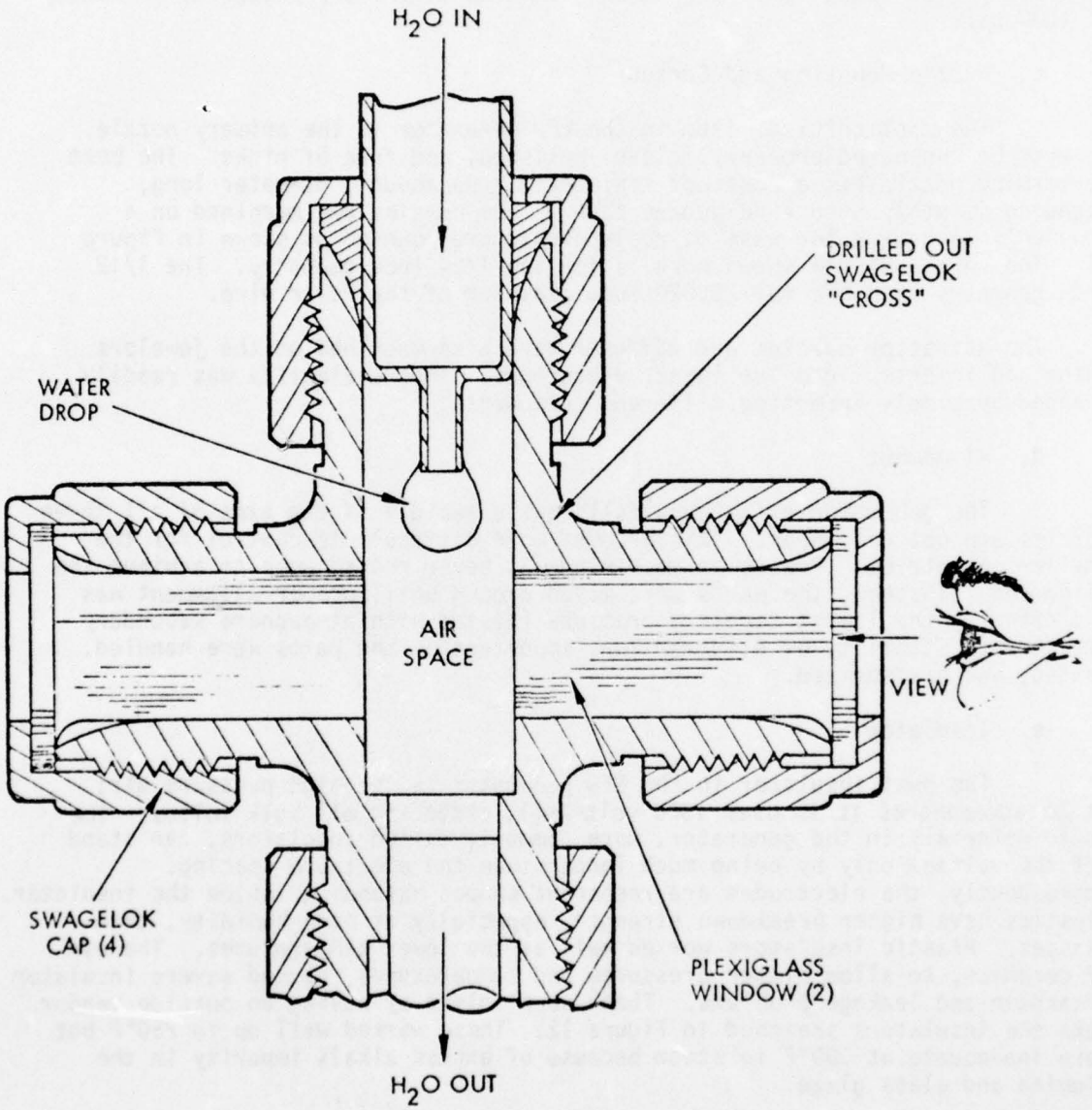

Figure 9. High Pressure Water Flow-Meter. Drops are timed with a stopwatch

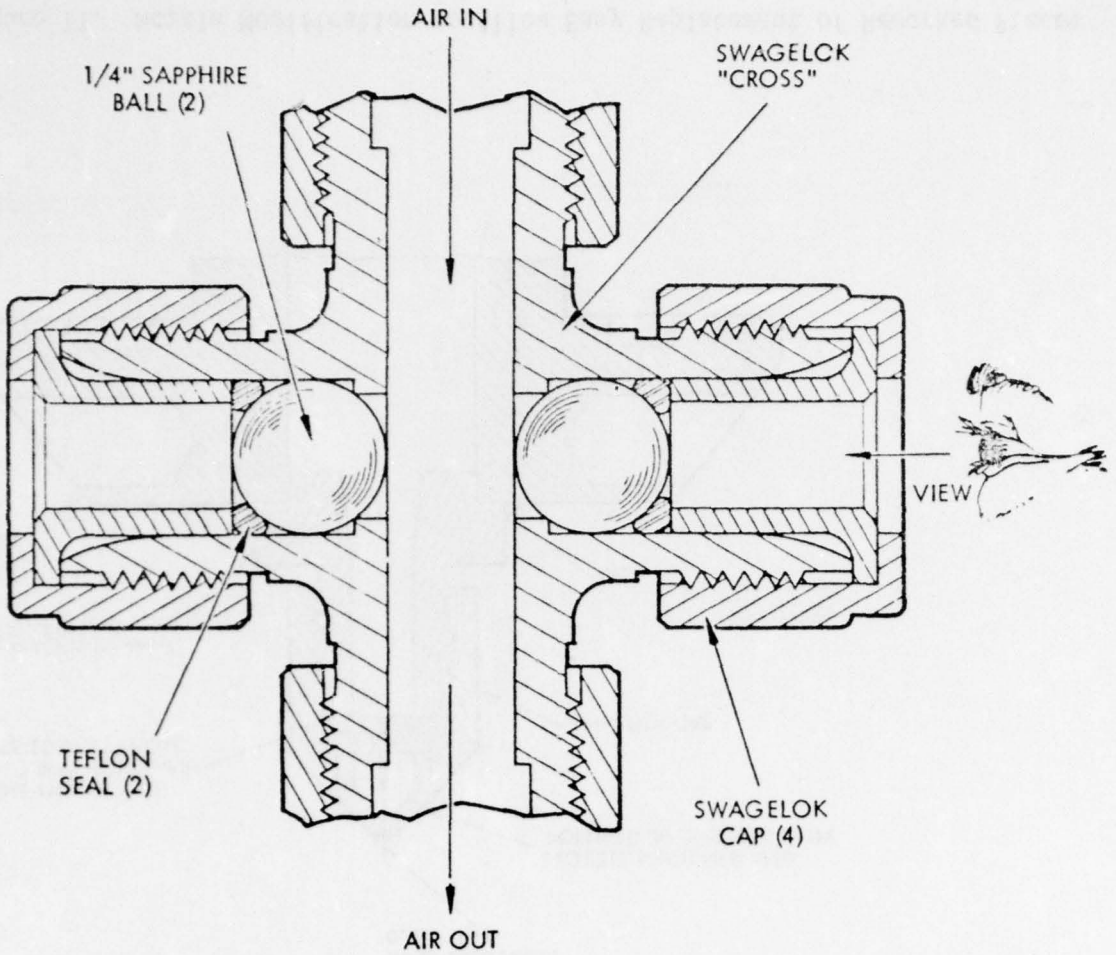

Figure 10. High Temperature, High Pressure, Dew-Point Sight-Glass
Above 100% humidity, drops can be seen condensing on the
sapphire surface.

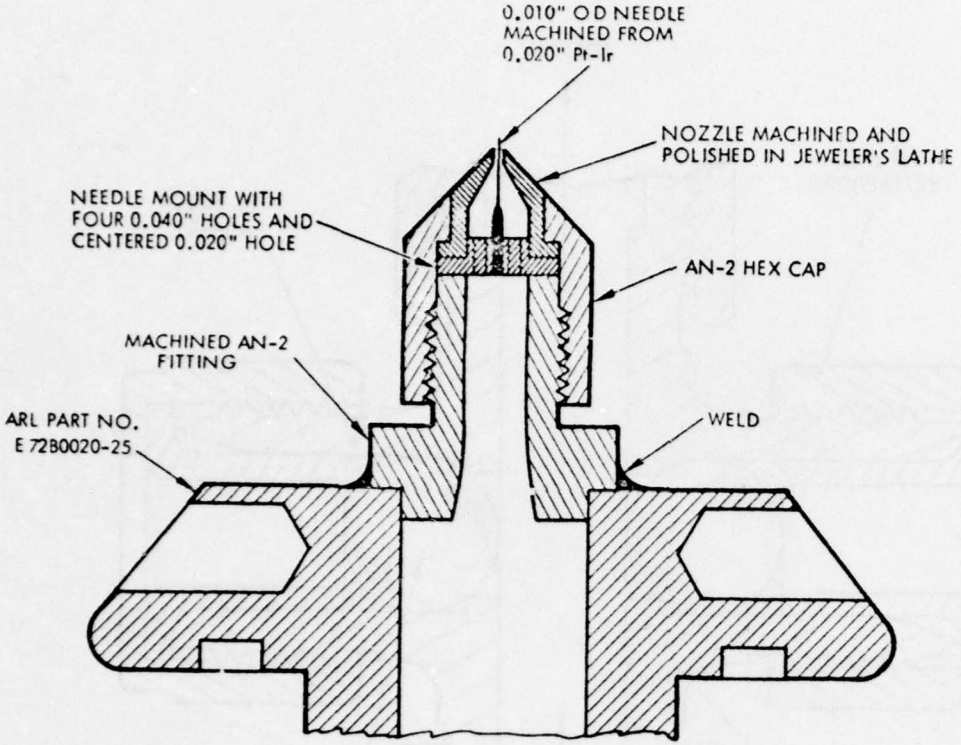

Figure 11. Nozzle Modification to Allow Easy Replacement of Reworked Pieces

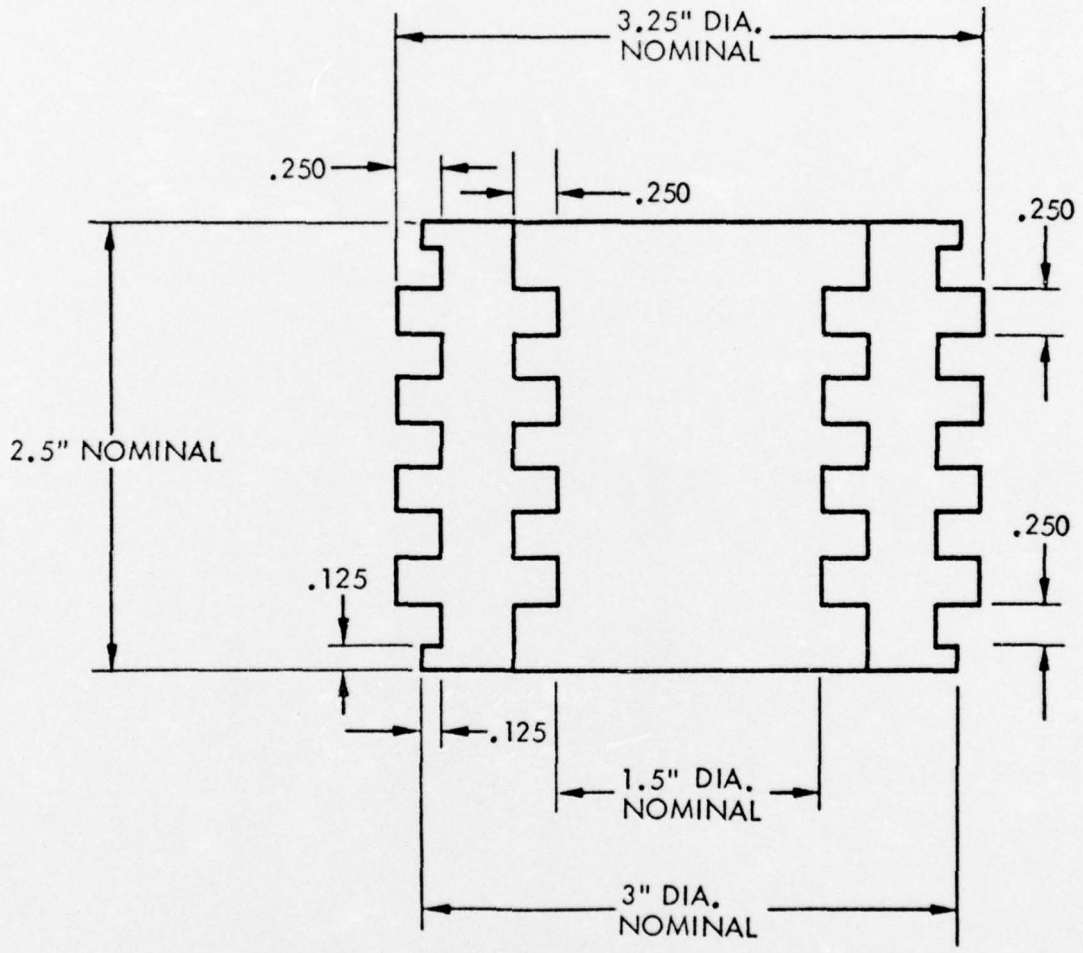

99.5% ALUMINA INSULATOR
HI Ca AND Pb GLAZE UNDER COMPRESSION

Figure 12. Insulator Designed to Eliminate Surface Breakdown at High Temperature and Humidity

SECTION III

EXPERIMENTAL AND ANALYTICAL STUDY OF CHARGED DROPLETS

This section presents the description of the experimental apparatus and the Rayleigh scattering laws that allowed measurements to be made of laser light scattered off the water droplets in the supersonic flow. These were compared to scattering from a calibrating gas to yield data on droplet size and spacial and number distribution. Analyses, confirmed roughly by the experimental data, are presented that predict the droplet sizes and number densities that would result under different conditions, such as expansion ratios, specific heat capacity ratios, temperatures, pressures and different mixtures of materials.

1. DESCRIPTION OF EXPERIMENTAL APPARATUS

The apparatus in which the experimental studies were performed is illustrated in Figure 13. It is a very versatile 1/4-inch EFD generator geometry that has four optical ports that permit viewing the conversion region. Axial traverses of this region are made by sliding the generator as a unit with respect to the stationary optical ports. During the laser scattering experiment, the top port contained a photomultiplier tube and its region-defining optics, while a horizontal port contained a window through which a small diameter laser beam entered from a 20 mW, horizontally polarized, argon laser. The other ports contained light traps. The laser beam and the multiplier optics defined a small volume that could be scanned vertically through the center of the jet by raising and lowering the laser. This scan could be done at different axial stations between the secondary (attractor) nozzle and the diffuser (collector).

During velocity profile measurements, one of the light traps, Figure 14a, was replaced by a small pressure probe, Figure 14b, that could be traversed horizontally across the gas jet within the secondary nozzle as well as at different stations downstream of the secondary nozzle toward the collector.

During hydrodynamic spraying experiments, water was introduced into the central needle. This needle can have its axial position simply and continuously varied during the experiment by an adjusting screw. In addition, accelerating voltages can be applied between the needle and primary nozzle as well as between the needle and secondary nozzle. The collector is insulated to allow measurements of current and has insulation to allow modest (not greater than 50 kV) voltage rise. This feature was used to infer the mobility of the hydrodynamically formed droplets.

Figure 15a and Figure 15b show the apparatus used for the laser beam scattering experiment. Figure 16a shows the gas thermal control system that works in conjunction with the water humidifier system, shown in Figure 16b, to produce an accurately known relative humidity. The gas source, which must be very free of any nuclei for condensation, is the same bottled gas that was used for the higher pressure EFD generator study. When possible, the scattering experiment used the low pressure air that was inadequate for use by the 1/12-inch or smaller generators and would otherwise have been wasted.

PRECEDING PAGE BLANK-NOT FILMED

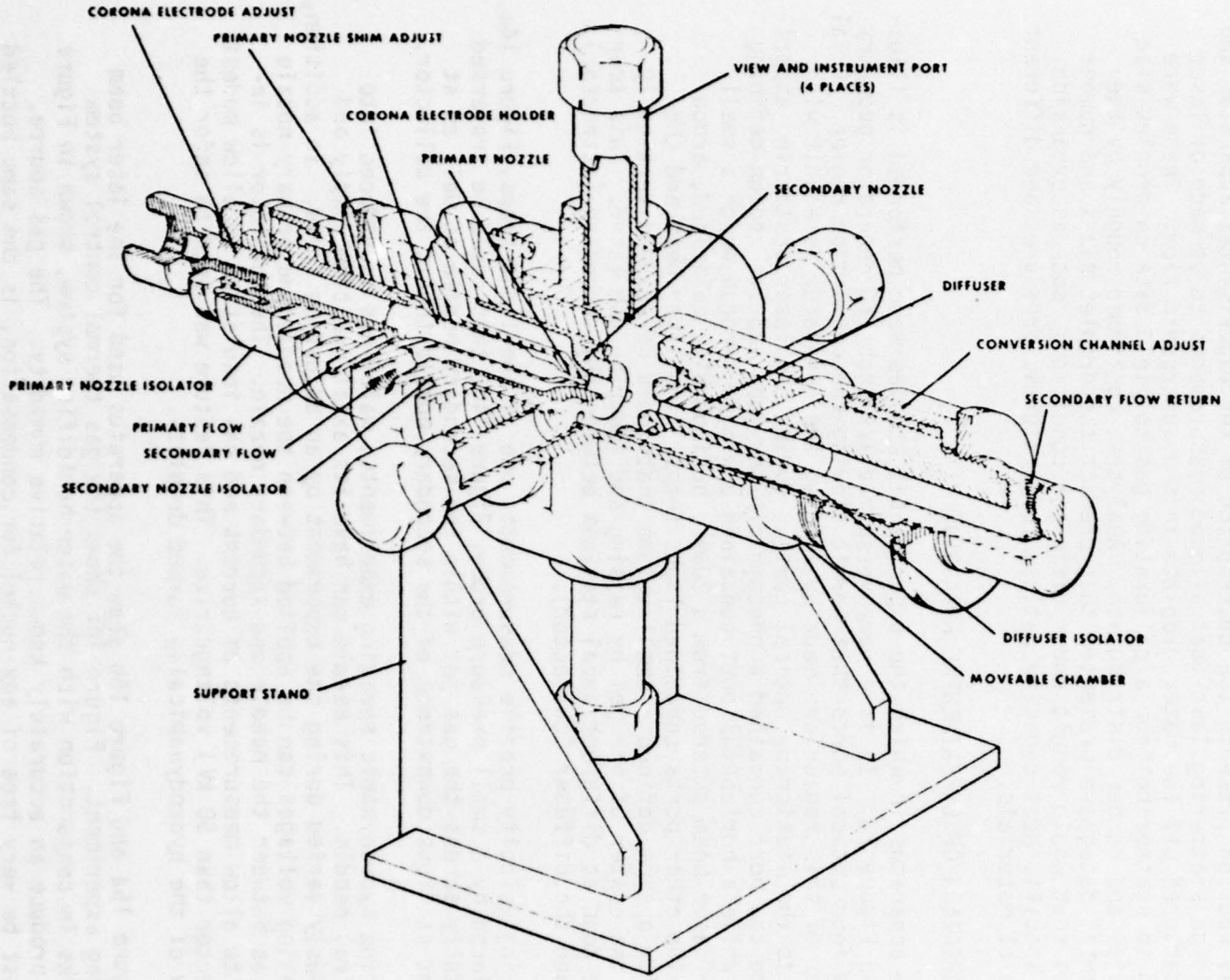

Figure 13. Charged Droplet Experiment

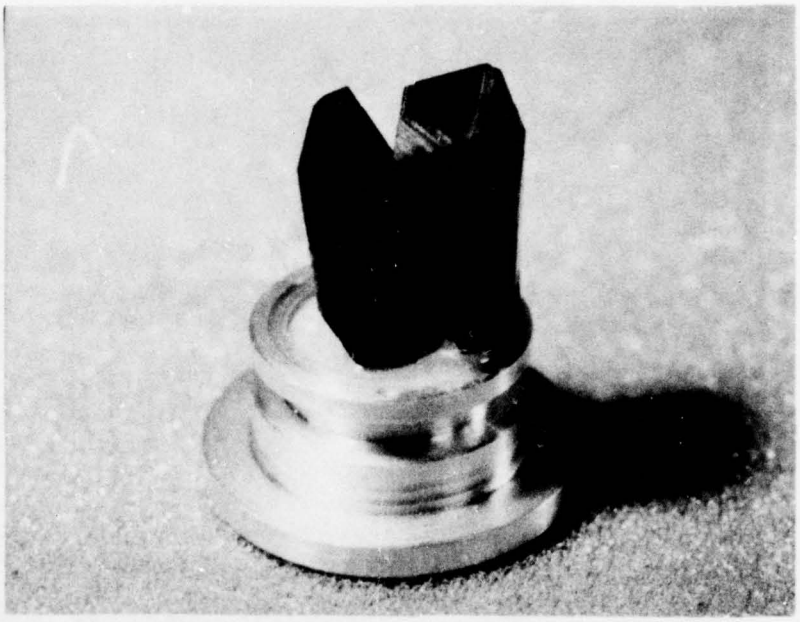

Figure 14a. Light Trap

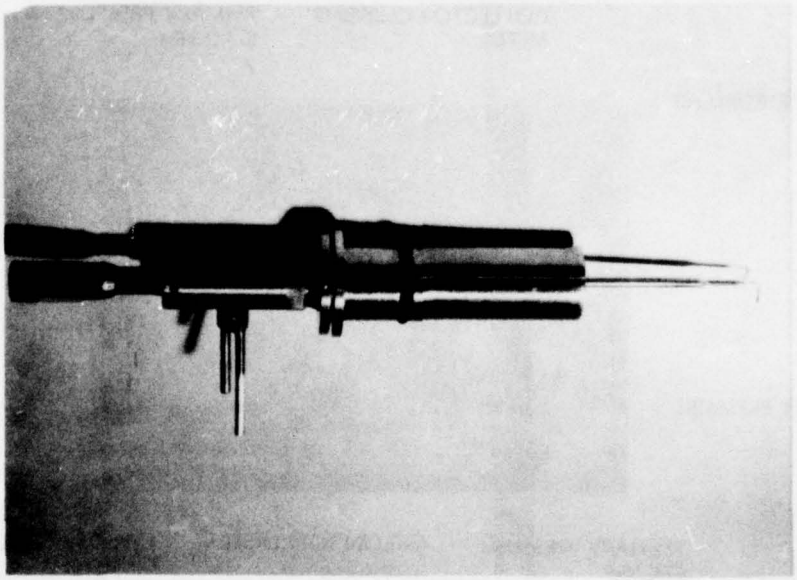

Figure 14b. Pressure Probe and Traversing Head

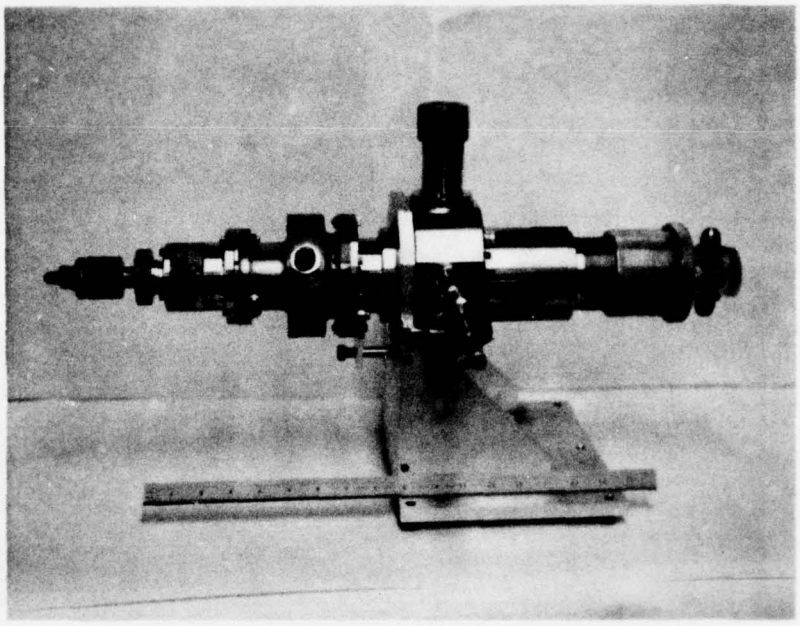

Figure 15a. Photograph of 1/4 Inch Experimental Channel

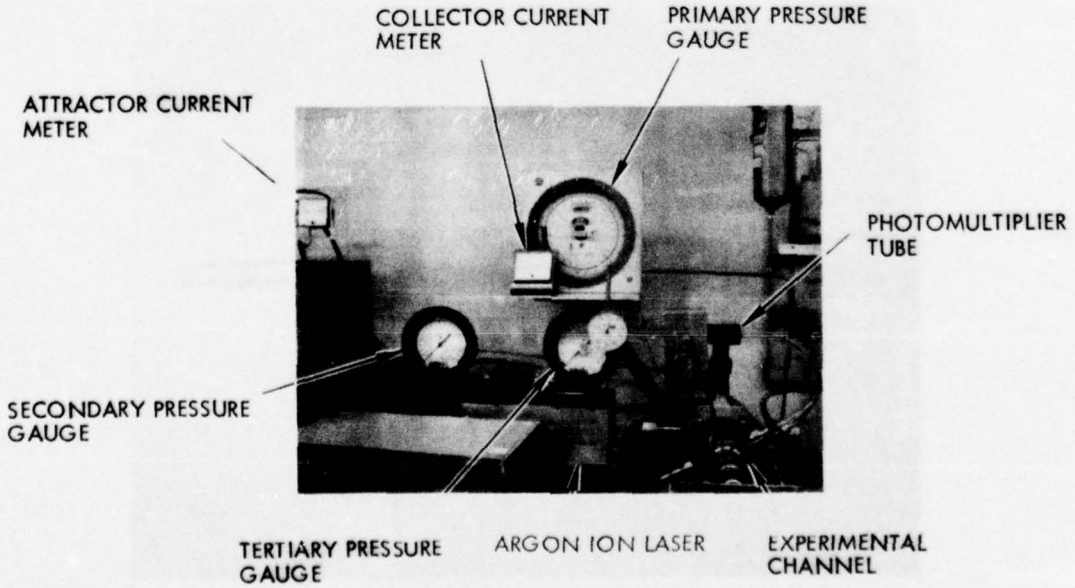

Figure 15b. Laser Beam Scattering Experimental Apparatus

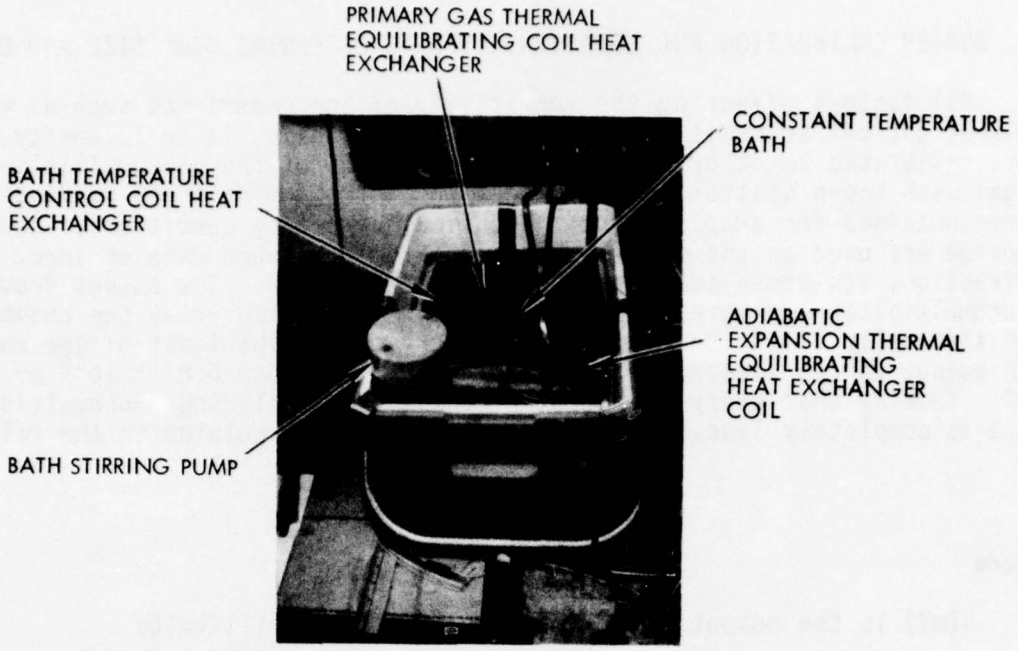

Figure 16a. Primary Gas Thermal and Equilibrating Bath and Heat Exchangers

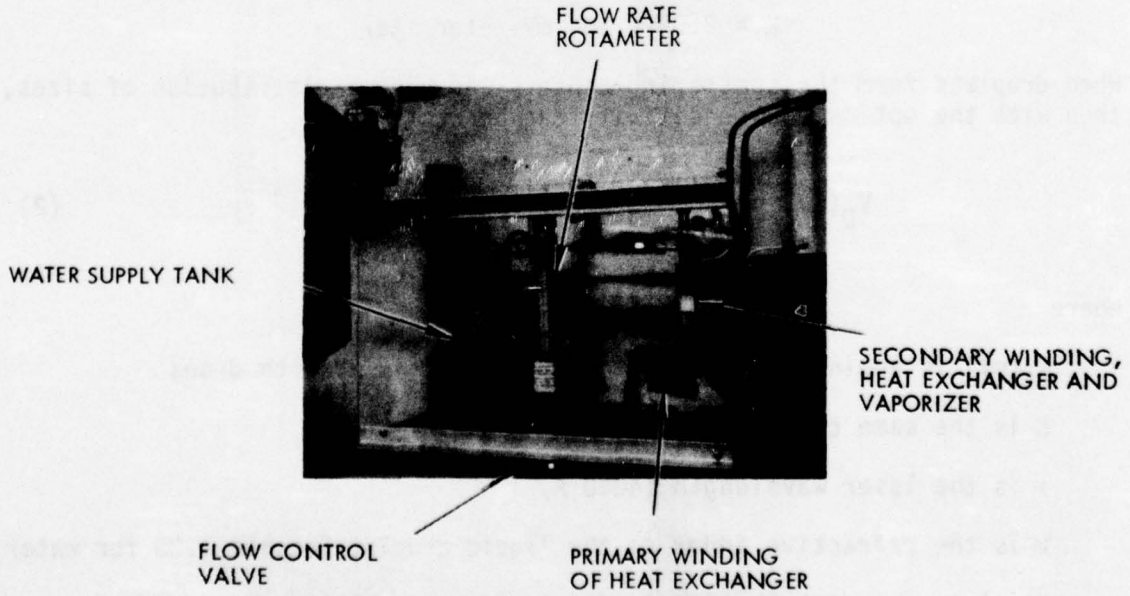

Figure 16b. Experimental Channel Humidifier System

2. SYSTEM CALIBRATION AND EQUATIONS USED TO DETERMINE DROP SIZE AND DENSITY

All factors affecting the sensitivity of the experiment such as view volume, optical transmittivity, photomultiplier gain, laser intensity, etc., were calibrated together by measuring the output of the photomultiplier using a gas with known scattering cross section and comparing these readings with those obtained for droplets under identical operating conditions. Carbon dioxide was used as the calibrating gas. From published data on index of refraction, its cross section is $1.98 \times 10^{-31} M^2/ster$. The output from the photomultiplier was carefully read on a digital voltmeter as the chamber was statically filled to different pressures up to the limit of the chamber. The output varied linearly as it should with a rate of 6.87×10^{-2} mV per psi. Knowing that every component of the system including photomultiplier tube is completely linear, the constant K can be calculated in the relationship

$$V(mV) = K \sigma n \qquad (1)$$

Where

$V(mV)$ is the output of the photomultiplier in millivolts

σ is the cross-section in m^2

n is the number of scattering molecules per m^3.

Equating the observed 6.87×10^{-2} mV for a room temperature number density of 1.69×10^{24} molecules at 1 psi in carbon dioxide with $\sigma = 1.98 \times 10^{-31} m^2/ster$, then

$$K = 2.05 \times 10^{5} \text{ mV-meter ster}$$

When droplets form the scattering centers and have a distribution of sizes, then with the optics and sensitivity can be written[b]

$$V_D(mV) = K \left(\frac{16\pi^4}{\lambda^4}\right)\left(\frac{m^2-1}{m^2+2}\right)^2 \int_0^{r_{max}} N'(r) r^6 dr \qquad (2)$$

Where

$V_D(mV)$ is again the photomultiplier output in mV with drops

K is the same constant as above

λ is the laser wavelength (4880 Å)

m is the refractive index of the liquid droplet (equals 1.33 for water)

N'(r) is the distribution function of the droplet number density

r is the droplet radius in meters

$$C_o = K\left(\frac{16\pi^4}{\lambda^4}\right)\left(\frac{m^2-1}{m^2+2}\right)^2 \quad \text{evaluated is } 2.35 \times 10^{32} \text{ mV/M}^3.$$

A mass balance can be made on the condensate and expressed as:

$$f(\dot{Q}_w/\dot{Q}_o)\ (\rho_T/\rho_o) = \frac{4\pi}{3}\int_0^{r_{max}} N'(r)\ r^3\ dr \qquad (3)$$

Where

f is the fraction of the condensate in the liquid phase

$\dot{Q}_w$ is the condensate liquid phase volumetric flow rate into the primary gas flow stream

$\dot{Q}_o$ is the primary gas volumetric flow rate at stagnation conditions.

ρ_T is the primary gas density at tertiary conditions

ρ_o is the primary gas density at stagnant conditions.

This equation is valid only in regions where there is no mixing of the secondary and primary gas flows.

If the droplet size distribution is known, then the droplet number density and sizes can be determined from a simultaneous solution of Equations (2) and (3). Although it is not consistent with the computer analyses, it was assumed for a first approximation that the droplets are uniform in size. The droplet radius, r, can then be determined from the expression

$$r = \left(\frac{4\pi\dot{Q}_o V_D\ \rho_o}{3C_o f\dot{Q}_w\ \rho_T}\right)^{1/3} \qquad (4)$$

and the number density N', from

$$N' = \left(\frac{C_o}{V_D}\right)\left(\frac{3f\dot{Q}_w \rho_t}{4\pi\dot{Q}_o\rho_o}\right)^{1/2} \qquad (5)$$

These expressions were used to analyze the test results and to obtain a first approximation to the water droplet characteristics in the 1/4-inch channel. The primary volumetric air flow at stagnation conditions, Q_o, for all of the runs was $1.58 \times 10^{-3} m^3/sec$. $\dot{Q}_w$ is directly measured in the rotameter flowmeter and varies with the temperature and humidity; typically it was $1.7 \times 10^{-8} m^3/sec$. $\rho_o/\rho_T = 1.84$ for the pressure ratios used in the experiment.

3. EXPERIMENTAL RESULTS

Scans of the colloid beam were taken at distances of 0.04 and 0.55 inch from the attractor face. The data are presented in Figure 17. There are several features of these scans that are of particular interest. These include:

- Diffusion of the colloid particles into the secondary flow from the primary stream
- Increase in peak and total integrated scattered light intensity in the downstream profile.

The depression in the scattered light intensity in the center of the colloid beam is due to the influence of the corona pin. The depressed signal probably represents both a decrease in droplet number density and size. The flow recirculation at the tip of the corona pin results in a

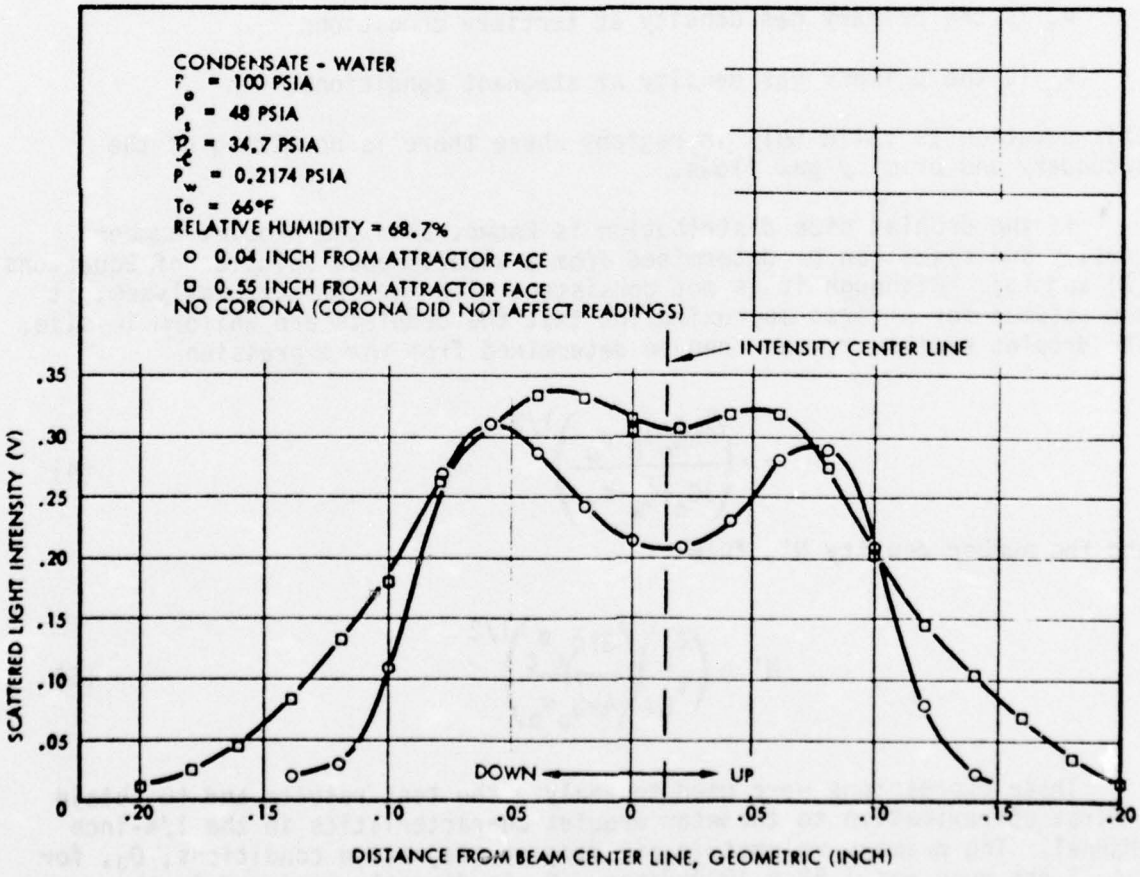

Figure 17. Scattered Light Intensity Scan Profiles Across the Channel Colloid Beam

warming of the gas which causes the entrained droplets to evaporate. This recirculating flow is continually being fed by, and reentrained into the primary flow. The relative magnitude of the decreased centerline signal decreases with distance down the channel. This diminishing effect could be the result of both stream mixing and droplet growth.

The peak value of the scattered signal for the profile nearest the attractor occurs slightly inside of the nominal outer diameter of the primary flow stream. The peaking of the signal could be the result of mixing of the primary and secondary flow streams at the outer periphery of the primary stream. This mixing would reduce the saturation ratio of the water vapor in this region, causing a reduction in the nucleation rate. The resulting fewer droplets would grow larger, and because of the sixth power of the scattering cross section with radius, cause the large scattered signal intensity.

A comparison of the light intensity profiles at the two locations indicates that the droplets are diffusing out from the primary stream into the secondary stream. This is probably the result of mixing of the two flow streams. It appears from the downstream profile, that droplets have even migrated out into the tertiary flow region.

Both the peak light intensity and the total integrated intensity increased with distance from the attractor face. This behavior indicates that the droplets were growing in size with distance along the channel. There was a wide range of droplet sizes because they were formed at a finite rate in the primary gas stream. The larger droplets grow in size at the expense of the smaller droplets when the saturation ratio of the water vapor is below the stability limit of the smaller droplets. Thus, the droplet number density can be decreasing, but those droplets remaining are growing larger resulting in an increased scattering signal.

If it is assumed that the peak values of the profiles represent regions of unmixed primary flow and that the droplets are uniform in size, then the droplet number density and radius at the 0.04-inch position are 6.45×10^{17} droplets/m^3 and 1.13×10^{-8} m, respectively. At the 0.55-inch position, the respective values are 6.97×10^{17} droplets/m^3 and 1.16×10^{-8} m. Although the assumptions used in deriving these numbers are contrary to the previous discussion of the light intensity profiles, they should indicate mean droplet number density and radius values and trends. The conditions for this experimental run are similar (but not identical) to the input data in the computer run shown in Figure 32. The computer data indicated that nucleation should be complete and the droplet size distribution small at the observation plane 0.55-inch downstream from the attractor face. The experimentally determined droplet number density at this plane was approximately 0.35 times that calculated.

The computer analyses of the nucleation rate model indicated that nucleation would be complete prior to the flow reaching the corona, assuming a humidity of ~68.7%. This result was verified by the fact that the scattered light intensity was independent, within experimental error, of whether the system was operated with or without corona. The results of the analyses had also indicated that nucleation was proceeding even at extended distances along the channel at the lower humidities. To observe this effect, a

scattered light scan was taken near the attractor face, with and without corona, for a primary gas humidity of 39.5%. The results are shown in Figure 18. As can be seen in the figure, the scattered light intensity profile has the same general shape for the two cases; however, the intensity was lower with corona. This decreased intensity is due to the larger number of droplets, resulting from the nucleation enhancement by the corona produced ions. The droplets are smaller in size due to the larger number density. Some of the skewness resulted from a temperature increase (from 20° to 21°C) of the primary gas stream during the experimental run.

As can be seen in Figures 17 and 18, the profiles are not symmetrical, even about the translated beam intensity centerline. This is probably because of the method by which the transverse profiles were taken. The optics were fixed and the laser was translated in a vertical direction. The movement of the laser relative to the viewing optics would change the view volume, and therefore the scattered light source size.

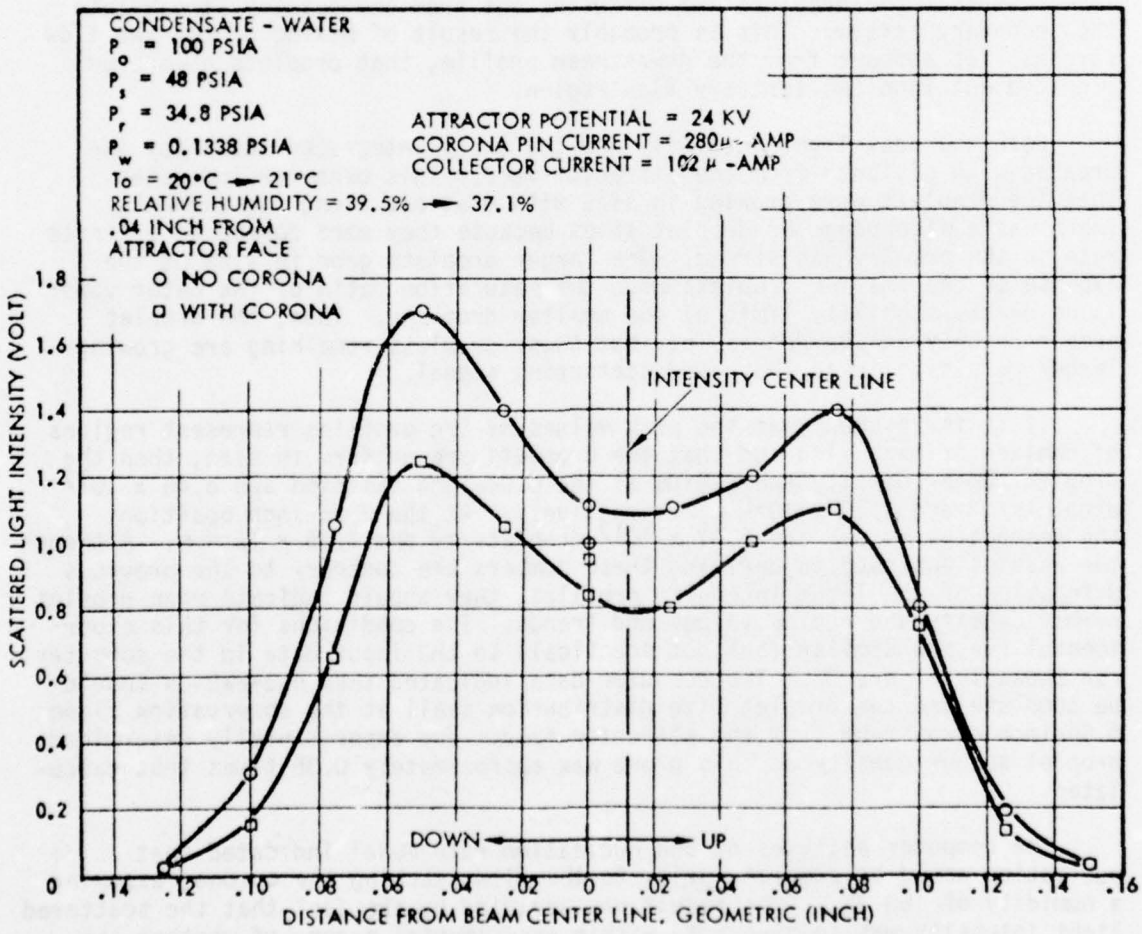

Figure 18. Scatter Light Intensity Scan Profile with and without Corona at Low Relative Humidity

4. MACH NUMBER PROFILES FROM PITOT TUBE SCANS

The Pitot traverses performed on the 1/4-inch experimental channel are shown in Figures 19 through 22. The traverses were taken inside the secondary nozzle or attractor, where the flow is confined, and in the free stream downstream of the attractor. The data shown in Figures 19 and 20 were obtained without the corona pin and those in Figures 21 and 22 were obtained with the corona pin placed at the optimum operating position.

The primary and secondary pressures and the gas temperatures were held constant during the runs. It is obvious from the skewness of the Mach number curves and the variation in tertiary pressure along the traverse that the probe perturbed the flow. The profiles of Mach number to the right of the zero position are probably fairly representative of the actual Mach numbers. This is due to the fact that the probe was moved from right to left, with respect to the figures, across the flow stream, and interference increased with probe penetration. There are slight indications of inflections in the slope of the Mach number curves which correspond to mixing regions between the primary and secondary and secondary and tertiary flows. Although skewed, these curves are adequate to assist in interpreting the light scattering experiments.

5. ELECTROHYDRODYNAMIC SPRAYING OF WATER DROPLETS

a. Analysis

Without electrical forces, water leaving a spraying needle is atomized by the supersonic air through a combination of wind- and drag-induced wave instabilities and turbulence-acoustical forces that tear the sheets of water apart and result in a range of particle sizes around 10 microns in radius. This process is quite similar to simple aspirated paint sprayers. With small electric fields present, charge is induced on the droplets when still in electrical contact with the needle, this charge being carried away with the droplets. As high electric fields are applied (approaching the gaseous breakdown strength of air), the electrical tension on the liquid exceeds the surface tension and aerodynamic forces, and the water is torn into smaller more highly charged droplets. These droplets will accelerate through large potentials to high radial velocities, but their paths will curve downstream by the drag of the air. The droplets must have less charge than the Rayleigh limit where the electric forces balance the surface tension forces. The charge will, however, be close to this limit, as these two forces dominate in the droplet formation.

All electrohydrodynamic spraying processes that we are familiar with are characterized by a close approach to this Rayleigh limit, even when the particles range from tens of Angstroms in diameter (as in glycerol colloid spraying used in electric propulsion) to hundreds of microns in diameter (as used in the charged-droplet scrubber). The work of K. Joshi of SRI, described in 1969, is completely consistent with this interpretation. His 1.0 coulomb/kilogram particle would be about 3 microns in radius, very close to the Rayleigh limit, and would have a surface field of 10^8 volt/meter, very close to the breakdown field at the pressure used. These particles

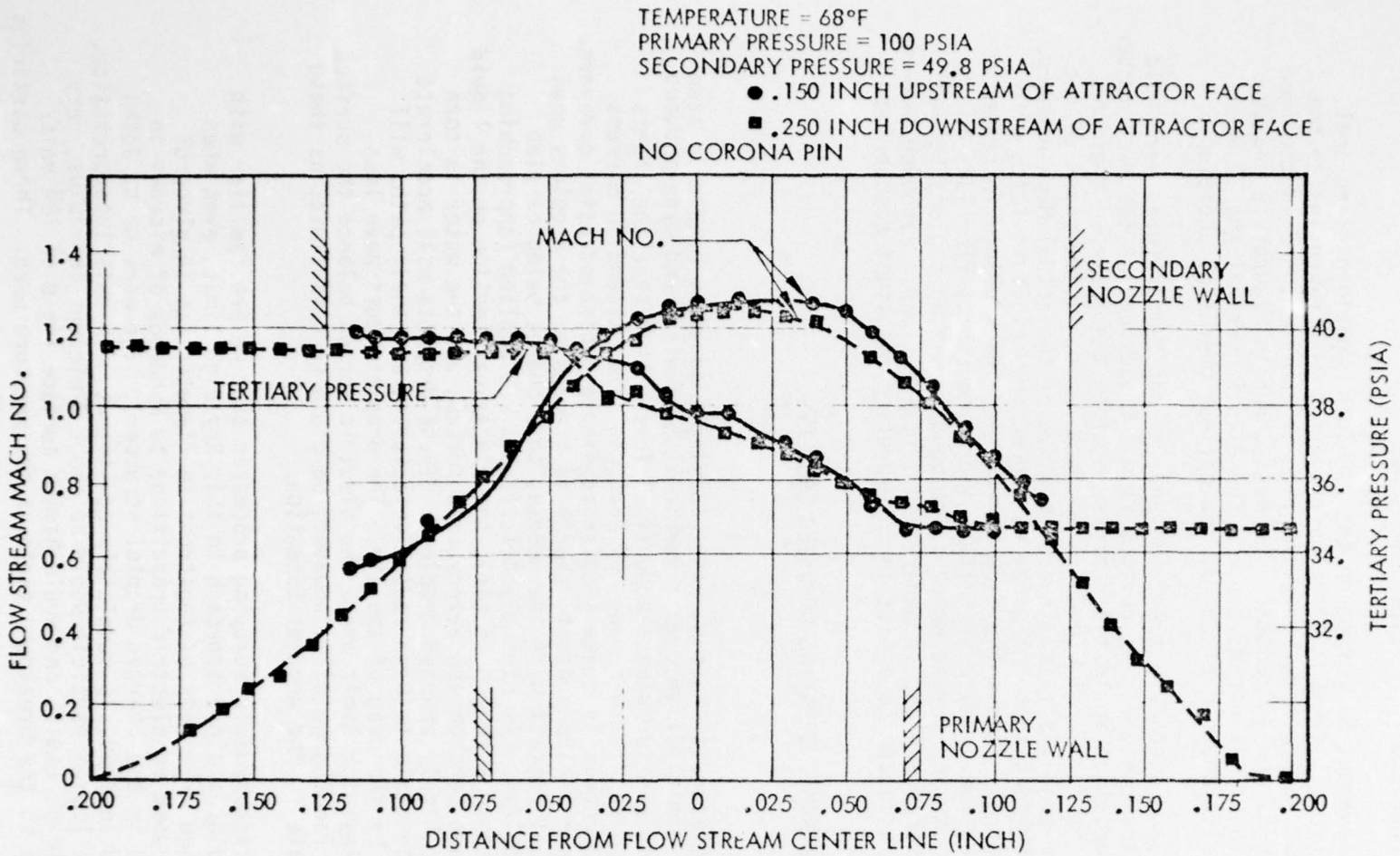

Figure 19. Air Flow Stream Mach No. and Simultaneous Tertiary Pressure Profiles with a Primary Mach No. of 1.05 and No Corona Pin. Pitot probe entered from positive direction.

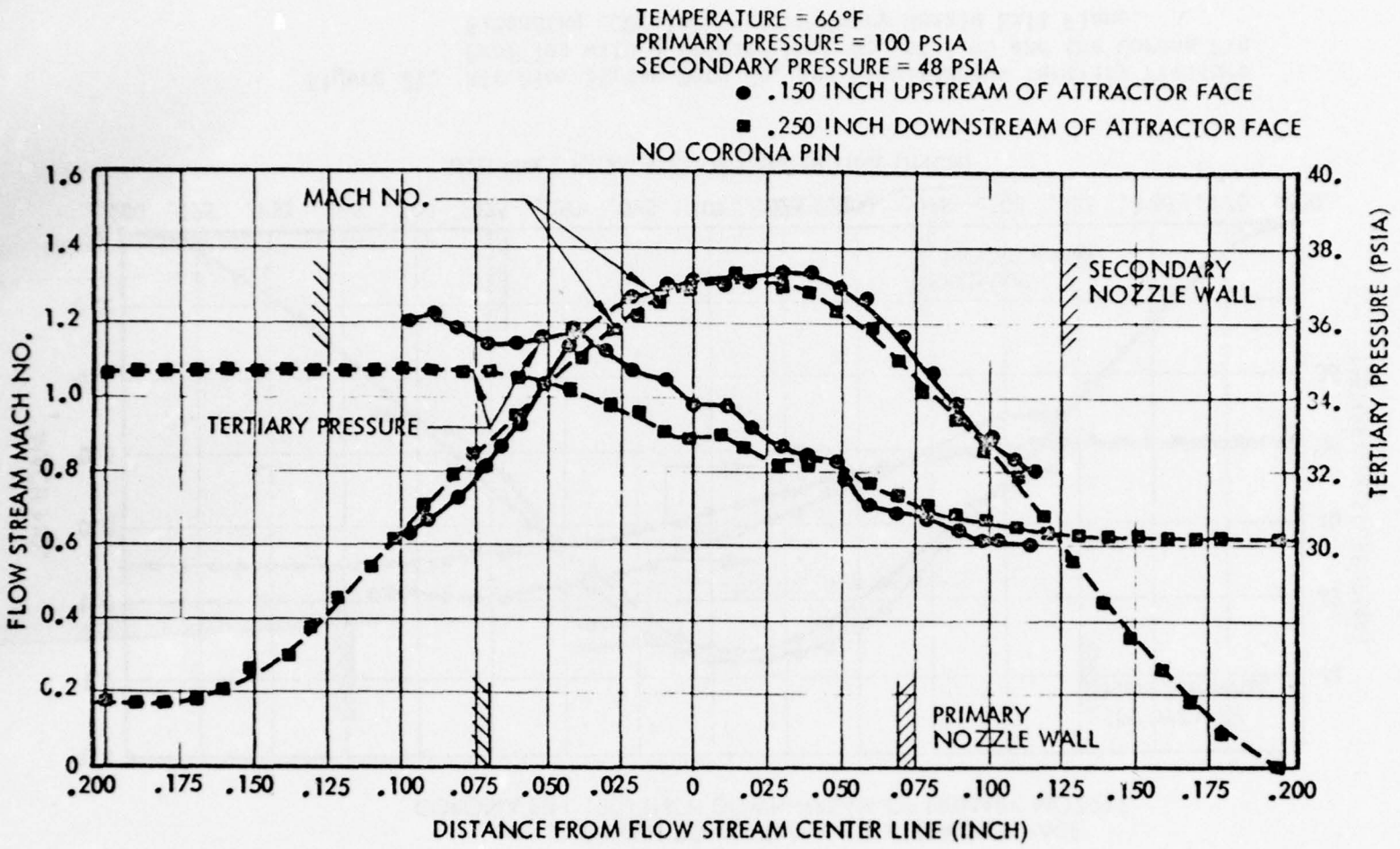

Figure 20. Air Flow Stream Mach No. and Simultaneous Tertiary Pressure Profiles with a Primary Mach No. of 1.08 and No Corona Pin. Pitot probe entered from positive direction.

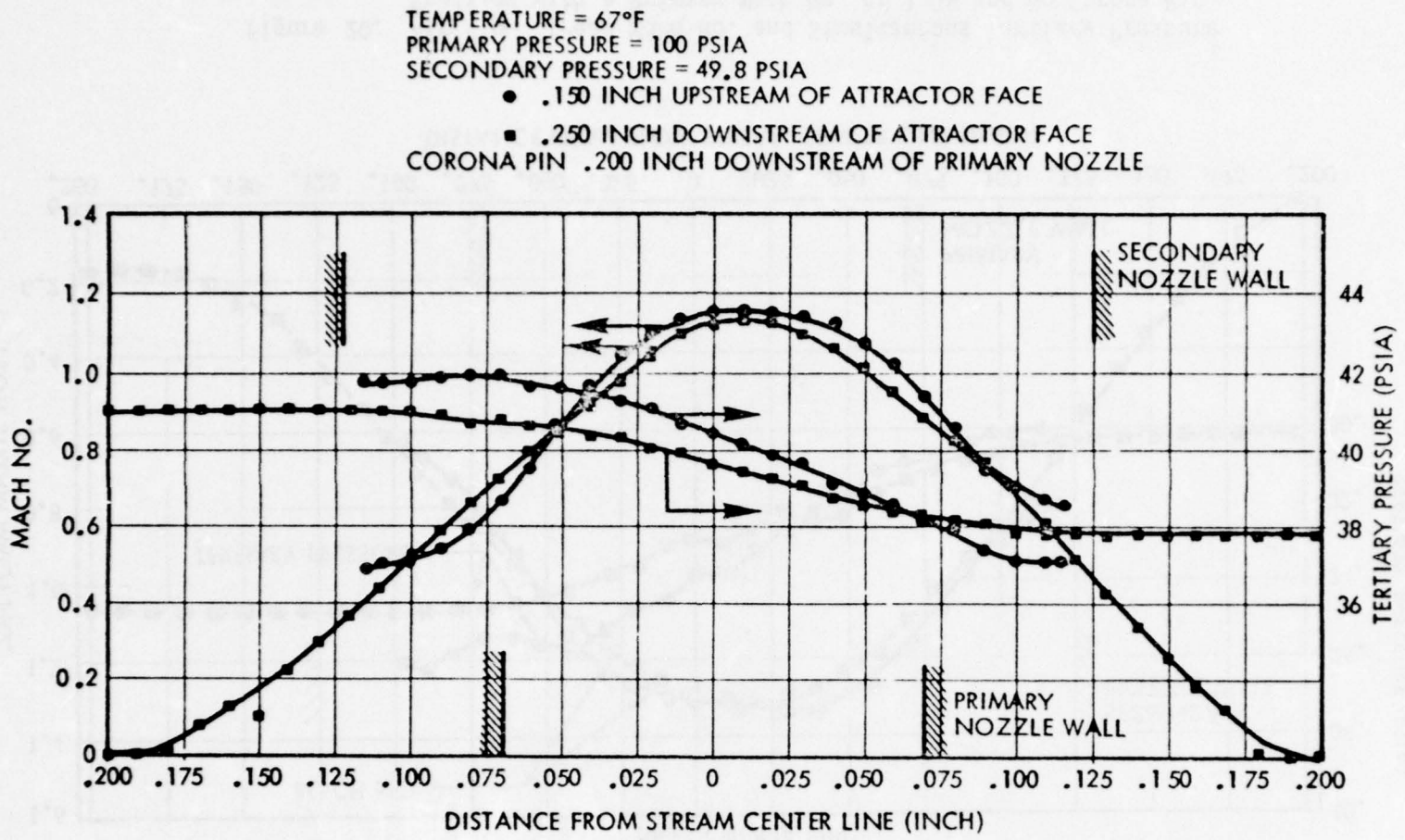

Figure 21. Air Flow Stream Mach No. and Simultaneous Tertiary Pressure Profiles with a Primary Mach No. of 1.05 and the Corona Pin Extending .200-Inch from Primary Nozzle Exit Plane.

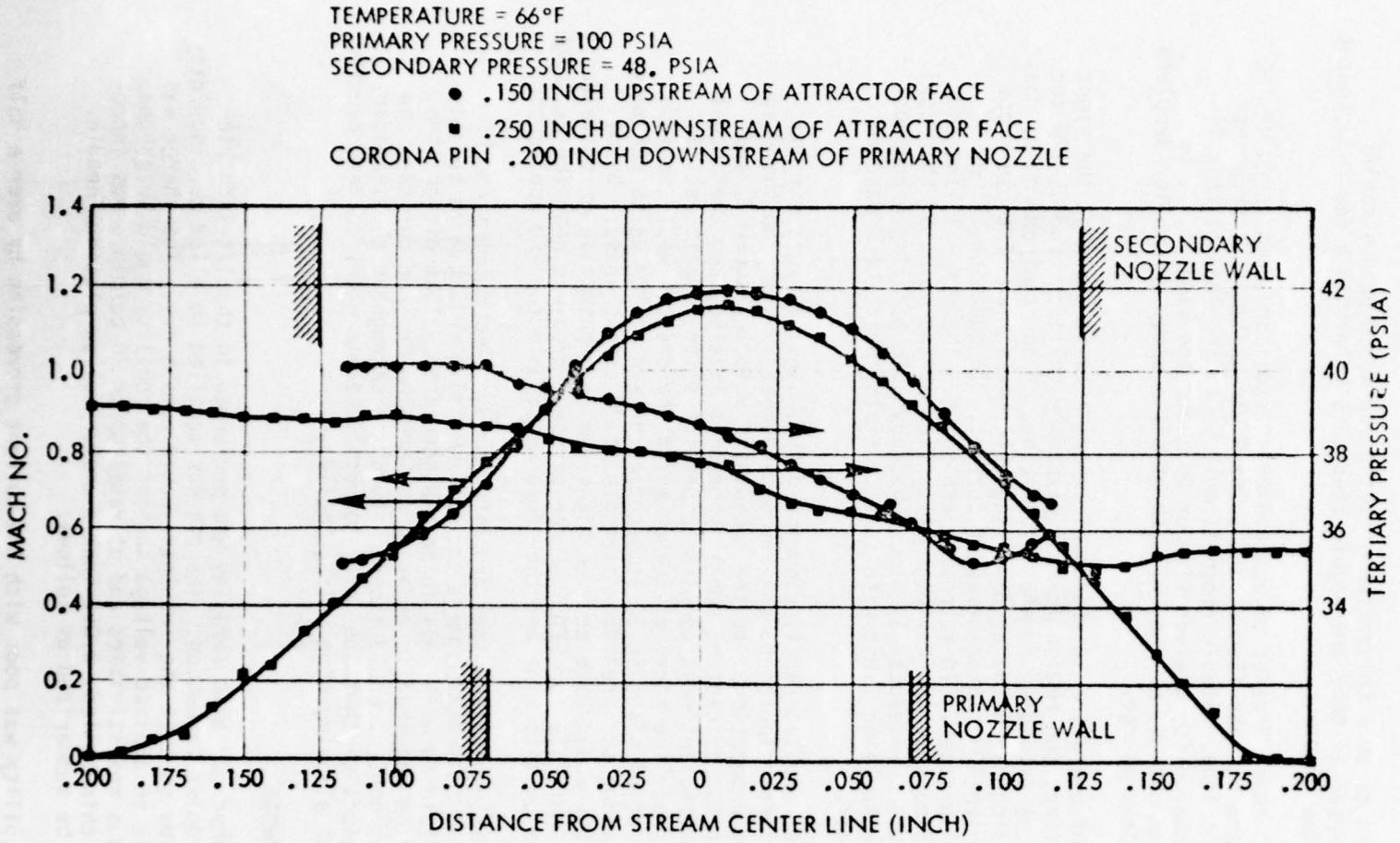

Figure 22. Air Flow Stream Mach No. and Simultaneous Tertiary Pressure Profiles with a Primary Mach No. of 1.08 and the Corona Pin Extending .200-Inch from the Primary Nozzle Exit Plane.

would be subjected to an acceleration of 10^7 g and would gain a radial velocity of 100 m/sec as they are accelerated to 5 kV within a few thousandths of an inch from the needle.

In Figure 23 three decades of water droplet radii are considered having a total charge ranging over five decades; the Rayleigh limit is shown as the lower straight line. Stable droplets must be to the left of this line, i.e., have less charge for a given size or be above the line; i.e., be larger for a given charge, or they will shoot off a spray of smaller droplets to remove the excess charge.

The region of operation in the Joshi experiments is shown at the right on the Rayleigh line; the region for the glycerine colloids used at TRW for propulsion is shown extending to the left. Lines of constant charge-to-mass ratio are shown along with the accompanying water mass flow if these drops were associated with 400 microamperes of current. In addition, lines of constant average surface field intensity are shown. The Q/M = 1 line and the $E = 10^8$ V/M line meet the Rayleigh limit line at the point of the Joshi experiment as would be expected if electrohydrodynamic spraying produced droplets near the Rayleigh limit with surface fields near the breakdown strength of the air.

At the higher droplet radii, assuming dense, high pressure air and actual droplet drift velocities, the Reynolds number is high and the drag forces, which are proportional to the radius and velocity squared, are also high so that the concept of mobility becomes invalid, and the actual changing drag coefficient must be used to predict drift velocities. In Figure 23 the curved line shows a line on which the droplet would achieve a drift velocity of 50 m/sec in 30 atmospheres of air at 10^8 volts per meter field strength (about the breakdown strength at 30 atmospheres). Below this line, droplets would have an even higher, more prohibitive drift velocity and hence not be suitable for EFD. As can be seen, droplets near the Rayleigh limit are well below this line and therefore unsuitable for EFD applications.

This analysis emphasizes that droplets made by electrohydrodynamic spraying would have too much charge and too much slip relative to the air in an electric field to work well in an EFD generator. In addition, too much water would be required in order to achieve the desired current, and the average water content would exceed saturation throughout the secondary and tertiary regions so that the insulator would become water soaked, causing breakdown and not allowing high voltage build up.

b. Experiments

Electrohydrodynamic spraying was performed in the 1/4-inch rig used to study droplet formation. The rig was modified to allow zero humidity secondary air flow so that the insulator would remain dry. The charge was collected against an applied voltage so that the mobility could be gauged. Water with various resistivities and at rates up to 20 cc/min., was introduced through a thin-walled, 0.062-inch diameter hollow platinum needle. The results can be summarized as follows:

(1) The mobility was poor with the current decreasing by over a half with additional tens of kilovolts on the collector.

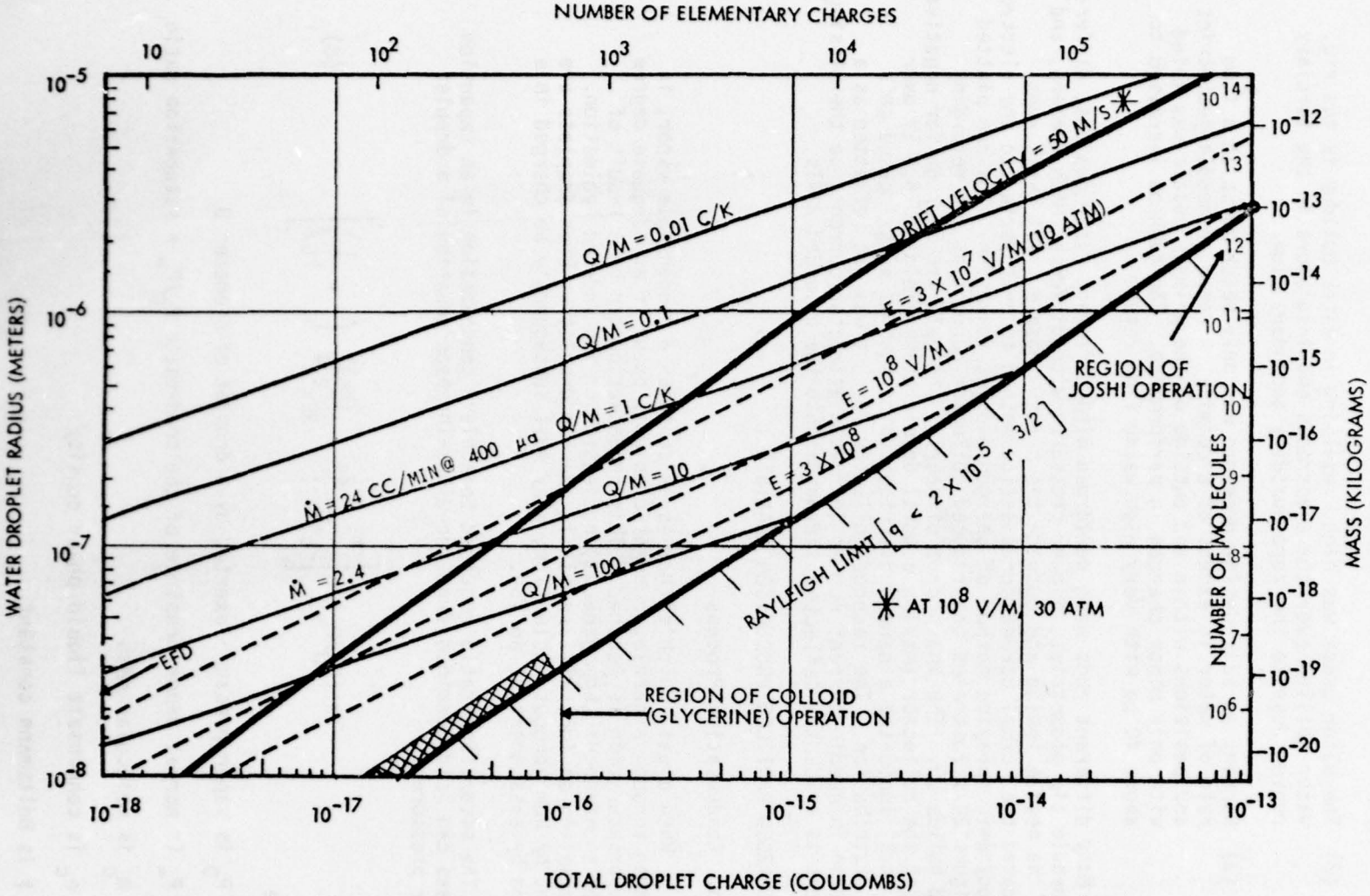

Figure 23. Relationship of Charge, Radius, Charge-to-Mass Ratio, Surface Electric Field Strength, and Rayleigh Limit for Water Droplets.

(2) The water usage was high, resulting in water buildup in the rig. Water spilled over the electrodes and insulators in the tertiary region despite the zero humidity secondary flow.

(3) Current at half design pressure was only about 20 μa at a flow rate of water in excess of 6 cc/min. A range of needle geometries and positions within and outside of the primary nozzle was tried with only minor changes in performance. The current increased to about 40 μa with very high water flow rates.

Many different runs were performed with different water dopants, different needle tip geometries, higher pressures with different Mach numbers, and with the needle inside and outside the primary nozzle. All these runs indicated the normal corona-condensation method to be superior to the electrohydrodynamic spraying method of charged droplet formation. The run plotted in Figure 24 illustrates the reduced collector current as the retarding field builds up. The sharp drop of nearly one half the current for negative 8 kV on the collector (making a total decelerating field of 26.5 kV over 0.75 inch) indicates a narrow distribution of species superimposed on a wide distribution. The reduced collector current was not reflected as a decrease in needle current nor an increased attractor current, so the missing current is evidently deflected sidewards onto the grounded walls.

6. CHARGED PARTICLE PRODUCTION ANALYSIS

a. Condensation Process

When a gas, which either is or contains a condensible vapor, is expanded through a nozzle, condensation will occur if an adequate degree of supersaturation is reached. This condensation can be a result of either spontaneous (homogeneous) nucleation or ion induced nucleation. Condensation on ions will result in charged droplets. When droplets are formed by homogeneous nucleation, they must subsequently be charged in a corona by attachment of an ion.

The saturation ratio required to achieve condensation in an expansion process can be determined from the Gibbs-Thompson equation of a droplet vapor pressure:

$$\ln (P_D/P_\infty) = \left[\frac{m_c}{\rho_c kT} \frac{2\sigma}{r} - \frac{(ne)^2}{32\pi^2 r^4} \left(1 - \frac{1}{\varepsilon_D}\right)\right] \qquad (6)$$

Where

P_D is vapor pressure exerted by a droplet of diameter D

P_∞ is normal vapor pressure of the condensate P_c/P_∞ = saturation ratio

m_c is molecular mass

ρ_c is condensate liquid phase density

k is Boltzmann constant

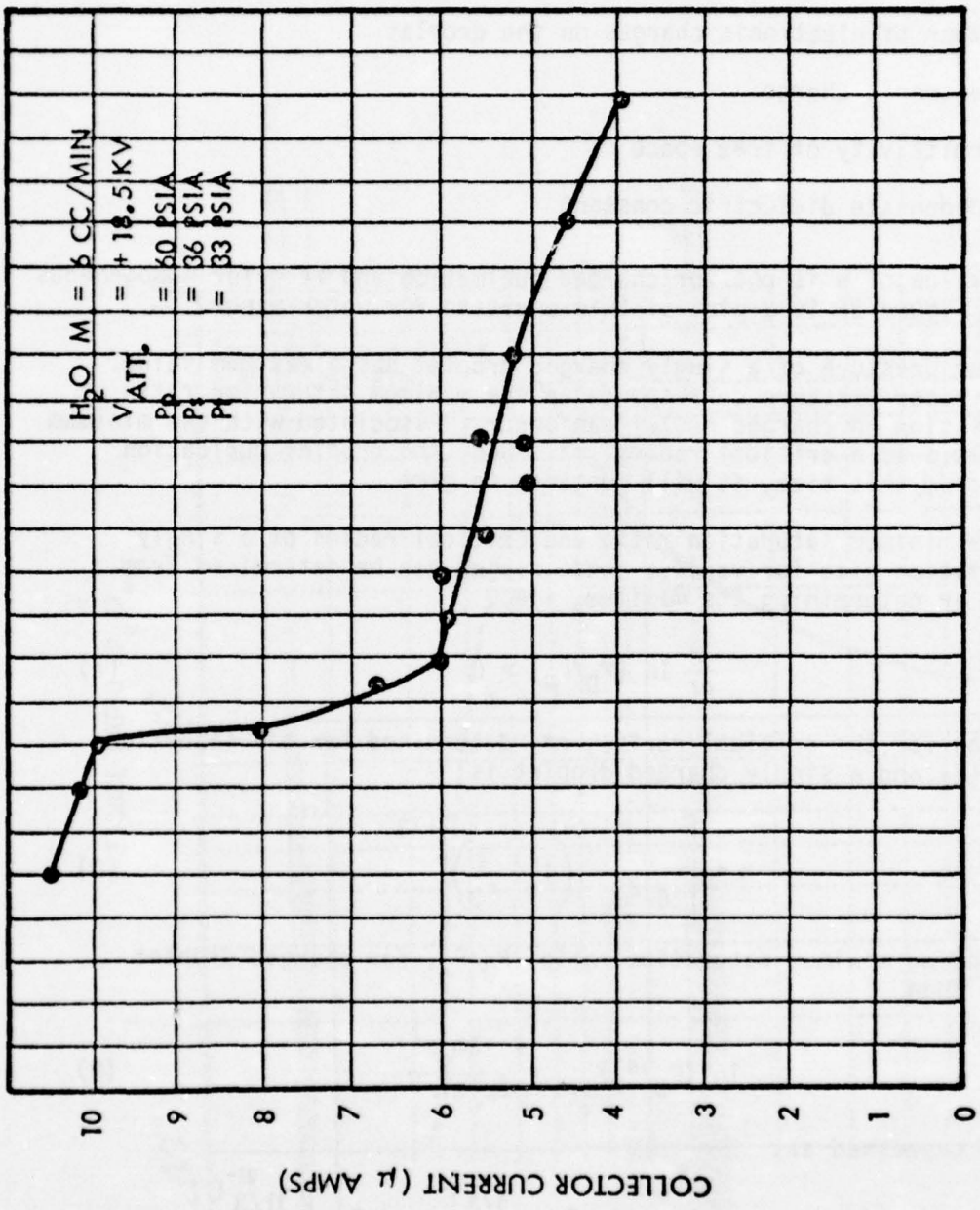

Figure 24. Current of Electrohydrodynamically Sprayed Water Droplets Versus Retarding Collector Voltage.

T is temperature

σ is surface tension

r is radius

n is number of electronic charges on the droplet

e is electronic charge

ε is permittivity of free space

ε_D is condensate dielectric constant

The nominal value of n is one for charged nucleation and zero for homogeneous nucleation. Figure 25 is a plot of this equation for water vapor.

The vapor pressure of a singly charged droplet has a maximum value. This maximum vapor pressure corresponds to the minimum saturation ratio at which condensation on charged nuclei can occur. Associated with the minimum saturation ratio is a critical radius, r*. Once the droplet nucleation site has reached this size, it will continue to grow.

Both the minimum saturation ratio and critical radius of a singly charged nucleation site for various condensibles can be determined from Equation (6) by determining its maximum, i.e.,

$$\frac{d}{dr} \ln (P_D/P_\infty) = 0 \tag{7}$$

The expression for the critical radius, r*, determined for the condition of Equation (7) and a singly charged droplet is

$$x = \left[\frac{e^2}{16\pi^2\sigma\varepsilon}\left(1 - \frac{1}{\varepsilon_D}\right)\right]^{1/3} \tag{8}$$

The corresponding minimum saturation ratio, P_D/P_∞, for charged droplet formation is then

$$\ln (P_D/P_\infty)_{min} = \frac{3m_c\sigma}{2\rho_c kTr^*} \tag{9}$$

which can be expressed as

$$\ln (P_D/P_\infty)_{min} = \frac{3m_c\sigma}{2\rho_c kT}^{4/3}\left[\frac{16^2\varepsilon}{e^2\left(1 - \frac{1}{\varepsilon_D}\right)}\right]^{1/3} \tag{10}$$

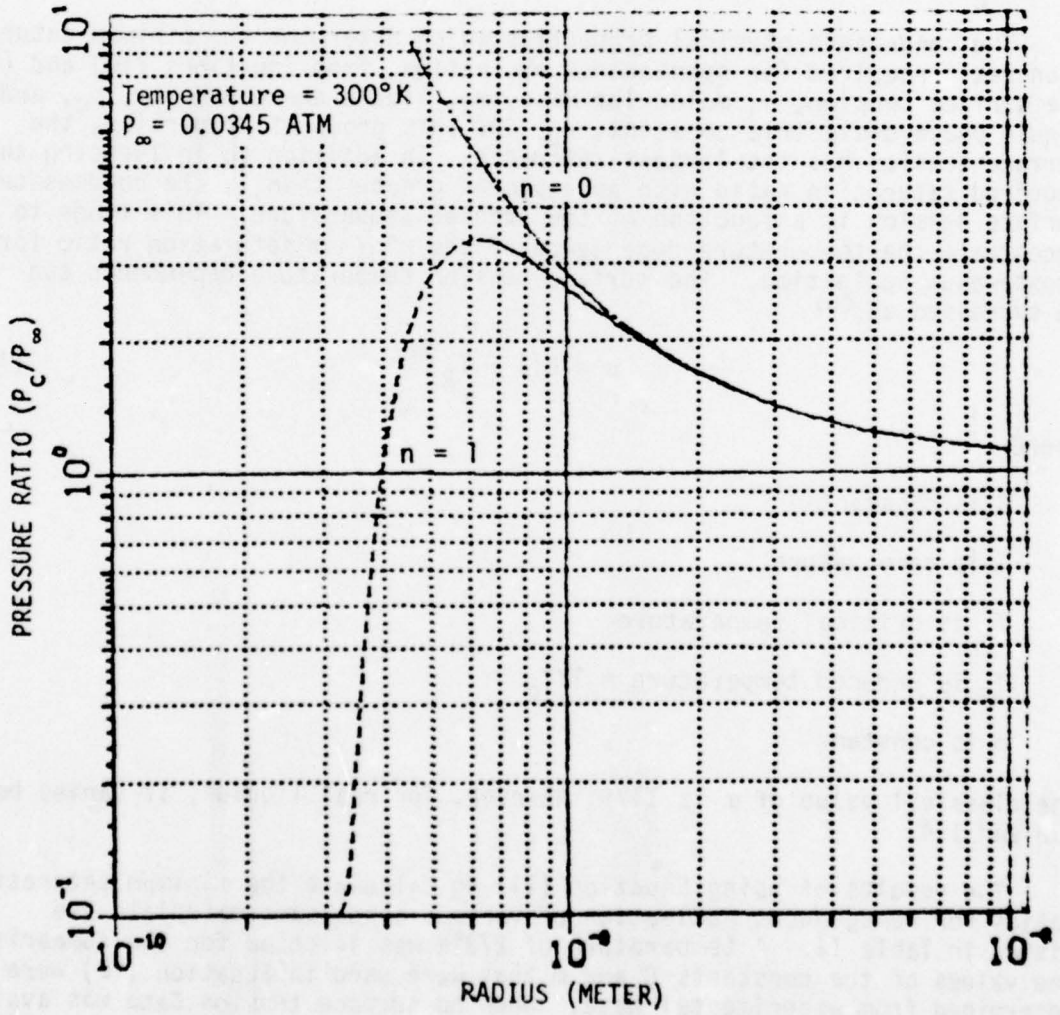

Figure 25. Water Droplet Vapor Pressure as a Function of Droplet Radius

The vapor pressure curve for an uncharged droplet has no maximum; however, there is a minimum saturation ratio at which homogeneous nucleation and droplet growth will occur. The data from cloud chambers, using water, indicate that the critical radius required for condensation of charged and uncharged nucleation sites is approximately the same. By assuming that the critical radii are identical, then the minimum saturation ratio for homogeneous nucleation is

$$\ln (P_c/P_\infty)_{min} = \frac{2\bar{m}_c\sigma}{\rho_c kT}^{4/3} \left[\frac{16\pi^2\varepsilon}{e^2 \left(1 - \frac{1}{\varepsilon_D}\right)} \right]^{1/3} \qquad (11)$$

where P_c is condensate pressure.

The condensate physical properties which determine the minimum saturation ratio required for spontaneous nucleation, from Equations (10) and (11), are surface tension, σ, molecular mass, m_c, liquid phase density, ρ_c, and liquid phase dielectric constant, ε_D. Of this group of properties, the surface tension has the largest influence. In addition to influencing the required saturation ratio with an exponent greater than 1, the condensate surface tension is a function of the droplet temperature. This tends to accentuate the temperature dependence of the minimum saturation ratio for spontaneous nucleation. The surface tension temperature dependence can be expressed as:[c]

$$\sigma = C(1 - T_R)^m \qquad (12)$$

Where

C is constant

T is temperature

T_c is critical temperature

T_R is reduced temperature = T/T_c

m is constant

The classical value of m is 11/9; however, for real liquids, it varies between 0.8 and 1.4.

The results of using Equation (11) to calculate the minimum saturation ratios for homogeneous nucleation of various condensate materials are listed in Table II. A temperature of 273°K was selected for the comparison. The values of the constants C and m that were used in Equation (12) were determined from experimental data. When no surface tension data was available, the corresponding state correlation proposed by Brock and Bird* was used to

Table II. Condensate Saturation Ratios (Homogeneous Nucleation)
Temperature: 273°K

Material	Surface Tension (Newton/Meter)	Minimum Saturation Ratio $(P_c/P_\infty)_{min}$
Water	0.07564	6.80
N_2O	0.00505	1.15
CO_2	0.00450	1.14
Freon 113	0.0200	13.20
Freon 11	0.0213	9.27
Freon 21	0.0224	5.50
Freon 114	0.0151	6.00
Hg	0.501	3.8×10^8

determine the constant, C. The value of the exponent, m, was taken as the classical. As can be seen from Table II, the freons, which are typical of organic materials with high molecular mass and relatively low liquid phase density, have a high minimum saturation ratio for spontaneous nucleation. Mercury has an extremely high saturation ratio for condensation, due to its large surface tension.

In Figure 26 three pressure curves are plotted versus temperature for water. On the right is the standard saturation vapor pressure curve showing the pressure of water vapor necessary to condense on a planar surface of water. The left curve shows the much higher pressure necessary to condense droplets when no nucleation sites are present. The middle curve is the lower pressure needed if charge nucleation sites are available. Also included in this figure are the adiabatic expansion curves for the primary and secondary flow in a typical 1/24-inch EFD channel at 80% humidity and 180°F. Note that homogeneous nucleation commences inside the primary nozzle in the subsonic flow.

Figure 27 shows a similar expansion curve in pure steam. The expansion characteristics are somewhat similar to water vapor in air. However, the secondary flow would have to be cooled to insure a saturated condition after expansion to prevent droplet evaporation.

b. Kinetic Conditions - Nucleation and Growth Rates

The thermodynamic conditions of the condensate system will determine the necessary end points in the expansion process for operation in an EFD channel. The rate at which equilibrium conditions are approached or reached is a kinetic problem. The two condensation processes which influence the effectiveness of a condensate in an EFD channel are nucleation rate, and droplet growth rate.

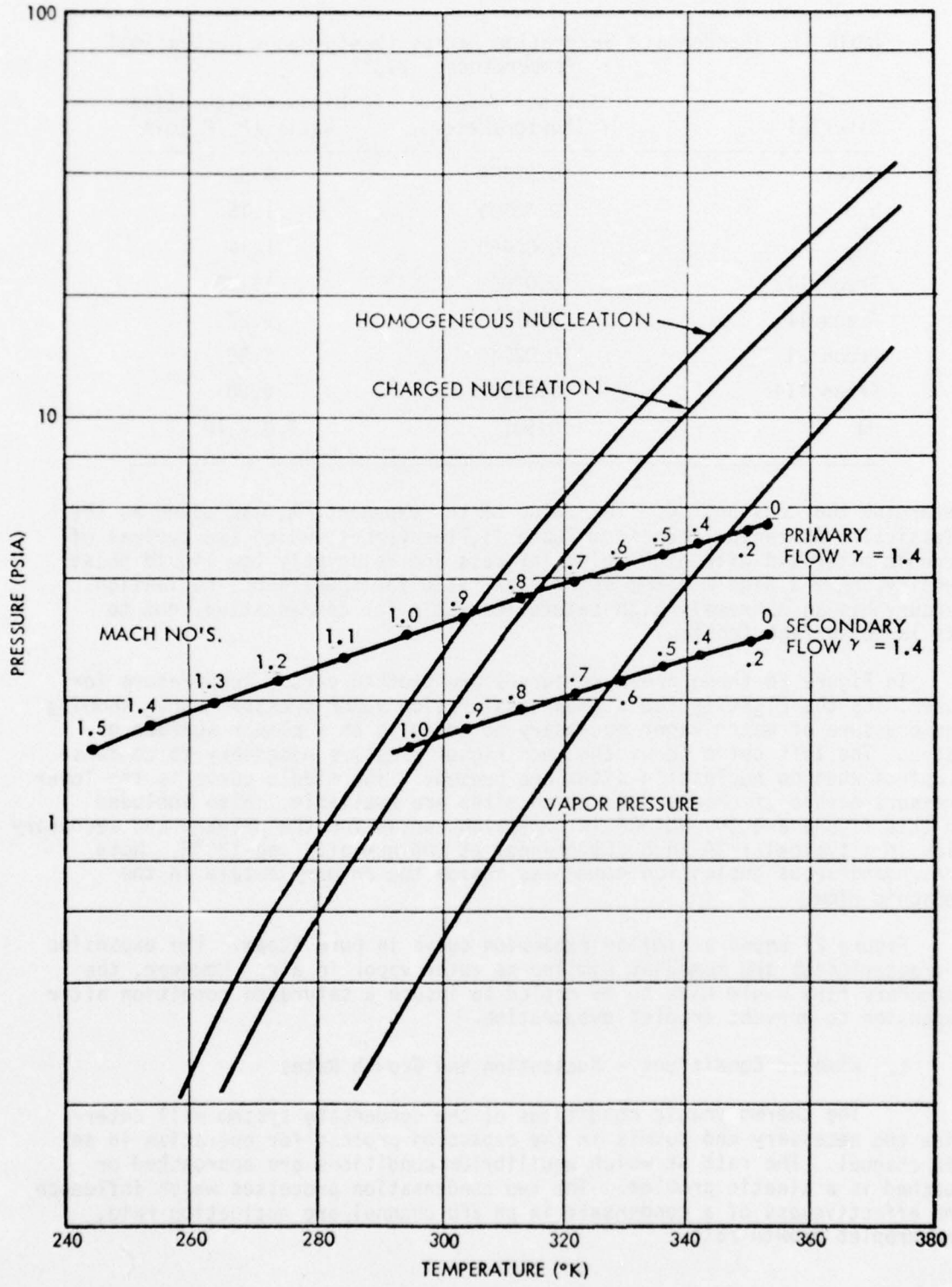

Figure 26. Critical Condensation Pressure For Water

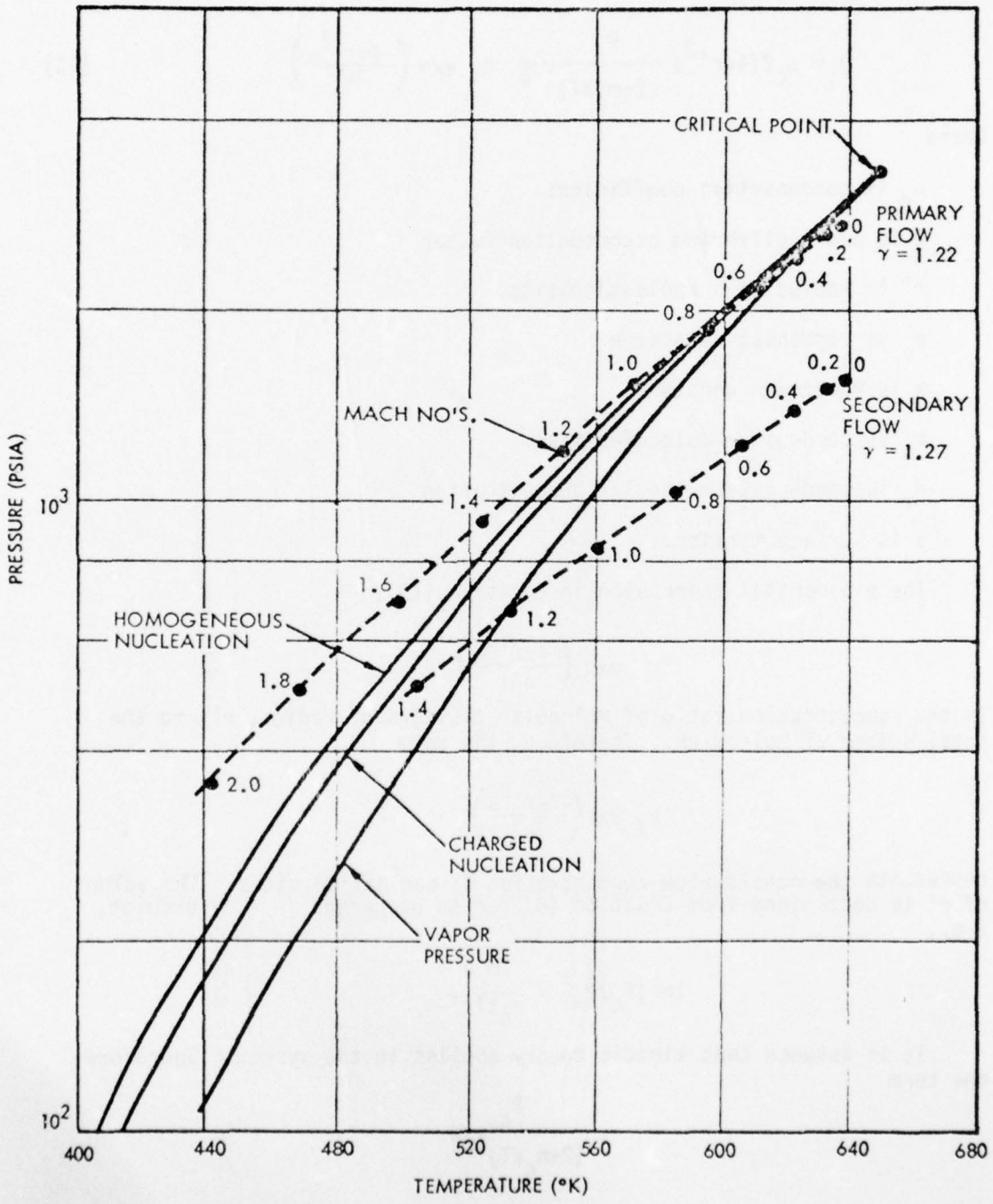

Figure 27. Expansion of Near Critical Water Vapor

The statistical approach[d] was used to characterize spontaneous nucleation. The resulting equation which describes the nucleation rate, J, is:

$$J = \alpha_c Z(4\pi r'^2) \frac{p_c}{(2\pi m_c kT)^{1/2}} n_i \exp\left(\frac{-4\pi r'^2 \sigma}{3kT}\right) \qquad (13)$$

Where

α_c is condensation coefficient

Z is non-equilibrium accomodation factor

r' is radius of a nucleation site

p_c is condensate pressure

k is Boltzmann constant

m_c is condensate molecular mass

n_i is condensate molecular concentration

σ is surface tension.

The exponential expression in Equation (13),

$$\exp\left(\frac{-4\pi r'^2 \sigma}{3kT}\right)$$

is the concentration ratio of molecular clusters of radius, r', to the total number of molecules. Therefore, the term

$$n_i \exp\left(\frac{-4\pi r'^2 \sigma}{3kT}\right)$$

represents the equilibrium concentration of nucleation sites. The value of r' is determined from Equation (6) for an uncharged (n = 0) droplet, i.e.,

$$\ln (P_c/P_\infty) = \frac{2m_c\sigma}{\rho_o kTr'}$$

It is assumed that kinetic theory applies in the system. Therefore, the term

$$\frac{p_c}{(2\pi m_c kT)^{1/2}}$$

represents the molecular flux of condensate within the system. The term, $4\pi r'^2$, is the surface area of the molecular cluster and the product of this area and the molecular flux is the impingement rate of molecules on the molecular cluster.

The term, α_c, is the classical condensation coefficient which is the fraction of the impinging molecules that stick to the cluster.

The factor, Z, in Equation (13) accounts for the probability that a nucleation site can lose a molecule, as well as gain, and become subcritical. In the former case, the cluster would not become a nucleation site which could grow into a droplet.

The product of the terms described yields the rate at which critical size molecular clusters have gained molecules and become growing droplets, and is defined as the droplet nucleation rate.

The Z term in Equation (13) can be expressed as

$$Z = \frac{m_c}{2\pi r'^2 \rho_c} \left(\frac{\sigma}{kT}\right)^{1/2} \tag{14}$$

Where ρ_c is condensate liquid phase density.

With this expression for Z and

$$n_1 = \frac{p_c}{kT} ,$$

Equation (13) can be expressed as

$$J = \left(\frac{\alpha_c}{\rho_c}\right)\left(\frac{p_c}{kT}\right)^2 \left(\frac{2\sigma m_c}{\pi}\right)^{1/2} \exp\left(\frac{-4\pi r'^2 \alpha}{3kT}\right) \tag{15}$$

The growth rate of a droplet, using the kinetic theory flux is

$$\frac{dr}{dt} = \frac{m_c \dot{N}}{\rho_c} \tag{16}$$

Where $\dot{N}$ is net molecular flux density to the droplet surface.

The expression for $\dot{N}$ is

$$\dot{N} = \frac{(\alpha_c p_c - \alpha_e p_D)}{(2\pi m_c kT)^{1/2}} \tag{17}$$

Where α_e is evaporation coefficient and p_D is vapor pressure of the droplet.

The value of p_D for uncharged droplets is determined from Equation (6) with $n = 0$.

The rate at which condensate is removed from the vapor phase can be determined from a mass balance on the system. The total condensate mass in a unit volume is constant except for that lost due to expansion as can occur in a flow process. With these conditions, the loss rate of condensate vapor molecules, $\frac{-d}{dt} n_v$, is

$$\frac{-dn_v}{dt} = \frac{n_v}{V} \frac{dV}{dt} + \int_0^\infty N(r)\, 4\pi r^2\, \dot{N}(r) \tag{18}$$

Where n_v is molecular concentration of condensate, V is volume and N(r) is concentration of droplets of radius, r. Equation (18) can be written in terms of distance traveled in a flow process. With the following substitutions:

$$v = \frac{dx}{dt}$$

and

$$V = \frac{1}{\rho}$$

Where v is stream velocity and ρ is stream density. Equation (18) can be expressed as

$$\frac{dn_v}{dx} = \frac{1}{\rho} \frac{d\rho}{dx} - \frac{4\pi}{v} \int_0^\infty N(r)\, \dot{N}(r)\, r^2 dr \tag{19}$$

In terms of the condensate pressure, p_c, Equation (19) is

$$\frac{dp_c}{dx} = \frac{kT}{\rho} \frac{d\rho}{dx} - \frac{4\, kT}{v} \int_0^\infty N(r)\, \dot{N}(r)\, r^2 dr \tag{20}$$

Through the simultaneous solution of Equations (15), (16) and (19), the droplet size and number density can be determined as a function of travel along the channel. A computer analysis was performed for four different channel conditions. The condensate was water dispersed in a working fluid with a $\gamma = 1.4$. The following simplifying assumptions were made:

- Gas stream gradually expanded to Mach number = 1.24 at an angle of 4° degrees
- Droplets in thermal equilibrium with working fluid

- No sensible heat effects due to condensation heat, i.e., working fluid remained at constant temperature
- Condensation and evaporation coefficients equal to unity.

The three channel conditions were:

Inlet Primary Water Pressure (psia)	Inlet Temperature (°F)	Channel Geometry (inches)
1.353	120	1/12
5.416	175	1/24
21.66	245	1/48
.146	70	1/4

The results of the analysis are presented in Figures 28 through 32. The conditions are chosen to match the experimental conditions. The first three were used to predict the droplet size and density in the generator experiment. The fourth set of conditions is for low relative humidities used in the 1/4-inch charged droplet experiment, to correlate with the onset of charged nucleation.

A stepwise analysis was performed along the flow lengths. These overall lengths were divided into 41 increments over which the processes of nucleation and droplet growth within a specific droplet size occurred at a constant rate. The number of droplet size ranges corresponded initially to the number of increments over which nucleation occurred. Nucleation would stop when the saturation ratio of the condensate equaled that defined by Equation (11).

The results in Figures 28, 29, 30 and 31, for a relative humidity of 80% and a final primary Mach number of 1.24, indicate that the droplet nucleation is complete before the end of the corona pin is reached. Therefore, under these inlet conditions, the droplet nucleation process is completely spontaneous.

The results shown in Figure 32, which are typical of low humidity conditions in the 1/4-inch channel, indicate that nucleation is still progressing at a rapid rate at a distance of 0.56-inch from the primary nozzle. This has been verified experimentally, as discussed previously, since this location is within the range of the closest view plane of the scattering experiment. Because of the low density in the corona region, the major portion of the charge is carried by heterogeneously nucleated droplets (droplets nucleated on the ions). Charged droplets formed by this method have a high mobility for a considerable time period and would probably result in high, unstable attractor currents.

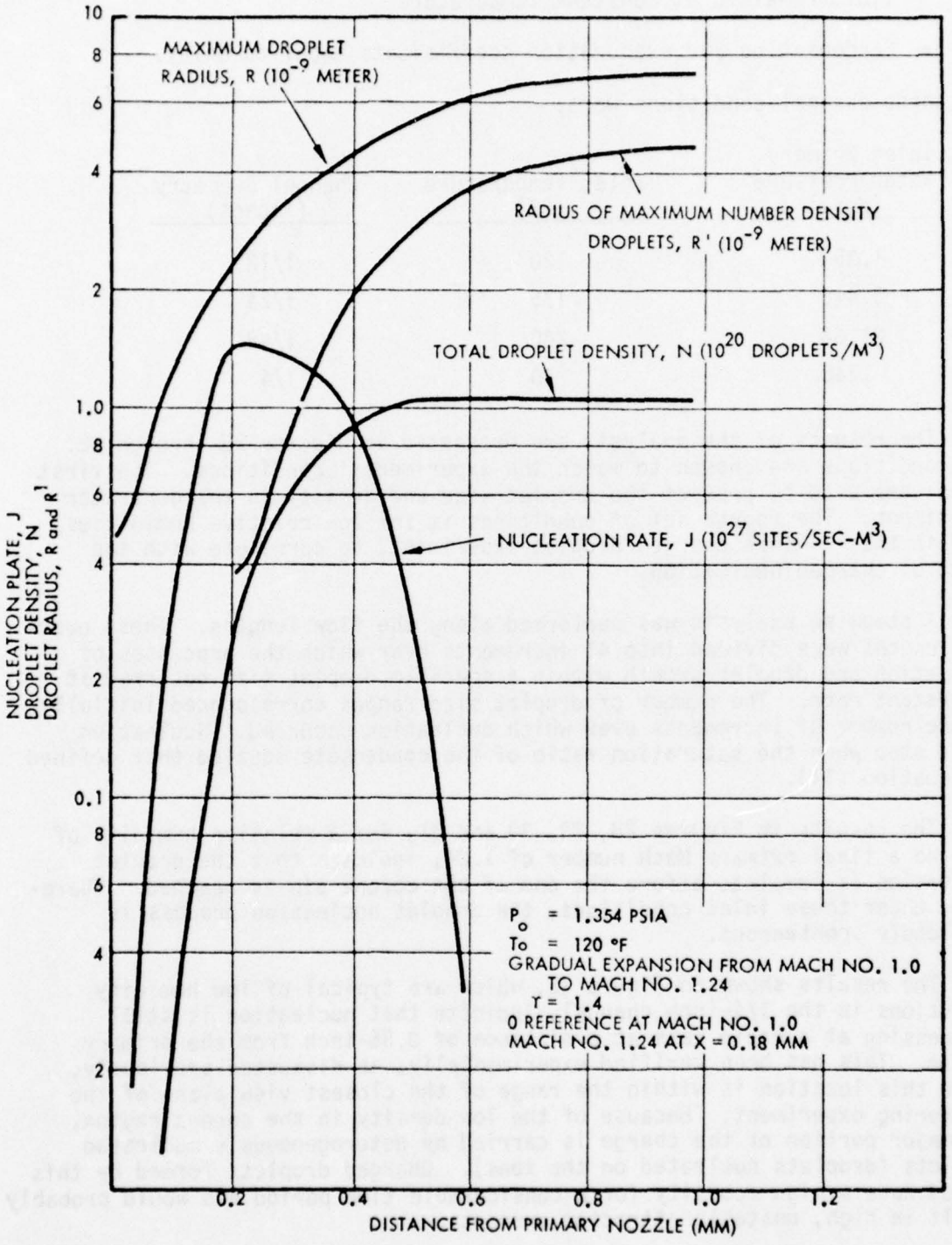

Figure 28. Condensation Kinetics in a 1/12 Inch Channel with Gradual Expansion (80% Relative Humidity)

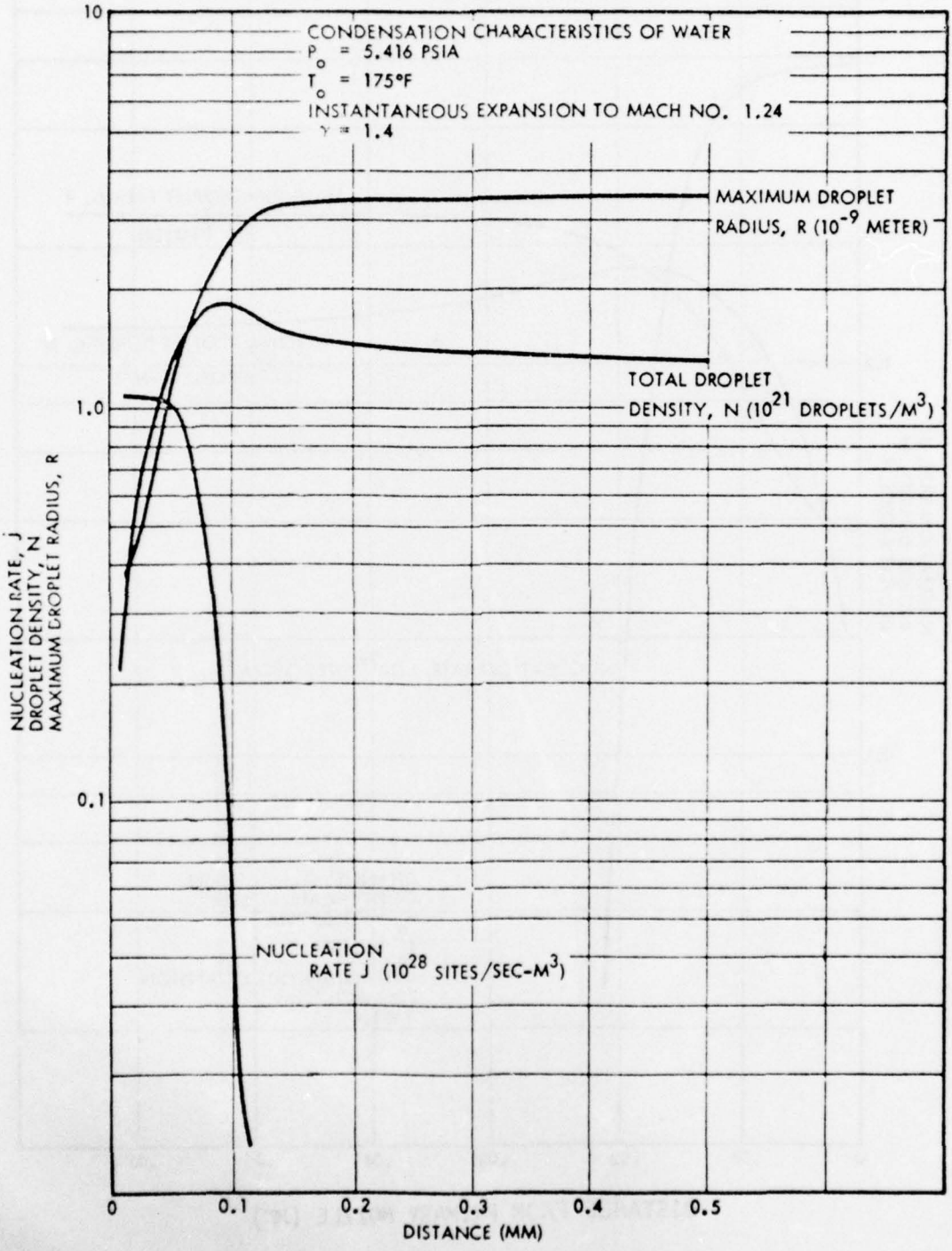

Figure 29. Condensation Kinetics in a 1/24 Inch Channel

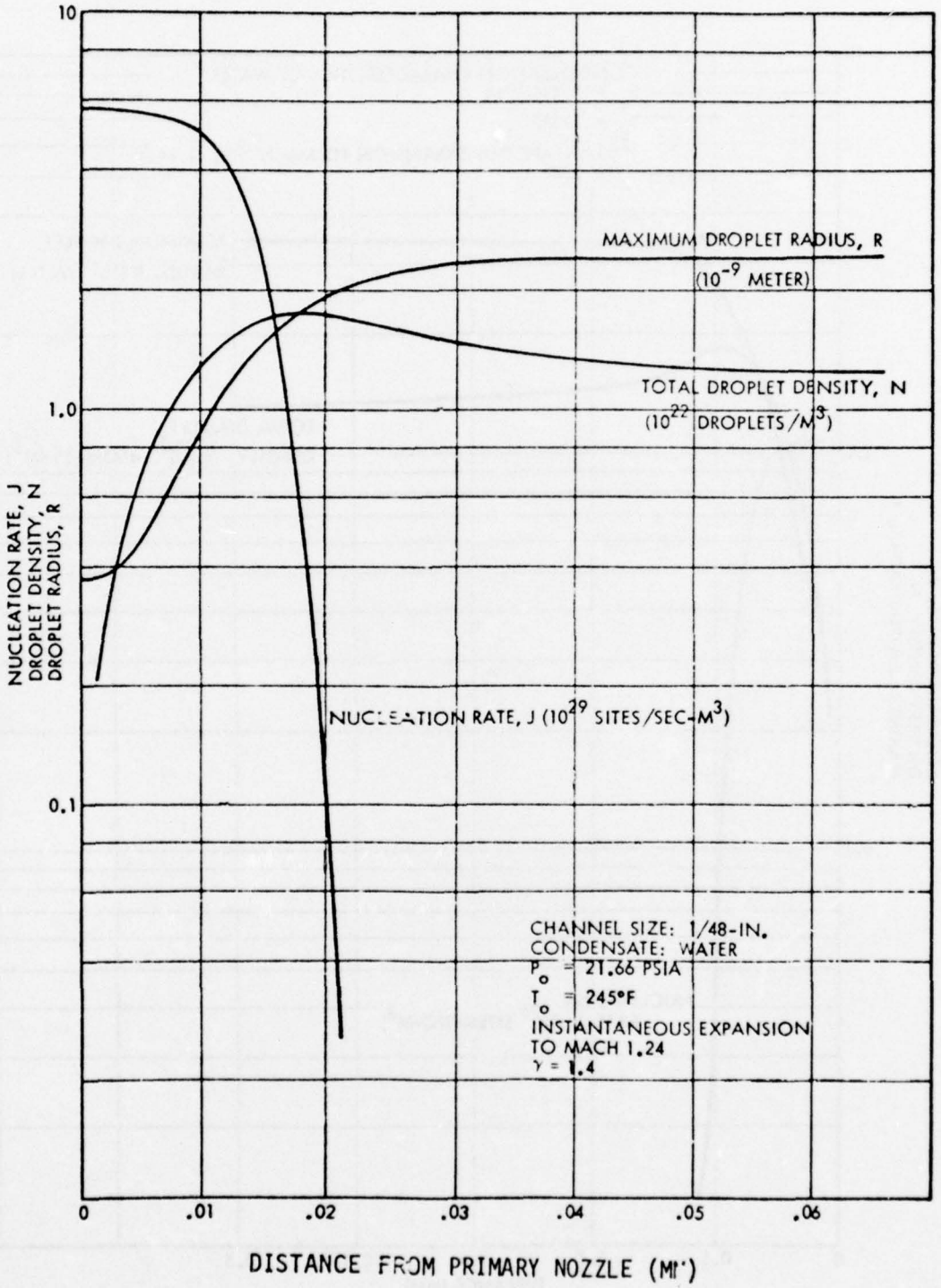

Figure 30. Computer Predicted Drop Size and Density at 245°F. This is the upper range of water used in the 1/48 inch geometry.

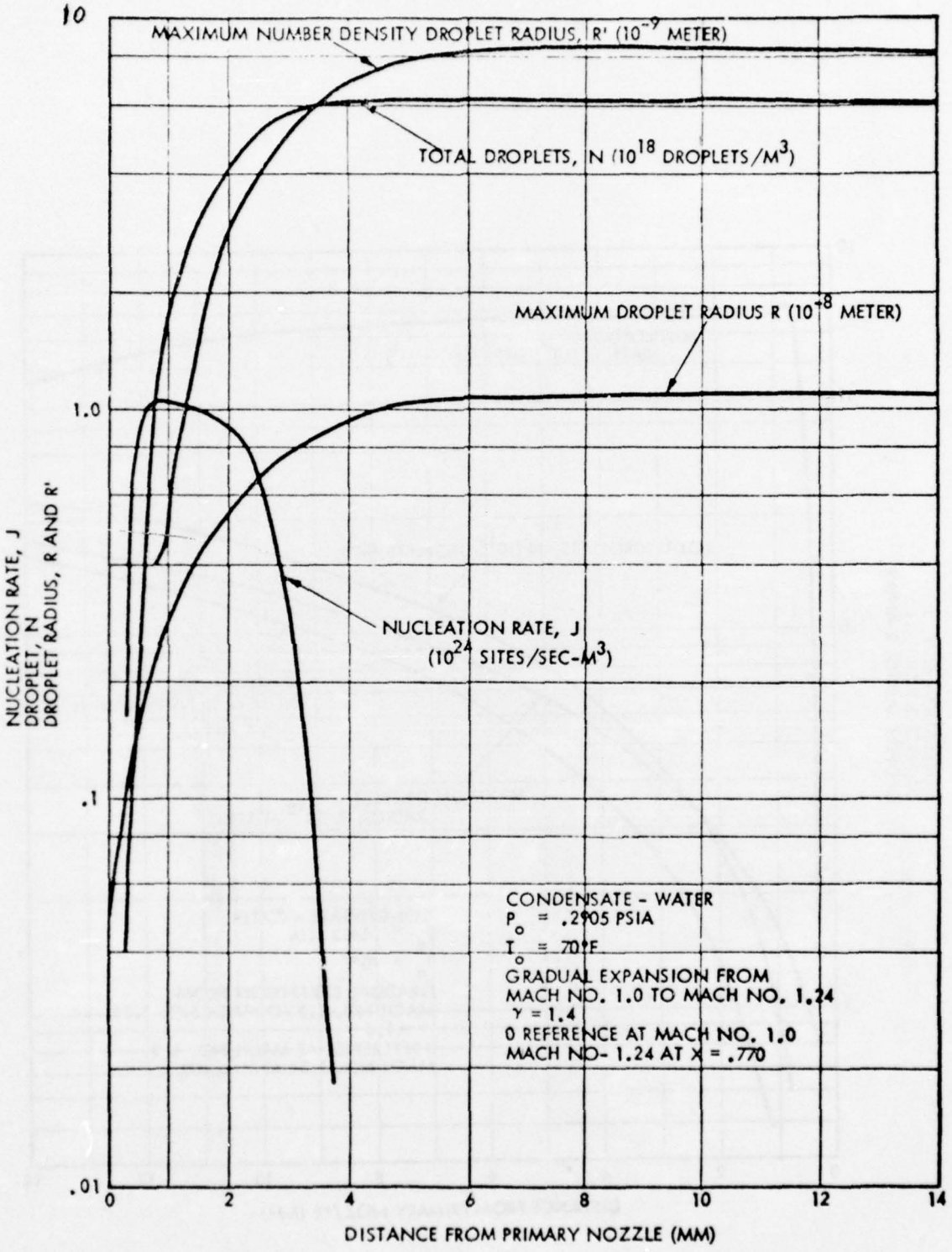

Figure 31. Condensation Characteristics of Water at 70°F, Relative Humidity 80% and Mach 1.24

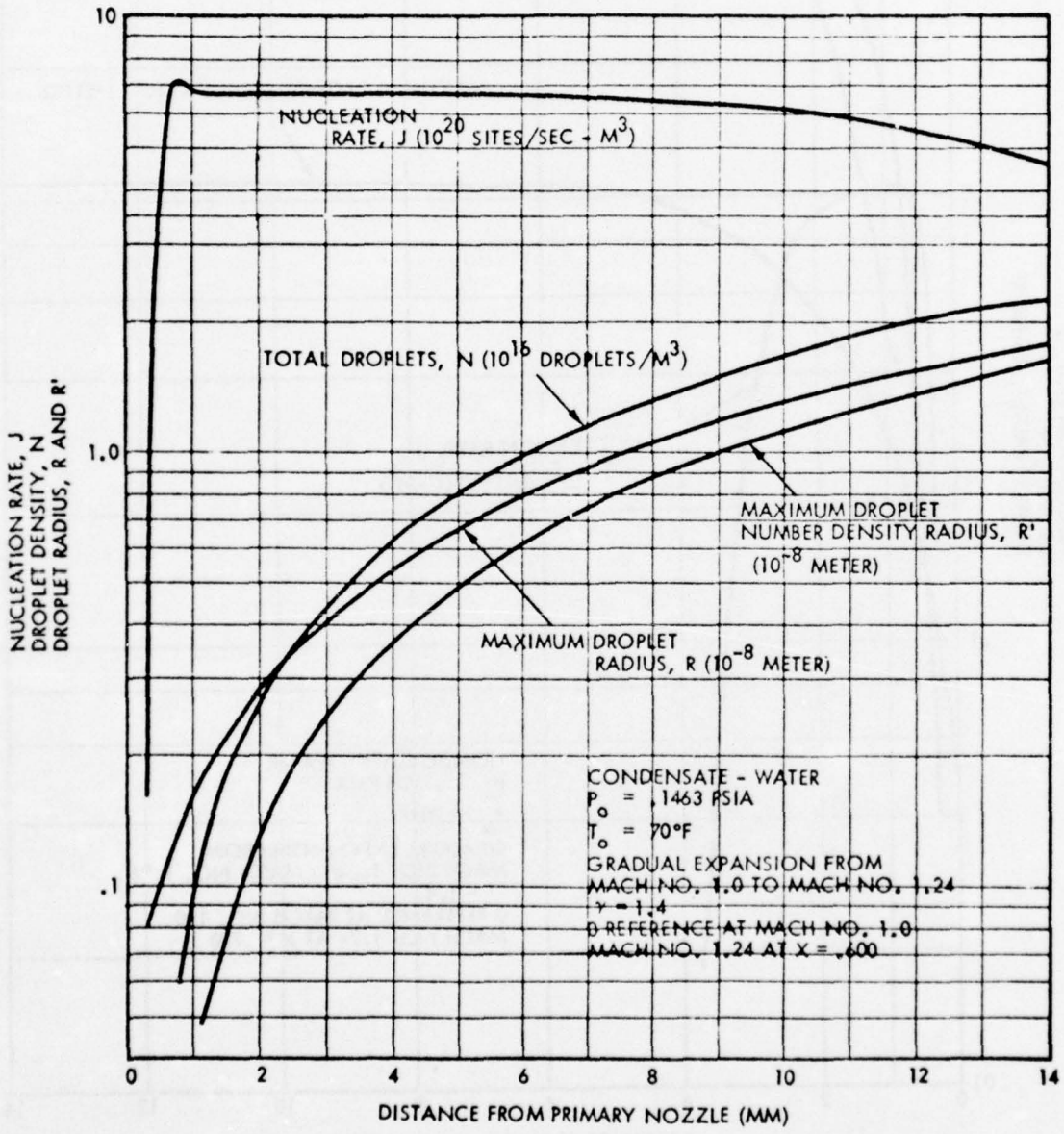

Figure 32. Condensation Characteristics of Water at 70°F, Relative Humidity 40.3% and Mach 1.24

7. EXPANSION OF STEAM

The droplet nucleation and growth kinetics during the expansion of steam under typical EFD operating conditions are rapid processes. These fast rates are due to the high concentration of condensates. The analytical techniques used to determine the droplet kinetics during the expansion of humidified air can be adapted to pure steam expansion with the addition of the heat balance on the droplet. However, the analysis, using the humidified air approach is extremely cumbersome when applied to steam. Therefore, an analytical approach similar to that developed by Hill[e] was used to get an estimate of the water droplet number density and average droplet size after expansion.

The one dimensional flow equations used in the analysis are:

Continuity

$$\dot{m} = \frac{\rho u A}{(1-\mu)}$$

where

$\dot{m}$ = mass flow rate

ρ = vapor phase density

u = velocity

A = flow area

$\mu = \frac{\text{mass fraction liquid}}{\text{mass fraction vapor}}$

Momentum

$$-AdP = \dot{m}du$$

where

P = pressure

Energy

$$C_p dT + udu = h_{fg} d\mu$$

where

C_p = gas phase specific heat

T = temperature

h_{fg} = heat of condensation

Once the expansion process has started and droplet nucleation and growth is in progress, the rate at which liquid phase is forming in a volume element $A(x)dx$ due to sites previously nucleated in a volume $A(x_1)dx_1$ is:

$$4\pi\rho_c \left[\left(r_o + \int_{x_1}^{x} \frac{1}{u} \frac{dr}{dt} dx' \right)^2 J(x_1)A(x_1)dx_1 \frac{dr}{dt} \frac{dx}{u} \right]$$

where

ρ_c is condensate density

J is nucleation rate per unit volume

r_o is nucleation site radius

t is time

x is flow direction coordinate

r is droplet radius

The rate of change of mass in the liquid phase to that in the vapor phase along the flow axis is:

$$\frac{d\mu}{dx} = \frac{4\pi\rho_c}{\dot{m}} \left[\int_0^x \left(r_o + \int_{x_1}^{x} \frac{1}{u} \frac{dr}{dt} dx' \right)^2 J(x_1)A(x_1) \frac{1}{u} \frac{dr}{dt} dx_1 + \frac{1}{3} r_o^3 J(x)A(x) \right]$$

Integration variables can be defined to reduce the number of terms in the condensation rate equation. Define K_1 as:

$$K_1 = 4\pi \int_0^x \left(r_o + \int_{x_1}^{x} \frac{1}{u} \frac{dr}{dt} dx' \right)^2 J(x_1)A(x_1)dx_1$$

then,

$$\frac{dK_1}{dx} = 8\pi \int_0^x \left(r_o + \int_{x_1}^{x} \frac{1}{u} \frac{dr}{dt} dx' \right) J(x_1)A(x_1) \frac{1}{u} \frac{dr}{dt} dx_1 + 4\pi r_o^2 J(x)A(x)$$

Let K_2 be:

$$K_2 = 8\pi \int_0^x \left(r_o + \int_{x_1}^{x} \frac{1}{u} \frac{dr}{dt} dx' \right) J(x_1)A(x_1)dx_1$$

then,

$$\frac{dK_1}{dx} = \left(K_2 \frac{1}{u} \frac{dr}{dt} + 4\pi r_o^2 JA \right)$$

and,

$$\frac{dK_2}{dx} = \left(8\pi \int_o^x J(x_1)A(x_1)dx_1 \frac{1}{u} \frac{dr}{dt} + 8\pi JAr_o \right)$$

As a final substitution, let K_3 be:

$$K_3 = 8\pi \int_o^x J(x_1)A(x_1)dx_1$$

then,

$$\frac{dK_2}{dx} = \left(K_3 \frac{1}{u} \frac{dr}{dt} + 8\pi r_o JA \right)$$

and,

$$\frac{dK_3}{dx} = 8\pi r_o JA$$

By differentiating the flow equation with respect to x, the condensation problem can be expressed in terms of the following equations which can be programed for solution:

$$\frac{dp}{dx} = P \left[\left(\frac{1}{(1-\mu)} - \frac{h_{fg}}{C_p T} \right) \frac{d\mu}{dx} + \frac{1}{A} \frac{dA}{dx} \right] \left[\frac{\gamma\mu^2}{(1-\mu)\left[1+(\gamma-1)M^2\right] - \gamma M^2} \right]$$

$$\frac{dT}{dx} = T \left[\frac{h_{fg}}{C_p T} \frac{d\mu}{dx} + \frac{(\gamma-1)(1-\mu)}{\gamma P} \frac{dP}{dx} \right]$$

$$\frac{dM}{dx} = \frac{-1}{M} \left[\frac{(1-\mu)}{\gamma P} \frac{dP}{dx} + \frac{M^2}{2\gamma RT} \frac{dT}{dx} \right]$$

$$\frac{dM}{dx} = \frac{\rho_c}{\dot{m}} \left(K_1 \frac{1}{u} \frac{dr}{dt} + \frac{4\pi}{3} JAr_o^3 \right)$$

$$\frac{dK_1}{dx} = \left(K_2 \frac{1}{u} \frac{dr}{dt} + 4\pi JAr_o^2 \right)$$

$$\frac{dK_2}{dx} = \left(K_3 \frac{1}{u} \frac{dr}{dt} + 8\pi JAr_o \right)$$

$$\frac{dK_3}{dx} = 8\pi JA$$

where

R is condensate gas constant

C_p is specific heat ratio

M is Mach number

The condensate was assumed to behave as an ideal gas in deriving the equation set.

The growth rate of a droplet, $\frac{dr}{dt}$, can be expressed as:

$$\frac{dr}{dt} = \frac{m_c}{\rho_c} (I_i - I_e)$$

where

M_c is condensate molecular mass

I_i is impingement rate of condensate molecular per unit droplet area

I_e is evaporation rate per unit area of a droplet.

The term I_i is a function of the gas steam temperature and pressure and I_e of the droplet temperature and size.

If the droplet radius of curvature is neglected and defining, α,

$$\alpha = 1 - \frac{T}{T_D}$$

where T_D is the droplet temperature.

The droplet growth rate can be expressed as:

$$\frac{dr}{dt} \approx \frac{m_c I_c}{\rho_c} \left[1 - \frac{p'}{p} \exp \frac{h_{fg}\alpha}{RT} \right]$$

where

P' is condensate saturation pressure at the steam temperature, T.

The term, α, which defines the droplet temperature is determined from the heat balance on a droplet. The droplets will be at higher temperature than the gas stream. Thus, the vapor leaving the droplets will remove more sensible heat than that arriving. This vapor sensible heat difference along with any sensible heat accumulated in a droplet due to a liquid phase temperature change will accommodate the thermal energy associated with the net condensation of liquid on to the droplet. The heat balance can be expressed as:

$$I_i h_{fg} - I_e \left[h_{fg} + C_p \left(T_D - T \right) \right] = \frac{\rho_c r C_{pL}}{\dot{m}_c} \frac{dT_D}{dt} + \left(I_i - I_e \right) C_{pL} \left(T_D - T \right)$$

where

C_{pL} is liquid phase specific heat.

The sensible heat due to temperature change within the droplet will be small relative to the vapor phase heat flux and heat of condensation; therefore, this term can be neglected. By rearranging terms and substituting α for T_D, the heat balance equation can be expressed as:

$$1 - \frac{C_{pL} T \alpha}{h_{fg}} = \frac{P'}{P} \left\{ 1 + \left[\frac{\gamma RT}{(\gamma - 1) h_{fg}} - \frac{C_{pL} T}{h_{fg}} \right] \alpha \right\} \exp \left(\frac{h_{fg}}{RT} \right)$$

The assumption used in the derivation of the condensation problem which will cause the largest error is that of neglecting the effect of droplet curvature on vapor pressure. The result of this assumption will be to under-estimate the droplet number density and over-estimate their size. The droplets are grouped into a single mean area size in the analysis which is made possible by the assumption.

The equations were solved for two flow cases. These were, constant pressure and constant area. The results with various initial conditions are shown in Table III. The expansion was assumed to be instantaneous to the starting Mach number. The results indicated that there is an excessive number of droplets formed and they are small in size. The droplet sizes were adequate to exhibit low mobility for conditions of low initial relative humidity. However, the gas density is reduced under the low relative humidity conditions which will reduce its breakdown strength. The analysis also indicates that the droplets grow to a maximum size and then diminish as flow progresses along the channel. The maximum size is included in the table. This behavior occurred for both constant area and pressure flow. The cause of this behavior results from neglecting droplet curvature effect on vapor pressure. By neglecting curvature effects, all size droplets have an equal probability of growing. Therefore, newly nucleated droplets can grow at the expense of existing drops.

Table III. Steam Expansion Analysis Summary

Equivalent Channel Size	Stagnation Conditions: Press. (psia)	Temp. °F	Temp. °K	R.H. (%)	Expanded Conditions: M_o	P_o (psia)	T_o (°K)	Conditions at Maximum Droplet Size or Number Density: P/P_o	T/T_o	M/M_o	A/A_o	Fraction Condensed	Number Density (Droplets/M^3)	Radius (Meter)	Distance From Initial Expansion (M)
1/12	338.1	450	505.6	80	1.24	138.7	416.0	1	1.039	.987	1.023	.0162	8.76×10^{20}	2.84×10^{-9}	7×10^{-5}
								1	1.087	.973	1.048	.0359	6.26×10^{21}	1.90×10^{-9}	1.7×10^{-4}
1/12	338.1	450	505.6	60	1.24	138.7	416.0	1.062	1.042	.969	1	.0117	7.80×10^{20}	2.70×10^{-9}	6×10^{-5}
								1.161	1.103	.923	1	.0286	5.64×10^{21}	1.90×10^{-9}	1.2×10^{-4}
1/12	317.0	450	505.6	75	1.24	130.0	416.0	1	1.037	.988	1.021	.0154	8.79×10^{20}	2.73×10^{-9}	8×10^{-5}
								1	1.079	.975	1.044	.0324	3.89×10^{21}	2.11×10^{-9}	1.6×10^{-4}
1/12	317.0	450	505.6	75	1.24	130.0	416.0	1.062	1.042	.969	1	.0116	8.13×10^{20}	2.61×10^{-9}	7×10^{-5}
								1.146	1.094	.930	1	.0260	4.40×10^{21}	1.96×10^{-9}	1.3×10^{-4}
1/12	408.3	450	505.6	96.6	2.00	53.5	324.1	1	1.046	.998	1.032	.0154	1.46×10^{18}	1.86×10^{-8}	2×10^{-3}
								1	1.267	.970	1.159	.0855	2.20×10^{20}	5.81×10^{-9}	9.2×10^{-4}
1/12	408.3	450	505.6	96.6	2.00	53.5	324.1	1.044	1.048	.992	1	.0124	1.40×10^{18}	1.78×10^{-8}	8.6×10^{-4}
								1.253	1.302	.956	1	.0796	7.63×10^{20}	4.00×10^{-9}	1.95×10^{-3}
1/12	1000	572.4	573.6	80	2.00	131.0	367.7	1	1.053	.994	1.033	.0193	4.34×10^{19}	6.36×10^{-9}	3.2×10^{-4}
								1	1.221	.975	1.123	.0803	2.97×10^{21}	3.13×10^{-9}	1.3×10^{-4}
1/12	1000	572.4	573.6	80	2.00	131.0	367.7	1.046	1.053	.991	1	.0156	4.06×10^{19}	8.08×10^{-9}	1.2×10^{-4}
								1.191	1.241	.966	1	.0729	3.39×10^{21}	3.06×10^{-9}	2.6×10^{-4}
1/12	750	572.4	573.6	60	2.00	131.0	367.7	1	1.052	.994	1.032	.0191	3.82×10^{19}	7.89×10^{-9}	2×10^{-4}
								1	1.189	.978	1.107	.0684	1.67×10^{21}	1.53×10^{-9}	5×10^{-4}
1/12	750	572.4	573.6	60	2.00	131.0	367.7	1.042	1.048	.992	1	.0142	3.37×10^{19}	7.58×10^{-9}	1.8×10^{-4}
								1.166	1.205	.971	1	.0618	2.07×10^{21}	3.10×10^{-9}	4.2×10^{-4}
1/24	1000	572.4	573.6	80	2.00	131.0	367.7	1	1.050	.994	1.031	.0182	6.23×10^{19}	7.26×10^{-9}	1.9×10^{-4}
								1	1.220	.975	1.123	.0802	5.82×10^{21}	2.50×10^{-9}	5.2×10^{-4}
1/24	1000	572.4	573.6	80	2.00	131.0	367.7	1.046	1.053	.991	1	.0157	6.19×10^{19}	7.04×10^{-9}	1.8×10^{-4}
								1.191	1.241	.966	1	.0729	7.79×10^{21}	2.31×10^{-9}	4.3×10^{-4}
1/24	750	572.4	573.6	60	2.00	98.2	367.7	1	1.050	.994	1.031	.0181	5.43×10^{19}	6.90×10^{-9}	2.9×10^{-4}
								1	1.188	.979	1.107	.0684	3.07×10^{21}	2.69×10^{-9}	8×10^{-4}
1/24	750	572.4	573.6	60	2.00	98.2	367.7	1.043	1.050	.992	1	.0148	5.17×10^{19}	6.65×10^{-9}	2.7×10^{-4}
								1.165	1.205	.971	1	.0617	4.13×10^{21}	2.46×10^{-9}	6.8×10^{-4}
1/4	219.4	409	482.8	80	1.24	90.0	397.3	1	1.035	.989	1.021	.0140	3.07×10^{20}	3.38×10^{-9}	1.8×10^{-4}
								1	1.077	.976	1.044	.0302	1.95×10^{21}	2.33×10^{-9}	4.3×10^{-4}
1/4	219.4	409	482.8	80	1.24	90.0	397.3	1.061	1.040	.970	1	.0105	2.92×10^{20}	3.16×10^{-9}	1.6×10^{-4}
								1.146	1.090	.930	1	.0235	2.10×10^{21}	2.18×10^{-9}	3.3×10^{-4}
1/4	219.4	409	482.8	80	2.00	28.7	309.5	1	1.047	.994	1.032	.0143	3.07×10^{17}	2.52×10^{-8}	2.8×10^{-3}
								1	1.252	.972	1.156	.0772	1.74×10^{20}	5.03×10^{-9}	9.2×10^{-3}
1/4	219.4	409	482.8	80	2.00	28.7	309.5	1.043	1.047	.992	1	.0114	2.91×10^{17}	2.41×10^{-8}	2.6×10^{-3}
								1.239	1.275	.959	1	.0685	2.70×10^{20}	4.46×10^{-9}	7.3×10^{-3}

8. CONCLUSIONS

Analyses have been developed to predict drop sizes and number densities. The computer has been used to perform the calculations for a wide range of water temperatures in air, as used for the 1/4-inch modelling geometry and for the 1/12-inch through 1/48-inch conversion geometries. An experimental confirmation of these computer predictions nas been obtained by measuring the intensity of laser light scattered off the nucleated and grown water drops in the supersonic flow of the 1/4-inch modelling EFD channel. This channel was also used to obtain Mach number profiles across the flow at different axial locations. These results readily explain the details of the charged droplet formation in the EFD generator.

In all the geometries investigated in this study, using air with water vapor at 80% humidity, a more than adequate number of droplets are self nucleated and grown before the corona tip is reached, and negative ions from the corona then diffuse through and attach to the droplets.

The experimental investigation of hydrodynamic spraying indicates the charged droplets have excess numbers of charges and consequently would have too much slip within the EFD fluid flow.

The analysis of the neucleation and growth of water droplets in the expansion of pure steam indicate that too many small droplets would be produced for the temperature and pressures that are appropriate for the generators studied.

SECTION IV

GAS BREAKDOWN EXPERIMENTS

An experimental program was undertaken to determine the effects of gas flow, corona current, electrode material and additives on high voltage breakdown in different high pressure gases.

1. EXPERIMENTAL APPARATUS

The pressure chamber used for the study is shown in Figure 33 a and b. A schematic of the inside of the chamber is shown in Figure 34. There are windows to observe the breakdown and a mechanism to adjust the gap setting from the outside. Most of the high pressure seals are such that the pieces are wedged together. Additional seals and constraints are provided to allow chamber evacuation. A high voltage, polyethlene cable fits into the connector at the top and leads to the voltage source. During the qualitative phase of the study, a current limited, 120 kV, oil-filled supply was used; but most of the study used a Van de Graaff generator capable of delivering over 200 kV whose voltage was measured by a rotating generating electrostatic voltmeter.

2. GENERAL QUALITATIVE OBSERVATIONS

Gas flow has no observable effect except as it alters the density of the gas between electrodes. This is understandable since the avalanche-streamer formation is in a very short period compared to the time for gas passage between electrodes, even at supersonic speeds.

High voltage breakdown is very fast, consistent with streamer formation, and always between a small spot on the anode and a small spot on the cathode. Almost identical molten craters are made on each electrode regardless of material, even when the discharged capacity is only 10's of picofarads. This has been confirmed with stainless steel, copper, gold, and tungsten electrodes. Luckily, with most gases, the craters do not degrade the breakdown strength - rarely does a crater intersect a former one.

Experiments preceded by sputtering the electrodes in argon showed that insulating films play no role in anomalous high pressure breakdown. Also, charged particles and radiation from corona do not effect breakdown.

After these qualitative questions were answered, the electrodes were changed to stainless steel segments of hemispheres of large radius to simulate near uniform electric fields - largest in the center and essentially equal to the voltage divided by the separation. All later data were taken with this geometry.

3. DATA - BREAKDOWN STRENGTH OF VARIOUS HIGH PRESSURE GASES

For the following data where a constant P-d product is given, the data were taken by varying the pressure and at each pressure adjusting the separation of the electrodes so the distance, d, in inches times the pressure in psia is the desired product. For example, at 1000 psia for a P-d product at 25 psi-in, the gap is 0.025 inch which is one turn from electrodes touching (adjusting threads are 40 per inch.)

PRECEDING PAGE BLANK-NOT FILMED

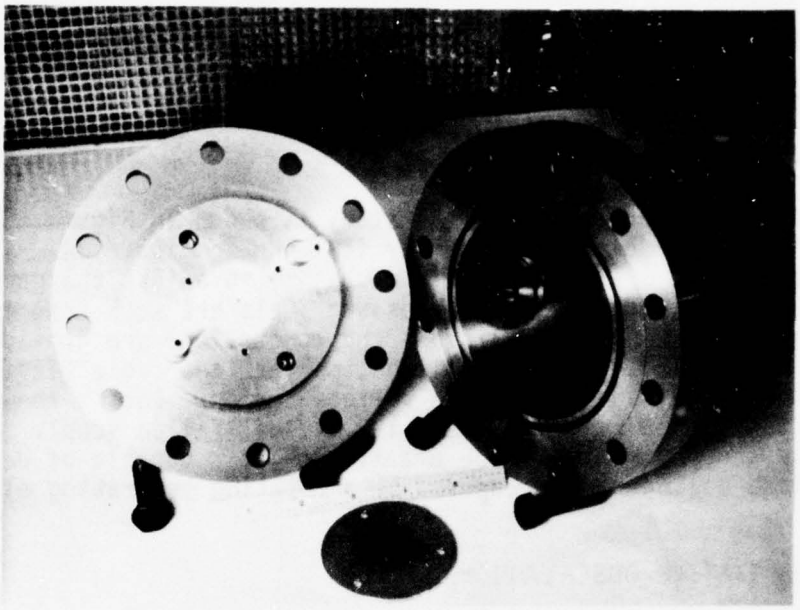

a) Partially Assembled

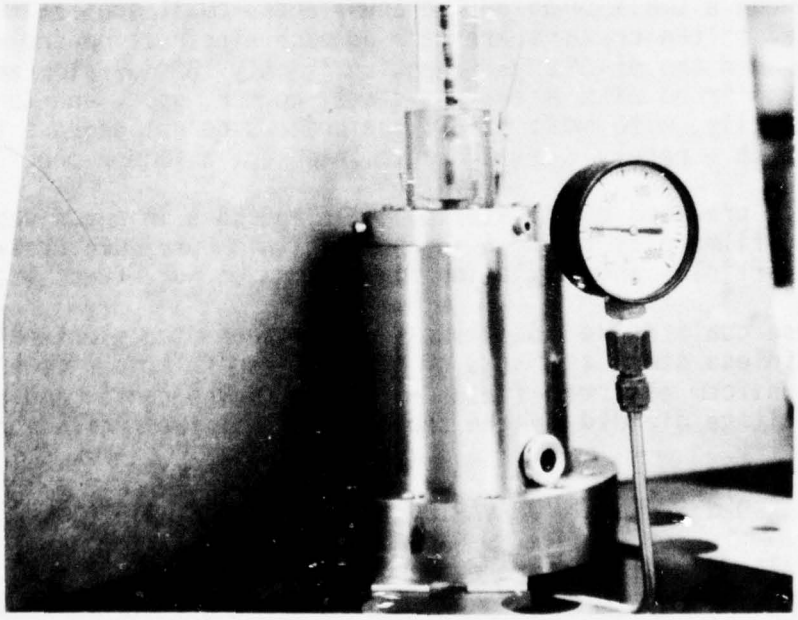

Figure 33. b) Fully Assembled Gas Breakdown Cell

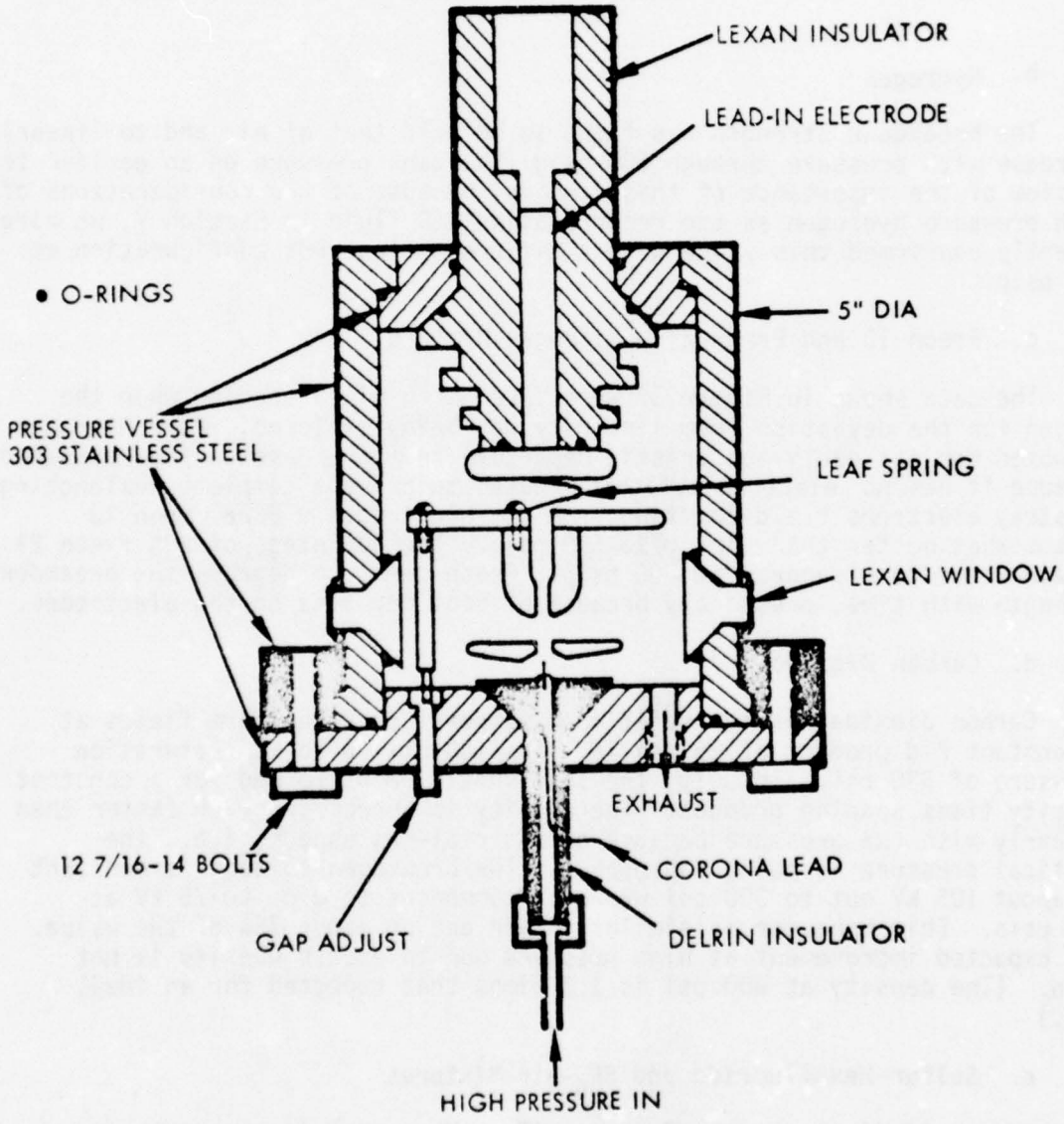

Figure 34. Gas Breakdown Cell Design

a. Air with No Additive

Figure 35 shows the breakdown voltage versus pressure for a constant P-d product. Classical breakdown laws (such as the Paschen law) would predict a constant voltage. Instead, at a somewhat variable pressure between 300 and 500 psi (probably dependent on the surface smoothness), a linear decrease in voltage starts. In Figure 36, the electrodes have been repolished and cleaned, and the onset of the deviation is now about 500 psi. At a later time, this data was extended to 1500 psi (>100 atm). The breakdown voltage continued its linear decrease and had a value of 65 kV at 1500 psi.

b. Hydrogen

The breakdown strength was found to be half that of air and to linearly increase with pressure through 600 psig (the tank pressure on an earlier test). In view of the importance of this finding, because of the considerations of high pressure hydrogen as the recirculating EFD fluid in Section V, we more recently confirmed this value with a different electrode configuration at 800 psig.

c. Freon 13 and Freon 21 - Nitrogen Mixture

The data shown in Figure 37 were taken with fixed spacing when the reason for the deviation from linearity was being explored. Pure nitrogen is noted for its early and drastic departure from the Paschen law, presumably because it has no electron-attaching gases to prevent complete avalanching of stray electrons field emitting from its electrodes. Pure freon 13 is somewhat better than air up to 500 psig. The advantage of 20% freon 21 in air seems to disappear at 800 psig. Freon seems to degrade the breakdown strength with time, presumably because of soot deposits on the electrodes.

d. Carbon Dioxide

Carbon dioxide was tested at room temperature in uniform fields at a constant P-d product of 25 psi-in from 100 psi up to its saturation pressure of 830 psi. Ideally, the test should be performed for a constant density times spacing product. The density is increasing much faster than linearly with the pressure because of the real-gas aspect, i.e., the critical pressure is being approached. The breakdown voltage is constant at about 105 kV out to 300 psi where it commences to drop to 75 kV at 800 psia. This behavior is similar to air but at about 78% of the value. The expected improvement at high pressure due to excess density is not seen. (The density at 800 psi is 1.7 times that expected for an ideal gas.)

e. Sulfur-Hexafluoride and SF_6-Air Mixtures

Figure 38 displays data for pure SF_6. Note that its strength is four times greater than air but the deviation occurs at a smaller electric field strength than for air. A single data point for 50% air is shown for comparison. The 50% SF_6 - 50% air is nearly as good as 100% SF_6.

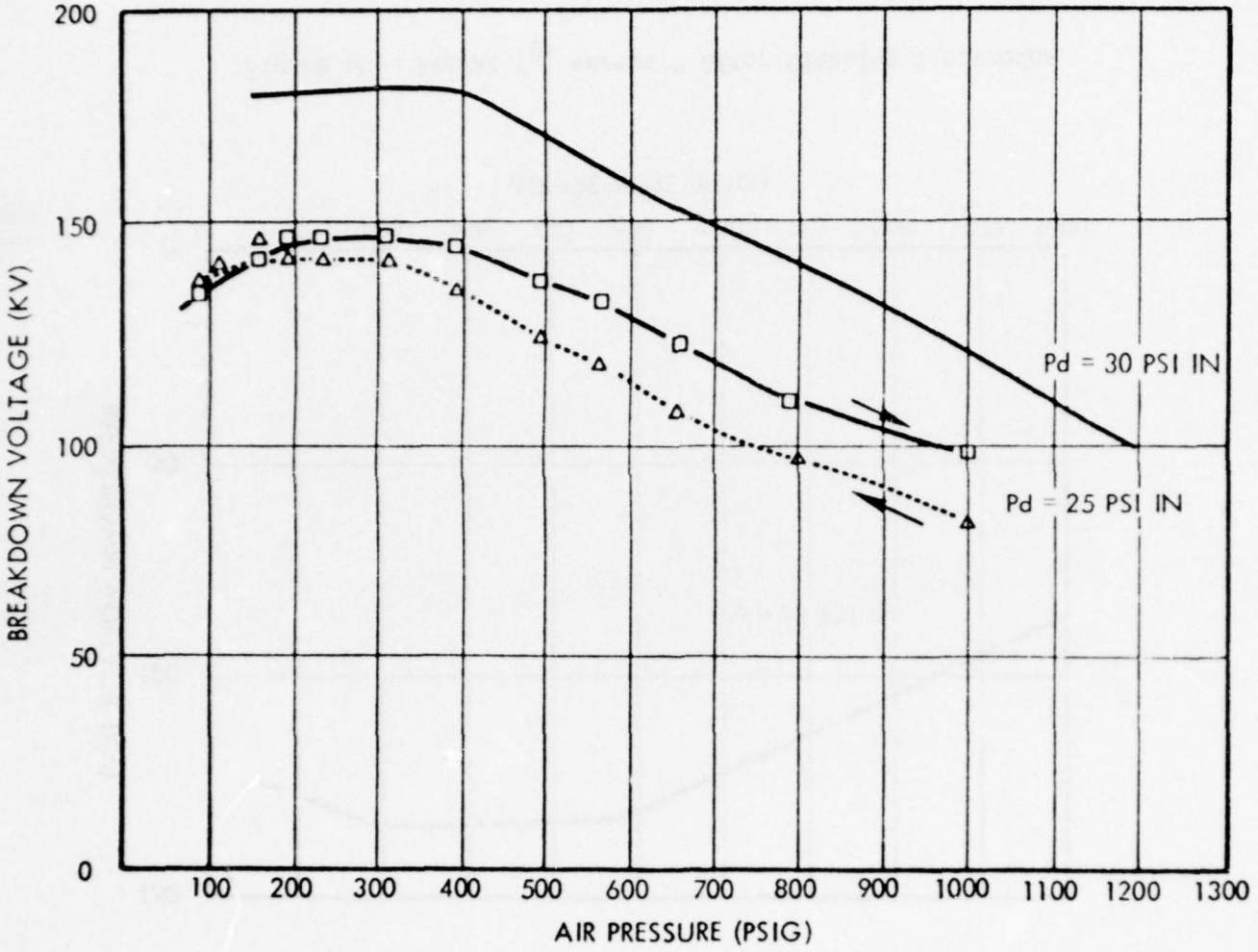

Figure 35. Breakdown Voltage in Air versus Pressure for Two Pd Products

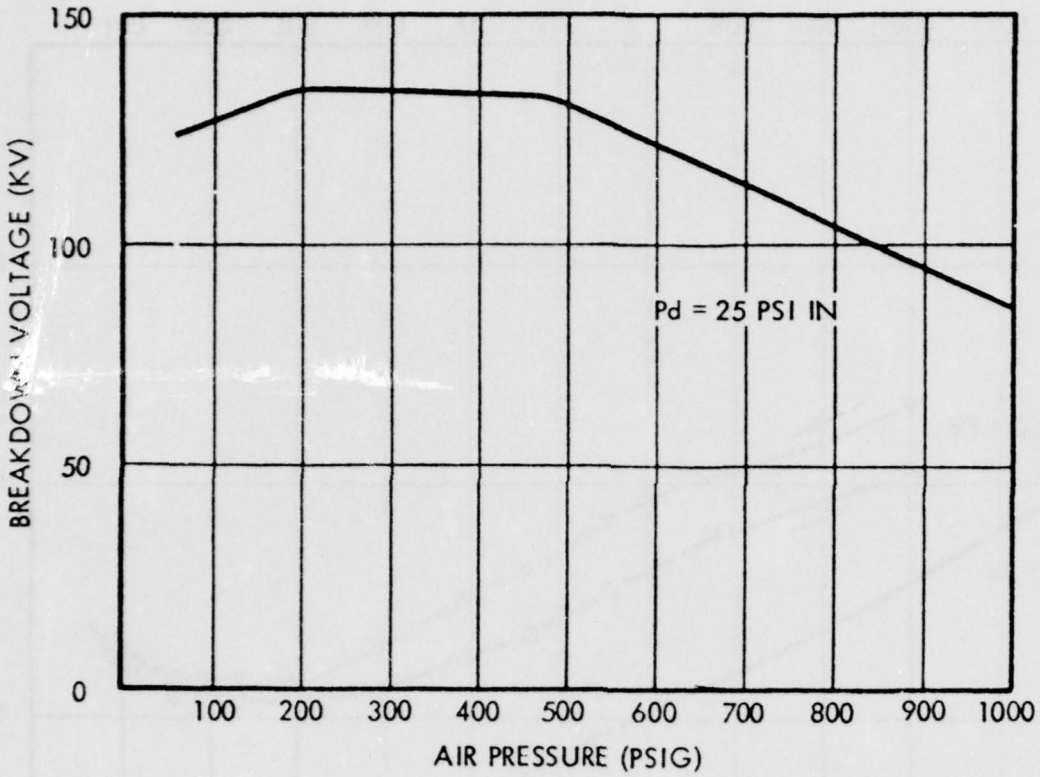

Figure 36. Repeat V_{Br} versus P After Cleaning Electrodes

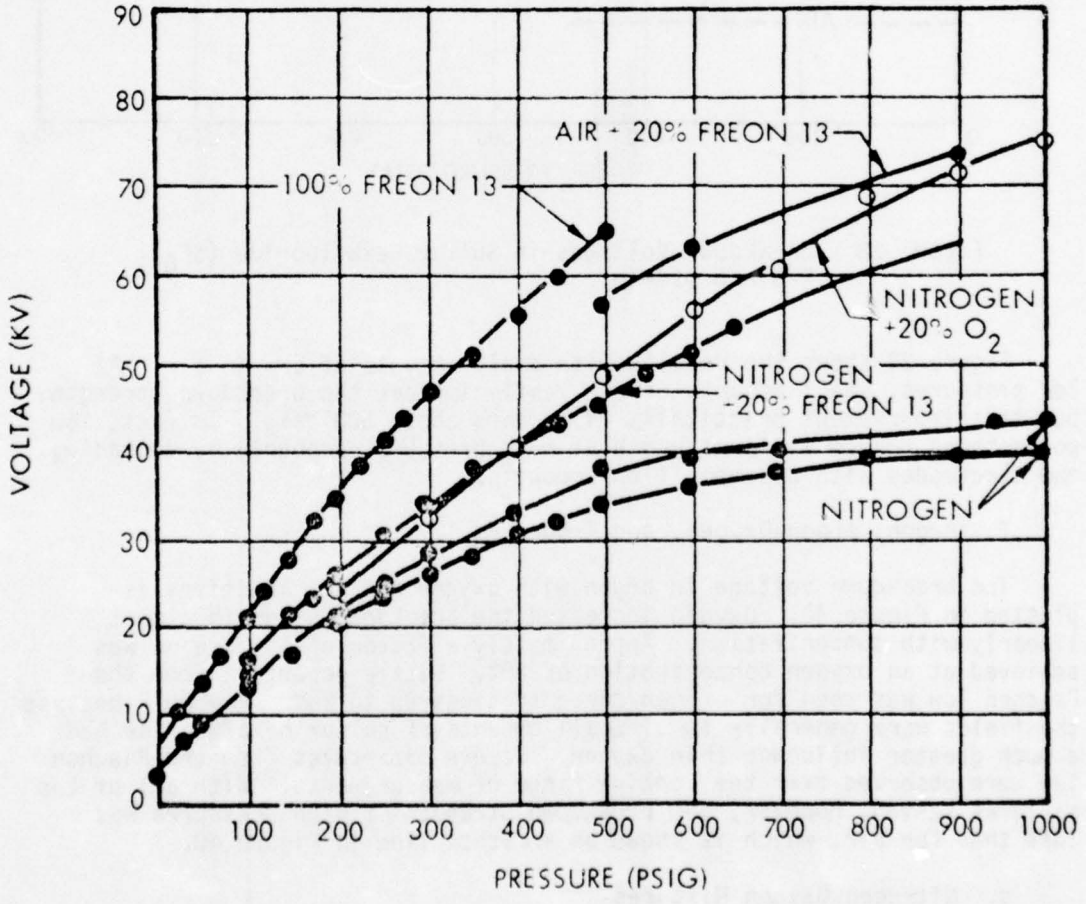

Figure 37. Breakdown Characteristics of Nitrogen, Doped Nitrogen and Freon 13 for a Spacing of ~ 0.020"

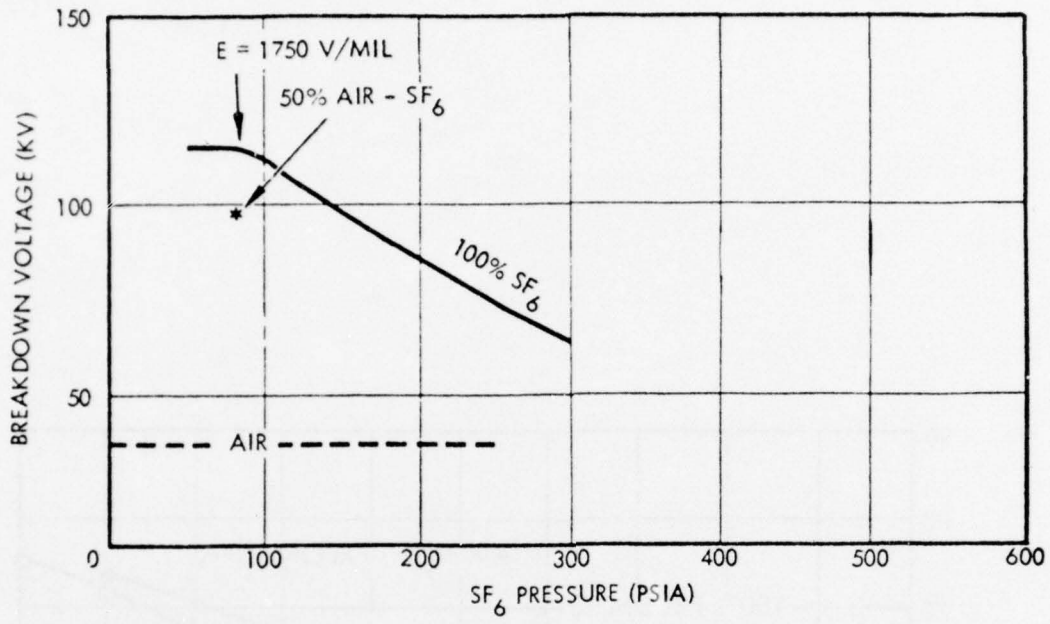

Figure 38. Breakdown Voltages in Sulfur Hexafluoride (SF_6). P-d = 6 psi-in.

Figure 39 shows the results with small amounts of SF_6 in air. At low pressures, small amounts of SF_6 vastly improve the breakdown strength, but this improvement practically disappears about 500 psig. In fact, low percentages reduce air's strength at high pressure, probably by degrading the electrodes with decomposition products.

f. Argon, Argon-Oxygen, and Argon-SF_6

The breakdown voltage in argon with oxygen and SF_6 additives is plotted in Figure 40. Oxygen increased the breakdown strength almost linearly with concentration. Approximately a factor of 4 increase was achieved at an oxygen concentration of 20%. Little departure from the Paschen law was seen for oxygen concentrations up to 20%. Probably because the fields were generally low. Small amounts of sulfur hexafluoride had a much greater influence than oxygen. Severe departures from the Paschen law were observed over the entire range of measurements. With all of the mixtures tested, however, the breakdown strength at high pressures was less than for air, which is shown as a dashed line in Figure 40.

g. Nitrogen-Oxygen Mixtures

Figure 41 illustrates the influence of oxygen in increasing the high pressure breakdown strength of nitrogen. Small amounts of oxygen (5% by volume) increased the 1000 psi breakdown strength by about a factor of 2.

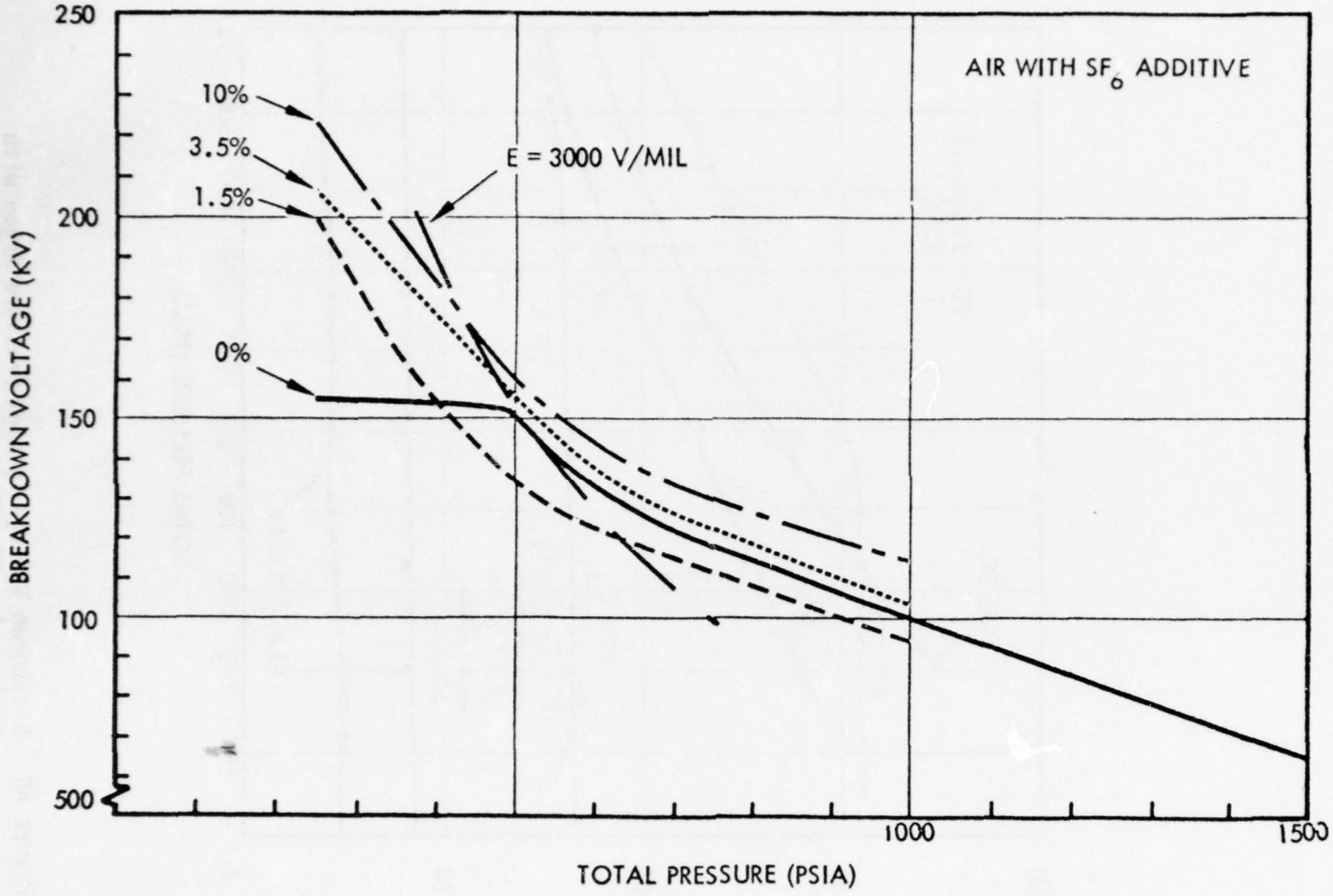

Figure 39. Breakdown Voltages in High Pressure Air with Small Percentages of SF_6. Pd = 25 psi-in.

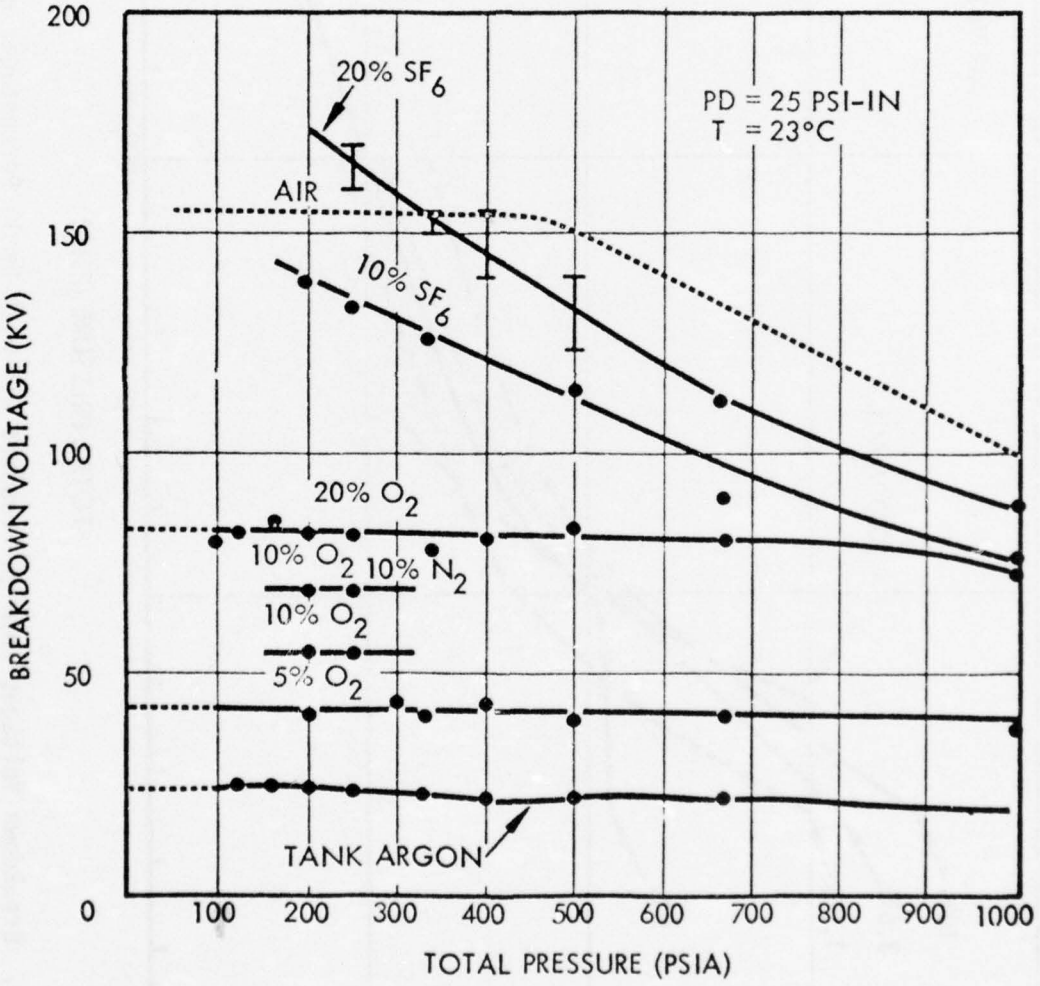

Figure 40. Breakdown Voltage in High Pressure Argon with Various O_2, SF_6 Mixtures

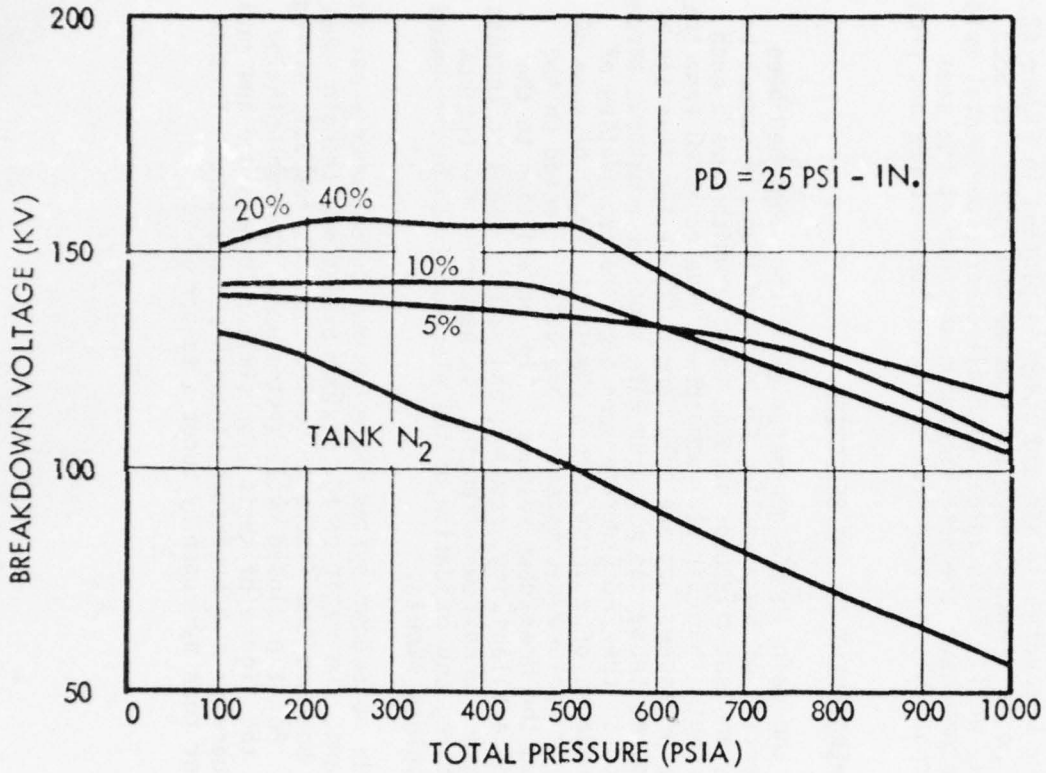

Figure 41. Breakdown Voltage of High Pressure N_2-O_2 Mixtures

Increasing the oxygen concentration to 20% increased the breakdown strength somewhat, but practically no difference was seen in going from 20% to 40% oxygen mixtures.

h. Steam

The breakdown strength of steam at 475^{o}F was compared with air for a 0.5 and 1.0 mm uniform field gap. Both electrodes of this gap were stainless steel. The breakdown in air and steam is plotted in Figure 42. The best straight line is drawn through the scatter and represents both steam and air equally well. This agrees with all other experimental evidence - i.e., that air and steam have the same breakdown strength at the same pressure. We show that this is also true at higher temperatures and pressures through 170 psig.

4. EFD GENERATOR IMPROVEMENT BY GAS SELECTION

Unfortunately, the gain in EGD generator efficiency that had been expected by the selection of some working fluid other than air cannot be achieved. All gases and gas mixtures studied to date which have a much larger breakdown strength than air at 1 atmosphere have departed from the Paschen law at lower pressures but are only marginally better than air at high pressures. Furthermore, those gas mixtures with superior breakdown strengths that have been tested in the EFD generator have caused degradation of performance either because of adverse corona characteristics, because of chemical corrosion, or because decomposition products collected on the electrode and lowered the breakdown voltage. Air, in addition to the obvious advantages of availability, economy, and safety, seems to possess quite good high pressure breakdown strength. It has about the optimum nitrogen-oxygen mixture, and oxidation of the electrodes can be prevented by using common stainless steels.

In an open cycle blowdown system where maximum output energy per stored mass becomes important, the ratio of the maximum breakdown strength squared to the gas density, becomes the figure of merit. In this respect, hydrogen is better than air. For the closed cycle system where maximum enthalpy removal is desired, the figure of merit (for similar temperature and ratios of C_p/cv) is the square of the breakdown strength per pressure. In this respect air is better than hydrogen by about a factor of 2.

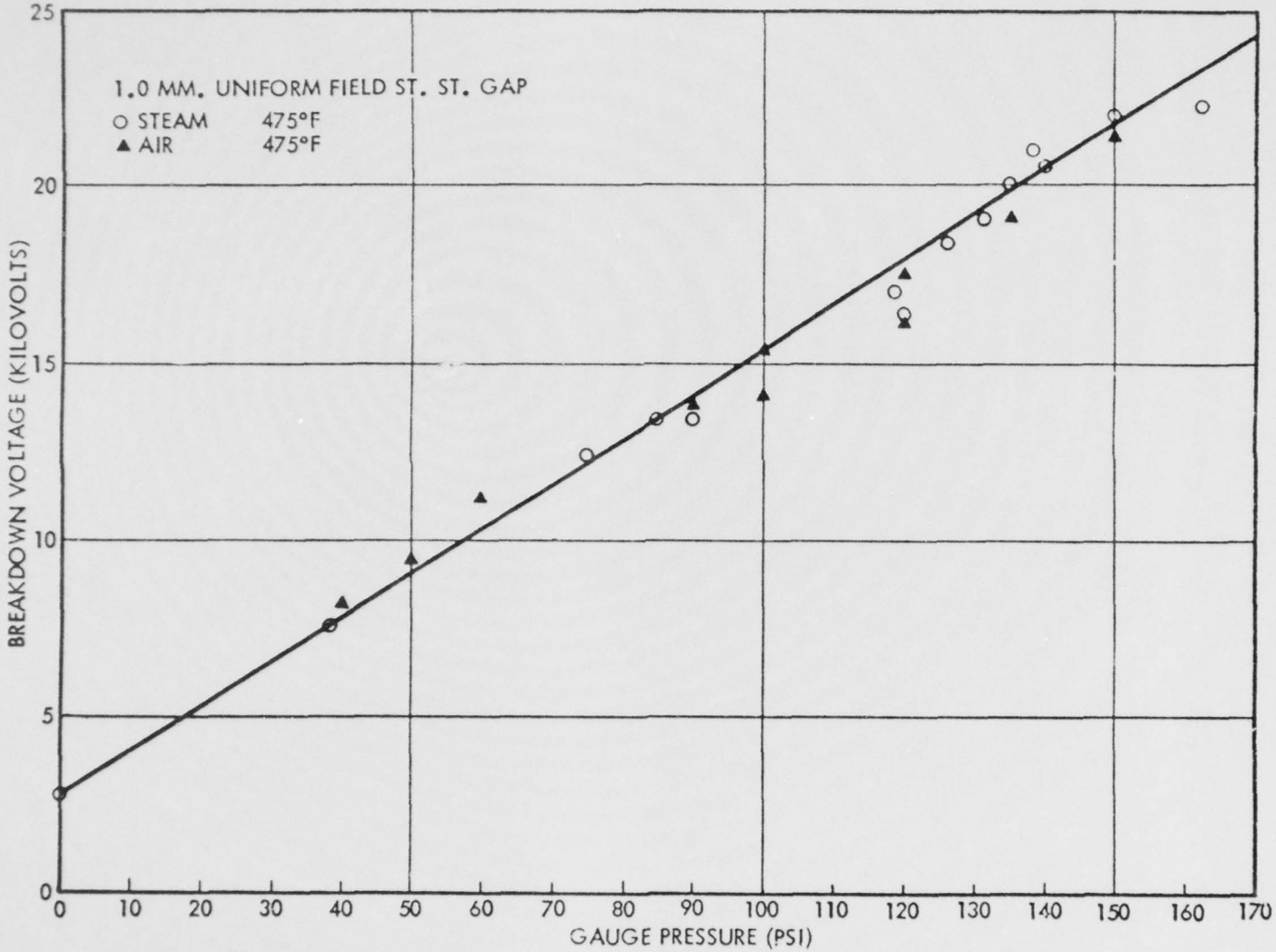

Figure 42. Breakdown Voltage of Steam and Air Versus Pressure

SECTION V

EFD GENERATING SYSTEMS

The single fluid EFD generator, even with its efficiency limitation, has two features that recommend consideration of its use in high power airborne systems: (1) the generator itself is light and compact and needs no cooling; and (2) the generator can have a short response time because of its few moving parts. A theoretical analysis, presented in the last part of this section, establishes the efficiencies of single gas systems and two-fluid systems. For single gas systems, hydrogen has the highest energy removal per stored mass and is chosen for the design of airborne EFD generating systems. For a closed recirculating system, the mercury-hydrogen system shows the highest efficiency and is chosen for the design of a ground-based system.

1. AIRBORNE HIGH POWER AND HIGH ENERGY EFD SYSTEMS

This section considers the design of an airborne EFD power package that can supply 6 MW intermittently or continuously for 1 minute. First it is shown that it is not feasible to store the working fluid as a cryogenic liquid at ambient pressure with a pump being used to transfer the liquid to high pressure; this approach requires too much power. Next the weight of the cryogenic working fluid and its Kevlon fiber-reinforced plastic pressure container is calculated for both air and hydrogen working fluids. The systems considerations are presented for the lighter weight H_2 systems only, although they also are applicable to air. The method of rapidly adding heat to vaporize and heat the gas and at the same time humidify it is discussed. Then the type of cylindrical stacked EFD generator that would be used and the estimates of its weight and size are given.

a. Pump Power

The pump power required to deliver the EFD fluid at the high working pressure required for this type of generator is prohibitive, when the fluid is stored as a liquid at ambient pressure. This power requirement can exceed the output electric power. For this reason low pressure storage is not a viable alternative to the high pressure storage tank approach.

This important, fundamental point can be expressed in simple terms. The pump work required to deliver a unit mass of liquid at the pressure P (neglecting the initial, low, storage pressure) is P times the volume of a unit mass, or P/ρ_ℓ where ρ_ℓ is the liquid density. The next step in operating the generator is to heat the liquid at constant pressure to convert it to a gas and raise its temperature to the required working level. After this has been done, the enthalpy of a unit mass of gas is C_pT, where C_p is specific heat at constant pressure. By using the equation of state for a perfect gas,

$$C_pT = \frac{C_p}{R}\frac{P}{\rho_g} = \frac{\gamma}{\gamma-1}\frac{P}{\rho_g}$$

where ρ_g is the gas density. Therefore, the ratio of the pump work per unit

PRECEDING PAGE BLANK-NOT FILMED

mass to the stagnation enthalpy of the heated gas per unit mass is

$$\frac{\text{Pump Work}}{\text{Gas Enthalpy}} = \frac{\gamma - 1}{\gamma} \frac{\rho_g}{\rho_\ell}$$

As an example, nitrogen gas has a density of 0.14 g/cc at 400°K and 2400 psia while liquid nitrogen has a density of 0.81 g/cc. Thus, using $\gamma = 1.4$, the ratio of the pump work to gas enthalpy is 0.05, or about the same as the electrical conversion efficiency of a blow-down EFD generator. Another example is hydrogen stored at 5000 psia and 400°K. The gas density for this case is 0.02 g/cc and the liquid density is 0.07 g/cc. Again using $\gamma = 1.4$, the pump work is 8% of the stagnation enthalpy of the gas.

This result may seem surprising when it is compared to chemical rocket engines and MHD generators where pump work is trivial compared to the delivered energy. There is a fundamental reason for this difference. It is that the physical properties of the colloidal particles require that the storage temperature of the working fluid be kept low compared to the temperatures that can be used in the other devices.

b. Choice of Operating Parameters

Both M. Lawson of the Air Force, using an incompressible formulation of the EFD generator flow, and L. Dailey of TRW Systems, using one-dimension compressible flow equations with empirical loss coefficients (presented later in this section) have concluded that, an EFD generator, with a primary Mach number of 2, can extract around 7% of the stagnation enthalpy for air and 4% for hydrogen. The value calculated for air requires only a small extrapolation from experimental data achieved by the in-house Air Force program. The value calculated for hydrogen is based on measured data for the breakdown strength of hydrogen together with its known linear increase to high pressures.

These two numbers, 7% enthalpy removal for air and 4% for hydrogen, were chosen for the basis of our analysis. The primary stagnation pressure was chosen as 2500 psia for air and 5000 psia for hydrogen to provide Mach 2 at the desired generator pressure. A temperature of 480°K was selected to provide about 90% relative humidity with the combustion products. The recirculating secondary flow is cooled to about 400°K by introduction of additional water to provide the necessary secondary humidity. The output pressures are about 300 psia for air and 600 psia for hydrogen. The geometries of the two systems are similar and are chosen to generate 200 kV. For simplicity, only a single stage is considered.

c. Weight of Fluid

An airborne mission was selected requiring 6 MW of power intermittently or continuously for 1 minute. This requires a total energy of 3.6×10^8 joules. To put this large energy requirement in perspective, the weights required for some common energy sources are considered. High rate batteries with a power density of 16 watt-hours/lb. would weigh 6250 pounds; a high-strength steel fly wheel with an energy density of 25 w-hr/lb would weigh in excess of

4000 pounds; and gasoline at 21000 Btu/lb would weigh 16 pounds.

For the EFD generator, the energy is taken from the stagnation enthalpy of the gas. The mass required is

$$\text{Mass} = \frac{3.6 \times 10^8}{C_p T_s \eta}$$

Where C_p is specific heat at constant pressure and T_s is the stagnation temperature which has been selected as 480°K. Thus, for air with $\eta = 0.07$ and hydrogen with $\eta = 0.04$, the required masses are 25,000 pounds and 2840 pounds, respectively. The lighter hydrogen system was used for the design study. It is pointed out, however, that the air system would be about the same size, more nearly state-of-the art, safer, and would have only about a 5% penalty for the weight of the pressure vessel.

d. Pressure Vessel

The most crucial component of the EFD hydrogen airborne power system is the pressure vessel. Conventional tankage is far too heavy; therefore, a design was selected which uses super-strong, light weight plastic tankage that can be fabricated with present day technology and equipment. Many cylindrical tanks of a conventional length and about 18 inches in diameter are fabricated from "Kevlar"(f) fibers imbedded in a suitable epoxy using a diameter selected to allow winding on conventional lathes. The cylindrical plastic sections are sealed to domes at the two ends made of titanium-aluminum alloys. The metal piping is connected to these domes.

To estimate the weight of the tankage, the design is based on the known parameters of fiber glass for the cylindrical sections and allows the extra weight for the domes and epoxy within the interstices to be covered by the 40% weight reduction afforded by Kevlar.

Fiber glass, which has ultimate tensile strength in excess of 625,000 psi at low temperatures and 425,000 psi at room temperature is used at a working stress of 250,000 psi to contain the gas at 5000 psia. The volume of the fibers carrying the hoop stress is then $\frac{2\pi R^2 L}{50}$. In addition, axial fibers are used having a volume one half that of the hoop fibers. The total fiber volume is then $\frac{3\pi}{50} R^2 L$.

The weight of the fibers = $\rho_f \times \frac{3\pi}{50} \times R^2 L$ and the weight of the liquid hydrogen = $\rho_\ell \times \pi R^2 L$, so that the ratio of the two is $\frac{W_f}{W_L} = \frac{3}{50} \frac{\rho_f}{\rho_\ell}$. Using a glass density of 2.6 and a liquid hydrogen density of 0.07, the fiber weight in the tank is 2.23 times the liquid hydrogen weight, or about 6330 pounds.

The volumes of the liquid hydrogen and tanks are 650 ft^3 and 39 ft^3 respectively. Twenty-foot long, 18 inch diameter tanks would be required.

The seal between the tank ends and the domes requires special attention. The high internal pressures must be used to seal and lock a demountable joint. Also the rigid domes in conjunction with the more elastic plastic sections must not generate large twisting moments in the plastic section. This critical joint is shown in Figure 43. The axial fibers are wrapped around a continuous bundle of fibers forming a bead which is a graded thickness termination that ends in a lip at each end of the plastic cylinders. The domes are then bolted onto the cylinder using a suitable sealant and cushioning material such as Teflon as shown in Figure 43.

The high elasticity of the vessel poses special, although straight-forward problems for the liner, the mounting and the insulator jacket. The insulation would probably be jackets of foam plastic suitably mounted to allow for expansion and prevent penetration of frozen moisture from the air.

e. Heat Addition and Gas Control

Figure 44 illustrates the operation of the system. In the standby condition the fast-acting gas valve is closed. The rig is heated to 400°K, and most of the piping to 480°K. A pilot light of oxygen from a liquid cryogenic tank at 5400 psia is burning in a hydrogen gaseous pressure. This excess pressure is great enough to overcome the liquid hydrogen head and prevent liquid flow. When power is required the gas valve is opened and the main liquid oxygen line is opened, creating a large flame into which liquid hydrogen is sprayed from an array of nozzles. The oxygen flow is regulated to provide the heat required to vaporize all of the hydrogen and raise its temperature to 480°K.

In order to supply the energy to vaporize and heat the hydrogen to 480°K, 1100 pounds of O_2 is needed. This also produces the humidity necessary for droplet formation in the primary flow.

f. Water to Cool and Humidify Secondary Flow

In order to achieve a humidity level around 70% in the secondary flow, 1300 pounds of water is injected into the generators. Porous inner walls of the outer pressure vessel have been chosen as the site of injection to confine the moist area with the highest flow rate region. The flow of this water must be started and stopped in synchronization with the gas flow. It would be stored in a pressurized vessel at 600 psi regulated from a gaseous pressure system.

g. Stacked EFD Cylindrical Generator

A cylindrical generator geometry is used having a stack of radial outflow slit nozzles. The local flow in these nozzles is essentially the two-dimensional geometry used by the Air Force in an experimental study.(g)

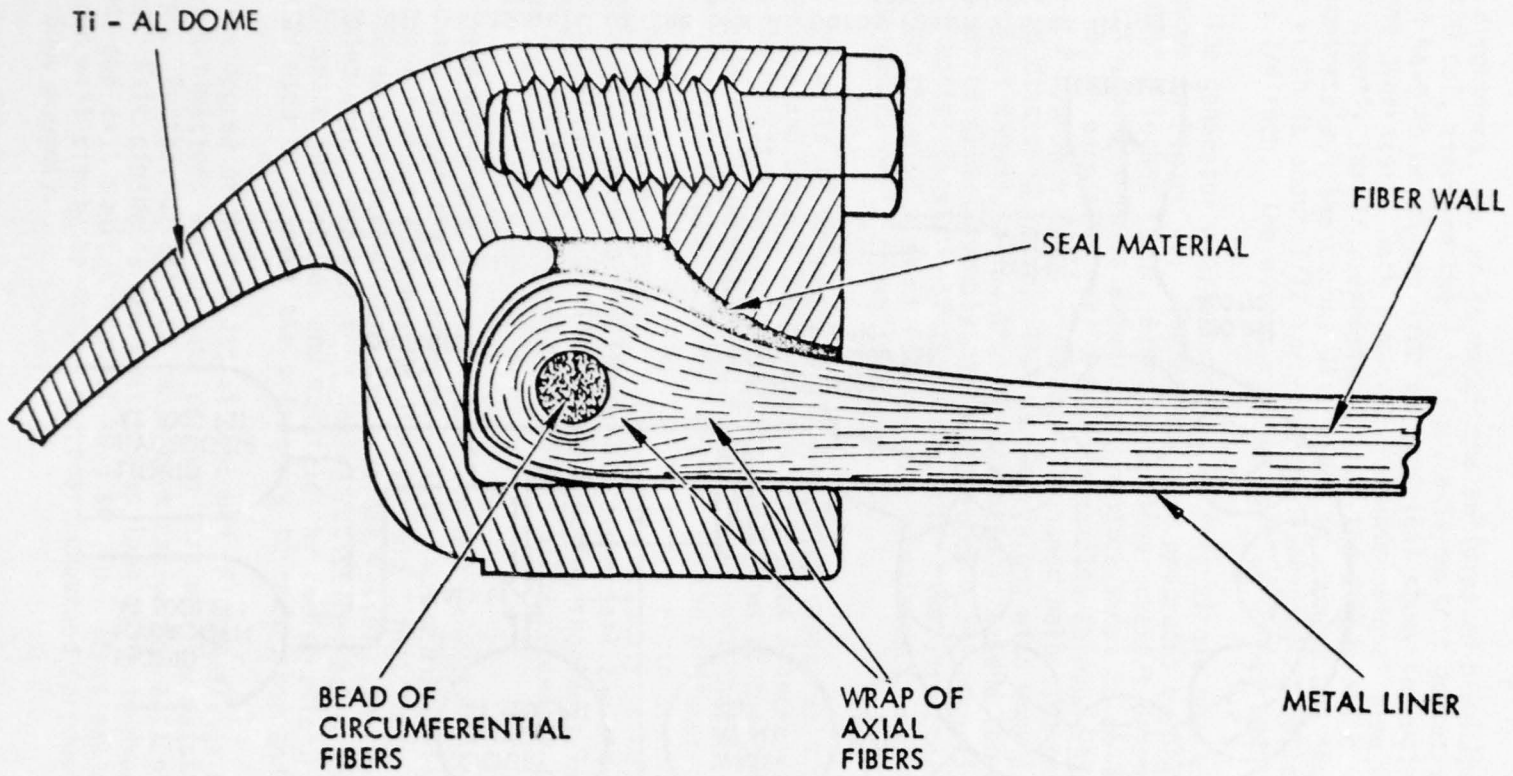

Figure 43. Detail of the Clamping Seal Between the Metal Dome and the Cylindrical Plastic Tank

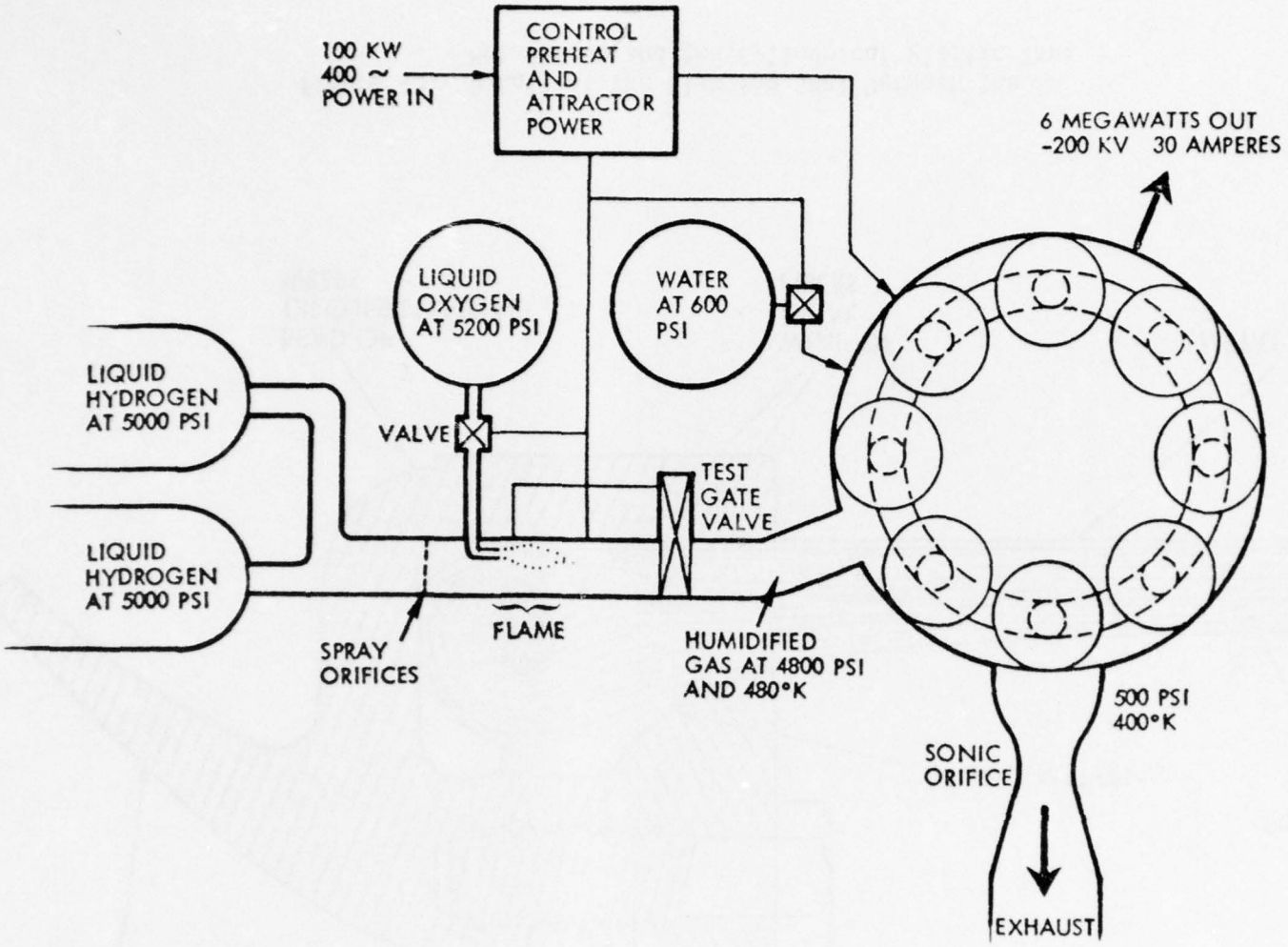

Figure 44. Schematic of the 6MW Airborne Power System Using an EFD Generator Operating with Hydrogen

The dimensions, chosen to match the anticipated breakdown strength of hydrogen at 400 psi, simulate the 1/12 inch axisymmetric geometry. The exact dimensions would have to be chosen from an empirical study conducted on a small portion of the generator. Mach number 2, two-dimensional flow in hydrogen is sufficiently far from experience that the dimensions can only be chosen approximately. The corona disc width is about 0.005 inch. The attractor slit width is about 1/12 inch and the attractor-to-collector distance is about 1/4 inch. The output voltage will be 200 kV and the current 30 amperes.

The generator will be made up of many single nozzle units, one of which is shown in Figure 45. The corona disc protrudes beyond the disc in 3 sections of about 2 inches each. Based on a linear current density of 14 milliampere per inch, each unit is expected to produce about 85 milliamperes. The corona disc has on each side very thin slit nozzles through which the primary Mach number 2 hydrogen flows. The kidney-shaped holes are necessary for secondary flow as discussed later. These holes, along with many internal strengthening welds (not shown), allow the structure to withstand the high internal pressure. In order to allow assembly, each attractor plane (usually separating two nozzle units) consists of three segments. The attractors are positioned as shown in the plan view of Figure 45. A cross-sectional view of a portion of the generator is shown in Figure 46.

Ten units of primary nozzles have been chosen as a basic module. These are welded and brazed together as a unit about 4 inches long. Thirty-three segments of attractor, with spacers and screws at the joints, are put together around the nozzle assembly and form a rigid unit that is later sealed and aligned by insulators. Eleven sections of the diffuser-collector are joined by spacers at the outside diameter to form a rigid assembly that can be slipped over the assembled attractor. The entire assembly is held together between two flat disc insulators. These insulators seal the attractor-to-collector space and align all the elements by indexing shoulders located on the nozzle assembly. Holes in the insulator seals allow secondary flow as shown in Figure 46.

These basic modules would generate 850 μa while requiring approximately 40 modules to get the 30 amperes. Five such modules will be mounted into a pressure can about 9 inches in diameter and 2 feet long. Figure 47 shows how the modules are stacked into the pressure vessel. The modules slip over and are sealed onto a central tube having registered holes to feed the nozzles. Springs space the modules and maintain the registration. The outer spring shown is used to connect the attractors to each other and to the feed-through.

The degree of design detail sketched (Figure 47) is necessary to make weight estimations and to make certain that no flaw exists in the basic concept. Further details of cable termination and exit piping are not discussed. Exit piping is not critical as long as their cross section area exceeds the exit sonic throat of 10.6 sq. in. It is expected that the moist hydrogen will simply be dumped overboard unburned (producing a thrust of about 6000 pounds).

The eight generators would weigh about 400 pounds.

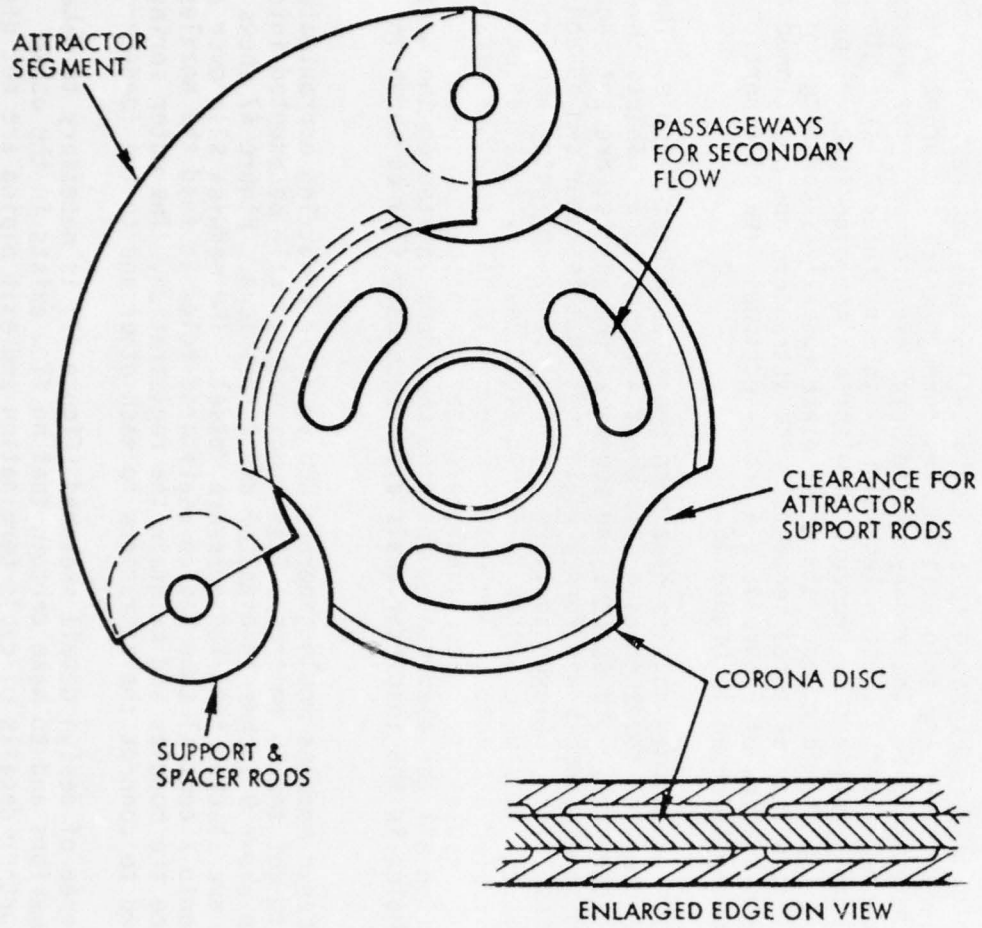

Figure 45. Single Primary Nozzle and Corona Disc

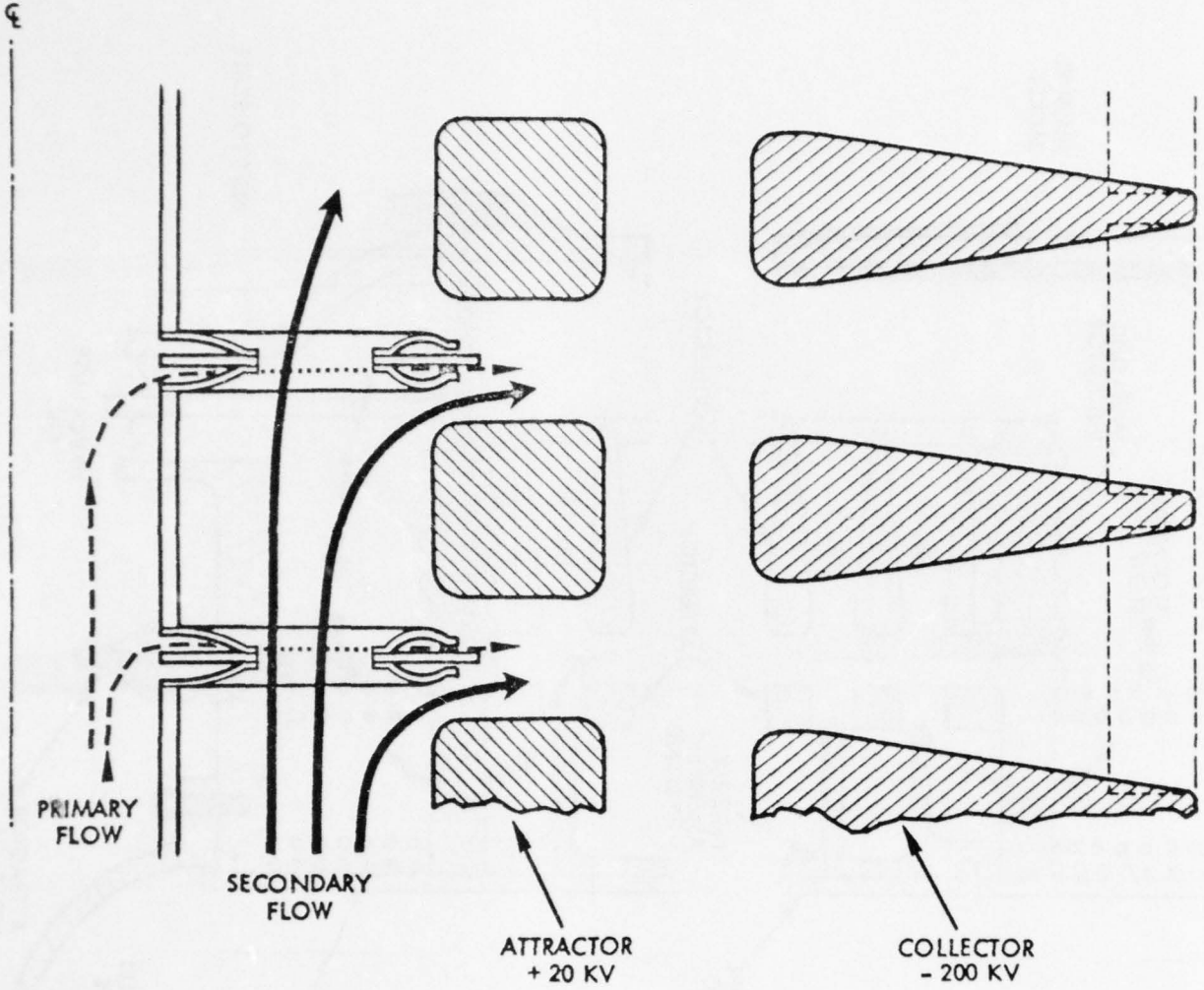

Figure 46. Sketch Showing Arrangement of the Electrodes and the Flow Paths

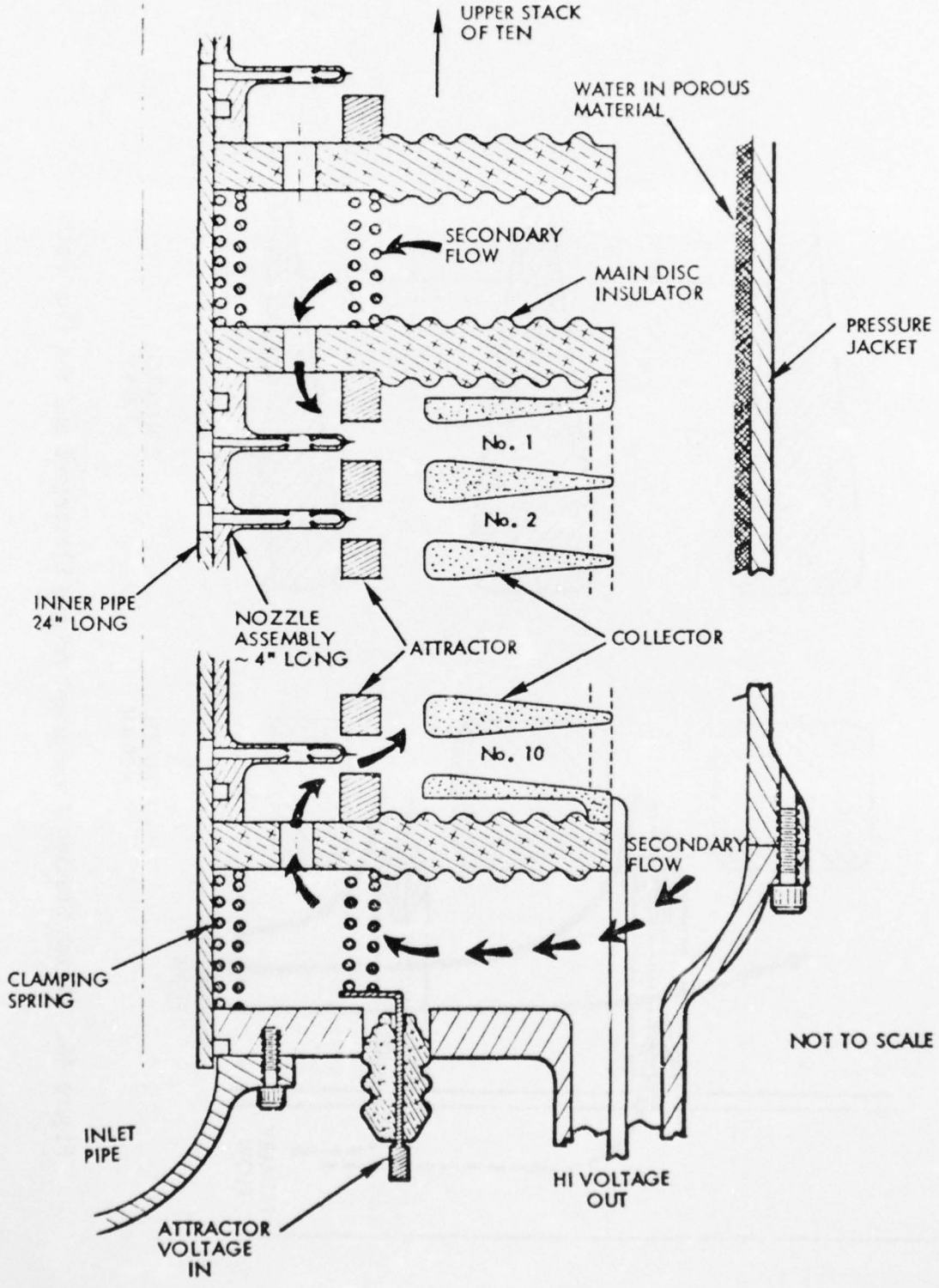

Figure 47. Sketch of the Assembled 6/8MW EFD Generator

h. Overall System - Weight and Volume

A breakdown of system weight and volume follows:

Hydrogen	2840	650
Tank and Insulator	6330	200
Oxygen and Tank	1300	18
Water, Tank, etc.	1350	18
8 Generators	400	25
Pipes and Valves	100	10
Attractor Power Supply and Control (2 lb/kW)	1200 lbs.	20 cu. ft.
	13520 lbs.	931

If twice the assumed 4% enthalpy removal could be achieved (as suggested by the following analysis), the hydrogen and tank weight would be reduced by half, thus reducing the total weight to about 9000 pounds.

If liquid air were used (possibly because of the danger of hydrogen), the system would weigh about 30,000 pounds.

2. GROUND BASED EFD GENERATOR

For a ground based system higher efficiences must be achieved than in the airborne system, and a condensible primary fluid must be used, that lends itself to a Rankine cycle. The best candidate for such a system, and one to which the Air Force has devoted much study, uses mercury as the primary driving fluid and hydrogen as the driven fluid. The reason for this choice is that high Mach numbers in the Hg can be used to convert a large percentage of enthalpy into kinetic energy and yet produce a low velocity that matches that of the low Mach number hydrogen flow. The calculated mixing losses are low for this condition although the necessary mixing length may be very large.

a. Parameters Selected and Assumptions

Mercury at 2500 psia and 1150°K is expanded in a supersonic nozzle to 300 psia without condensing, even though the local temperature is 493°K and the super-saturation ratio is over 500. The mercury molecules mix into a greater area and with a far greater number of hydrogen molecules. The hydrogen is warmed and the mercury is cooled during mixing, without condensation. The Hg atoms will not condense on any of the electrodes, such as the attractor or collector walls, because the walls are warm and are covered with oxides. The mercury modecules should, however, condense on the cool condenser, which is covered with a film of mercury, as rapidly as they can diffuse through the hydrogen.

It is felt that this action of the mercury in the mixed gas is realistic and that to depend on mercury for the colloid charge carrier is not a sound approach. Calculations on nucleation rate show that no amount of chilling

will raise the diluted super-saturation ratio high enough to condense, even on an ion. Therefore, the source of droplets is not resolved at this point. Hopefully, at the time such a system would be built, a system employing permanently dispersed colloids of the proper size and number density would be at hand.*

The secondary hydrogen pressure is 308 psia and the constant pressure in the conversion region is 300 psia. The area ratio between the supersonic mercury nozzles and the constant area mixing region is 0.01. The theoretically derived efficiency for this case is 39%. However, to be conservative, 30% is used for this analysis.

b. Description of Generator

A sketch of the entire 1 kW EFD generator is shown in Figure 48. The ~ 1-foot-diameter pressure vessel is finned on the outside to enhance cooling by air (possible by natural convection). It is also finned on the inside and the fins are aligned with the circulating gas flow to increase the rate of condensation. The vessel is statically filled with 308 psia of hydrogen at an operating temperature of about 70°C. The pressure will vary slightly with the operating temperature, but since gas density determines breakdown strength, there is no need to compensate for this variation. The 8 psi differential pressure remains the same. A few pounds of mercury are added to the system to fill the piping to and from the pump, the bottom of the boiler and the generator, as shown.

Mercury vapor at 2500 psia and 1150°K (1610°F) from the fuel-fired boiler enters from the bottom and is fed to the array of small supersonic nozzles. These nozzles are diverted into the attractor electrodes (that are converged for constant area) where mixing occurs with the circulating hydrogen. Corona from a loop of fine wire at ground potential (produced by the +20 kv of the attractor) negatively charges the colloid particles entrained in the mixed flow. This charged gas then slows down as it traverses the field and enters the diverging duct in the collector. Within the collector, as the gas is decelerated by the 8 psia pressure rise, the electric field caused by space charge builds up and causes the corona points to spray positive charges which neutralize the negative colloids, providing effective collection of negative charges.

As the hydrogen recirculates, it is cooled and mercury is condensed out of it onto the walls. The condensed mercury flows by capillary action down the walls to the bottom of the chamber where it is pumped back into the boiler. The hydrogen reenters the attractor, is accelerated to Mach number 0.2, and mixed with the primary jets of mercury. A reasonable amount of condensed mercury can remain in the hydrogen without impairing the operation of the generator.

c. Unattended Continuous Operation for 1 Year

Assume here that no electricity is available and that 1 kW is desired at 200 kV. A storage battery is selected to run the electric pump and to provide power to the attractor supply and the control system. The battery is charged by electricity converted from the high voltage output. Efficient

* MIT [i] tried a Cesium amd/gam to achieve condensation.

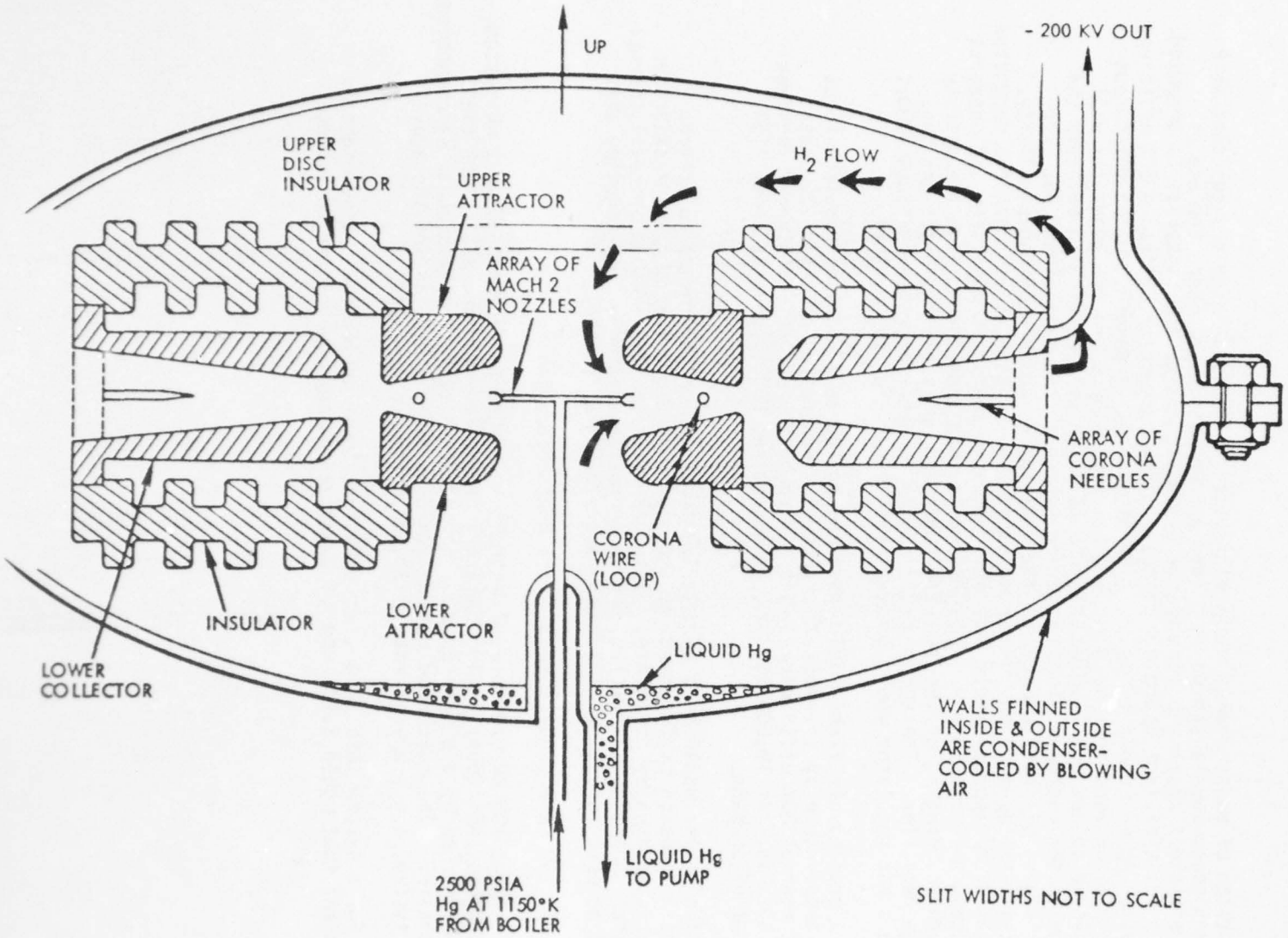

Figure 48. Sketch of 1 KW EFD Generator using Mercury Rankine Cycle Driving Hydrogen

AD-A033 729 TRW DEFENSE AND SPACE SYSTEMS GROUP REDONDO BEACH CAL--ETC F/G 10/2
STUDY ON ELECTROFLUID DYNAMIC POWER GENERATION.(U)
JUL 76 M N HUBERMAN, H SHELTON, W KRIEVE F33615-75-C-4085
UNCLASSIFIED AFAPL-TR-76-31 NL

2 OF 2
AD
A033729

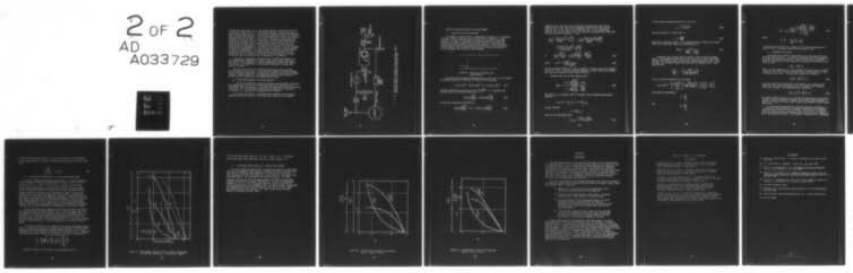

END

DATE
FILMED
2-77

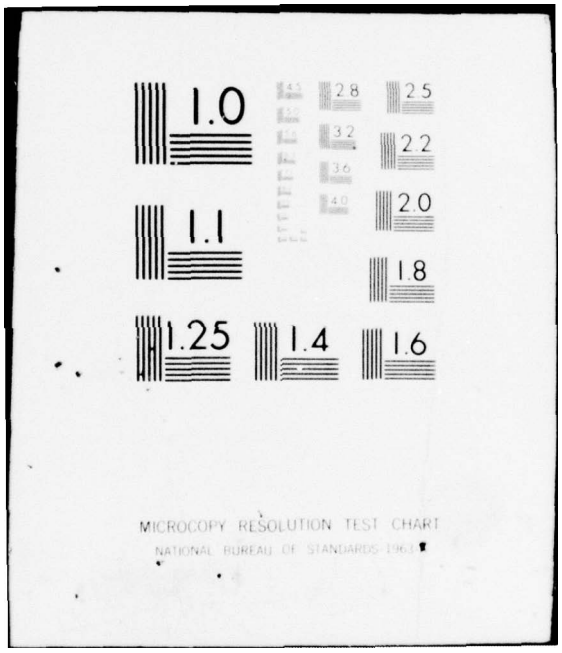
1.0
1.1
1.25
1.4
1.6
2.8
2.5
3.2
2.2
3.6
2.0
4.0
1.8
MICROCOPY RESOLUTION TEST CHART
NATIONAL BUREAU OF STANDARDS-1963

conversion of power from a very high voltage requires large devices that work at high power levels and do not seem appropriate here. Here the use of a less efficient spark-gap conversion system to charge the batteries is proposed. With a 40% efficient charging circuit, a 50% pump-motor system, a 50% efficient attractor power supply (supplying 2% of the output power), 20% of the output power will be used for charging the battery. Therefore the generator will be powered to put out 1250 watts, 250 of which will be used to maintain the charge in the battery. This charging scheme is shown in Figure 49. The major source of inefficiency is the resistor which is used for simplicity. It dissipates as much energy as is stored in the capacitor. When the capacitor charges up to approximately its full voltage, the spark gap fires and connects it across the transformer. The energy is then transferred into the battery through the ringing of the leakage inductance of the transformer and the bridge rectifier. The turns ratio of the transformer would be about 4000:1 and a shunt regulator would prevent overcharging of the battery.

A propane-air flame would heat the boiler to 1150°K and regulate it at that temperature by thermostatic control. Generation of power 1250 watts for 1 year at 30% efficiency (with 80% combustor-boiler efficiency) requires $1.56\ 10^8$ Btu. At 19,500 Btu lb, this requires 8000 pounds or about 1650 gallons of propane.

The boiler would be a simple TZM tube clad on the inside to prevent excessive erosion by the mercury and clad on the outside to prevent oxidation and/or carbiding by the flame. Internal spiral baffling would increase thermal transfer. Careful insulation and regenerative heating of the incoming air would be used to achieve the above assumed 80% efficiency.

d. 100 kW Ground-Package for 6 Month Operation

The 100 kW system would simply be scaled up from the above 1 kW system. One hundred individual 1 kW generators can be fed from one boiler and the fluid returned by a single pump. The output voltage terminals would be connected in parallel. The fuel requirement would be fifty times that of the above 1 kW system, i.e., approximately 80,000 gallons of propane.

For a system this large, an efficient power conversion system might be practical that would allow use of the power at any lower ac or dc voltage.

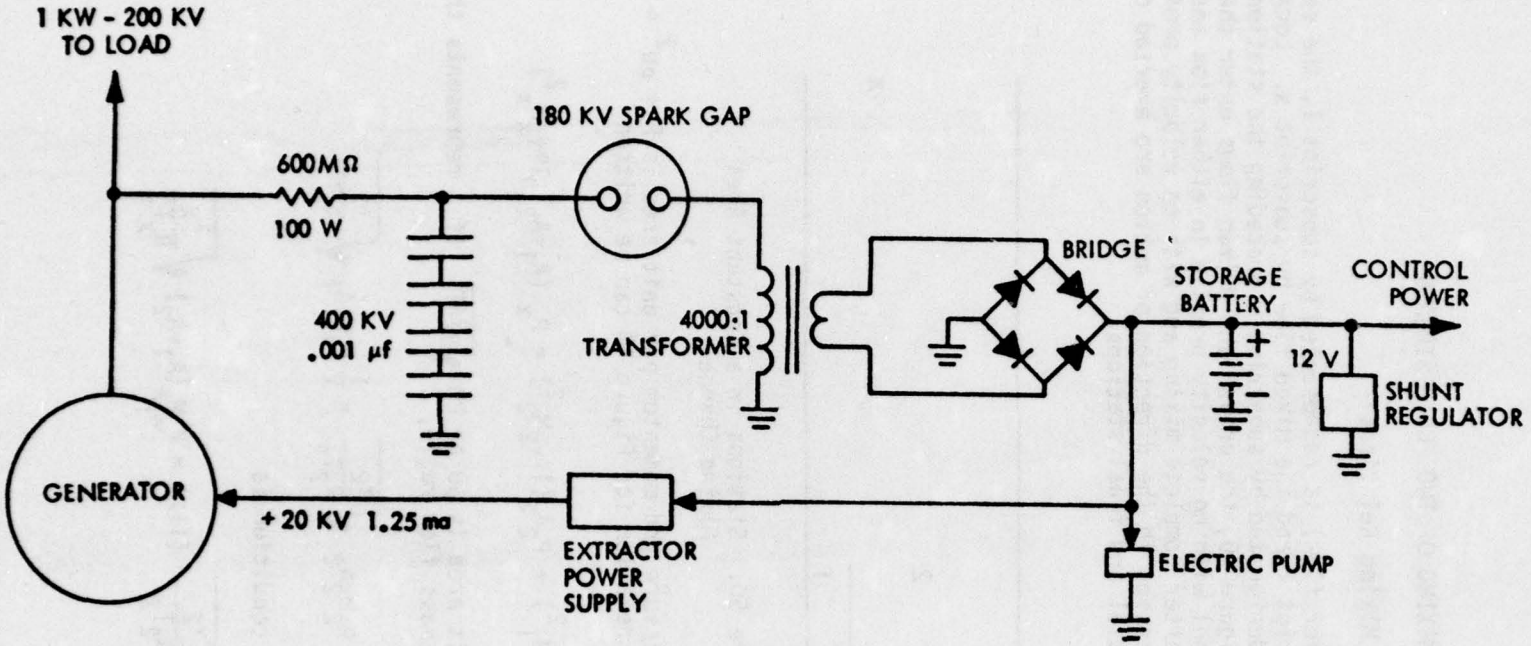

Figure 49. Auxiliary Electric System to Charge Battery Supply, Extractor Power, and Power the Mercury Pump

3. ANALYSIS INVOLVING MIXING OF TWO FLUID STREAMS

a. Constant Area Mixing Relations

The primary (or driver flow) is represented by subscript 1, the secondary (or driven flow) by subscript 2 and the mixed flow by subscript x. Local stagnation variables are designated by subscript s preceding the station subscript. As shown in Figure 50, the driver and driven flows enter the constant area mixing channel with no velocity profile in either flow and leave the mixing channel after complete mixing and with no velocity profile. No body forces or wall stresses in the direction of motion are exerted on the fluid between the initial and final stations.

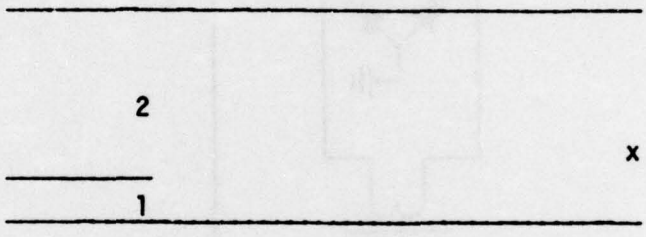

Figure 50. Stations in a Constant Area Mixing Channel

Since the sum of pressure and momentum per unit area is $P + \rho u^2 = P(1+\gamma M^2)$, the momentum conservation relation for Figure 50 can be written

$$P_1 A_1 (1+\gamma_1 M_1^2) + P_2 A_2 (1+\gamma_2 M_2^2) = P_x (A_1+A_2)(1+\gamma_x M_x^2) \qquad (21)$$

The mass flow rate per unit area is ρu or $PM\sqrt{\gamma/RT}$. If λ represents the ratio of driver to driven mass flow ratio,

$$P_2 M_2 A_2 \sqrt{\frac{\gamma_2}{R_2 T_2}} = \frac{1}{\lambda} P_1 M_1 A_1 \sqrt{\frac{\gamma_1}{R_1 T_1}} \qquad (22)$$

and the mass conservation condition is

$$P_2 M_2 A_2 \sqrt{\frac{\gamma_2}{R_2 T_2}} \ (1+\lambda) = P_x M_x (A_1+A_2) \sqrt{\frac{\lambda_x}{R_x T_x}} \qquad (23)$$

Equations (21), and (23) can be combined by dividing the left side of Equation (21) by the left side of Equation (23) and the right side of Equation (21) by the right side of Equation (23). In this operation, Equation (22) is also used so that the numerator and denominator terms have the same subscript throughout. Thus,

$$\left(\frac{\lambda}{1+\lambda}\right) \frac{P_1 A_1 (1+\gamma_1 M_1^2)}{P_1 A_1 M_1} \sqrt{\frac{R_1 T_1}{\gamma_1}} + \left(\frac{1}{1+\lambda}\right) \frac{P_2 A_2 (1+\gamma_2 M_2^2)}{P_2 A_2 M_2} \sqrt{\frac{R_2 T_2}{\gamma_2}}$$

$$= \frac{P_x (A_1+A_2)(1+\gamma_x M_x^2)}{P_x (A_1+A_2) M_x} \sqrt{\frac{R_x T_x}{\gamma_x}}$$

or

$$\left(\frac{\lambda}{1+\lambda}\right) \frac{\sqrt{R_1 T_{s1}}}{\mu(M_1)} + \left(\frac{1}{1+\lambda}\right) \frac{\sqrt{R_2 T_{s2}}}{\mu(M_2)} = \frac{\sqrt{R_x T_{sx}}}{\mu(M_x)} \tag{24}$$

where

$$\mu(M) \equiv \frac{M \sqrt{\gamma}}{(1+\gamma M^2) \sqrt{T/T_s}} \tag{25}$$

and the customary notation is used to represent pressure density and temperature as P, ρ and T, velocity and Mach number as μ and M, area as A, and the gas constant and specific heat ratio as R and γ.

Equation (24) can be rearranged to give

$$\mu(M_x) = \frac{(1+\lambda) \sqrt{\frac{R_x T_{sx}}{R_2 T_{s2}}} \mu(M_2)}{1 + \lambda \sqrt{\frac{R_1 T_{s1}}{R_2 T_{s2}}} \frac{\mu(M_2)}{\mu(M_1)}} \tag{26}$$

The term $R_x T_{sx}$ in Equation (26) is obtained from the energy conservation equation

$$\lambda C_{p1} T_{s1} + C_{p2} T_{s2} = (1+\lambda) C_{px} T_{sx}$$

and the relation

$$R = \left(\frac{\gamma-1}{\gamma}\right) C_p$$

which can be combined to give

$$R_x T_{sx} = \frac{\lambda R_1 T_{s1} + R_2 T_{s2}}{1+\lambda} \tag{27}$$

A similar mass averaging procedure is used for γ:

$$\gamma_x = \frac{\lambda \gamma_1 + \gamma_2}{1 + \lambda} \tag{28}$$

The gas constant R, in MKS units is

$$R = \frac{8315}{MW} \tag{29}$$

where MW is molecular weight. The average molecular weight of the mixed flow is the total mass flow rate of molecules, or

$$(MW)_x = \frac{\lambda + 1}{\frac{\lambda}{(MW)_1} + \frac{1}{(MW)_2}} \tag{30}$$

Equations (26) through (30) are used to find the mixed flow Mach number. The stagnation pressure for the mixed flow is then found from a relation involving M_x that is obtained by combining Equations (21), (22) and (23) in a different manner than that used for Equation (26). From Equation (22)

$$\frac{P_1 A_1}{P_2 A_2} = \lambda \frac{M_2}{M_1} \sqrt{\frac{R_1 T_1}{R_2 T_2}} \sqrt{\frac{\gamma_2}{\gamma_1}}$$

This is used with Equation (21) to obtain

$$P_x(1+\gamma_x M_x^2) = \frac{P_2(1+\gamma_2 M_2^2)}{(1 + \frac{A_1}{A_2})} \left[1+\lambda \sqrt{\frac{R_1 T_1}{R_2 T_2}} \sqrt{\frac{\gamma_2}{\gamma_1}} \frac{(1+\gamma_1 M_1^2)}{(1+\gamma_2 M_2^2)} \frac{M_2}{M_1} \right]$$

Then from the tantologies

$$T_s = \frac{T}{\frac{T}{T_s}}$$

and

$$P_s = \frac{P}{\frac{P}{P_s}}$$

$$P_{sx} = P_{s2} \frac{P_s(M_x)}{P_s(M_2)} \frac{\left[1+\lambda\sqrt{\frac{R_1T_{s1}}{R_2T_{s2}}}\ \frac{\mu(M_2)}{\mu(M_1)}\right]}{\left(1+\frac{A_1}{A_2}\right)} \tag{31}$$

where

$$P_s(M) \equiv \frac{1}{\left(\frac{P}{P_s}\right)(1+\gamma M^2)}$$

In performing calculations it is useful to note that the denominator of Equation (26) is the square bracket term of Equation (31).

b. Generator Efficiency

One dimensional, uniform, flow conditions are also assumed for the generator working section. In addition, the working section is assumed to be an open jet such that pressure is constant during power extraction. Therefore, deceleration of the mixed flow is due only to the electric body force, so that

$$udu = -\frac{qE}{\rho}\,dx$$

where x is axial position, E is local electric field and q and ρ are local charge per unit volume and mass per unit volume, respectively (i.e., q/ρ) is charge per unit mass. The acceleration equation is therefore

$$d\left(\frac{1}{2}u^2\right) + \frac{qE}{\rho}\,dx = 0 \tag{32}$$

The energy conservation condition is that electric work is done at the expense of local stagnation enthalpy (i.e., the sum of local enthalpy plus kinetic energy). The energy equation is therefore

$$d\left(C_pT + \frac{1}{2}u^2\right) + \frac{qE}{\rho}\,dx = 0 \tag{33}$$

By combining these equations it is seen that the temperature (and therefore the density also) is constant throughout the constant pressure working section. Consequently electric work is done at the expense of local kinetic energy only.

In the present one-dimensional estimate of generator efficiency, it is assumed that the colloids are introduced, charged and mixed uniformly while the driver and driven flows are mixing. The ratio q/ρ is then regarded as constant across the generator working section and the integral of Edx is the generator voltage V. The integral of Equation (33) is therefore

$$\frac{qV}{\rho} = C_{px} (T_{sx1} - T_{sx2}) \tag{34}$$

where x_1 and x_2 refer to the working section inlet and exit conditions.

The efficiency of conversion of primary flow stagnation enthalpy to electric work is defined as

$$\eta = \frac{(1+\lambda)\, C_{px} (T_{sx1} - T_{sx2})}{\lambda\, C_{p1}\, T_{s1}} \tag{35}$$

and is referred to as generator efficiency.

Since $C_p = \frac{\gamma}{\gamma-1} R$, and R is inversely proportional to molecular weight, Equation (35) can be written

$$\eta = \left(\frac{1+\lambda}{\lambda}\right) \left(\frac{\gamma_x}{\gamma_1}\right) \left(\frac{\gamma_1-1}{\gamma_x-1}\right) \left(\frac{MW_1}{MW_x}\right) \left(\frac{T_{sx1}}{T_{s1}} - \frac{T_{sx2}}{T_{s1}}\right) \tag{36}$$

From Equation (34) and (35), the electric work parameter can be written non-dimensionally as

$$\frac{\left(\frac{qV}{\rho}\right)}{C_{p1}\, T_{s1}} = \left(\frac{\lambda}{1+\lambda}\right) \eta \tag{37}$$

c. Analysis of Experiments

The one-dimensional analysis procedure is to assume uniform flow in the driver and driven streams which correspond to isentropic expansion from their respective plenum conditions. The measured electrical power is subtracted from the stagnation enthalpy flow rate of the driver stream and pressure rise is calculated that brings the mixed flow leaving the generator to rest such that the final pressure is equal to the initial driven flow stagnation pressure. The ratio of this pressure rise to that corresponding to isentropic deceleration of the flow leaving the generator defines an overall diffuser loss coefficient η_D that accounts for all nonideal losses such as open-jet mixing losses in the working section, diffuser losses and departure from uniform one-dimensional conditions everywhere.

The first case is a high driver Mach number test conducted at WPAFB. The primary Mach number was 1.61 and the secondary Mach number was 0.45. The pressures of both streams at the beginning of constant area mixing were 270 psia and the stagnation temperatures of both streams were 340°K. The electrical power output was 30 watts, corresponding to 5% of the stagnation enthalpy flow rate of the primary stream. Air was used for both the driver and driven flows.

From the power measurement, the mass flow rate is

$$\dot{m}_1 = \frac{30}{0.05\, C_p\, T_{s1}}$$

Also, for one-dimensional flow,

$$\dot{m}_1 = \frac{P_1\, A_1\, M_1 \sqrt{\frac{\gamma_1}{R_1\, T_{s1}}}}{\sqrt{\frac{T_1}{T_{s1}}}}$$

Therefore the effective one-dimensional flow area of the driver flow was 1.27×10^{-7} M^2. With this area known, and using the measured mixing channel diameter of 0.083 inch, the driven flow area was 3.36×10^{-6} M^2 and $A_1/A_2 = 0.0379$ for this experiment. The mass flow ratio was consequently, from Equation (22), $\lambda = 0.164$. Then, from Equation (26), $\mu(M_{x1}) = 0.433$ and $M_{x1} = 0.47$, where the subscript x1 refers to the mixed flow conditions at the generator working section inlet. From Equation (31)

$$\frac{P_{sx1}}{P_{s2}} = 1.083$$

exit conditions (after power extraction) are determined by the measured efficiency.

For this case, γ, T_s and molecular weight are the same for both streams and are not affected by mixing. Thus $T_{sx1} = T_{s1}$. After power extraction T_{sx2}/T_{s1} is calculated from Equation (36) to be

$$\frac{T_{sx2}}{T_{s1}} = 1 - \eta \left(\frac{\lambda}{1+\lambda}\right) = 0.9930$$

Thus, for this case,

$$\frac{T_{x2}}{T_{sx2}} = \frac{\frac{T_{x1}}{T_{sx1}}}{\frac{T_{sx2}}{T_{s1}}} = \frac{0.9577}{0.9930} = 0.9645$$

and $M_{x2} = 0.43$. The diffuser efficiency is then found to be

$$\eta_D \equiv \frac{P_{s2} - P_{x2}}{P_{sx2} - P_{x2}} = \frac{\frac{P_{s2}}{P_{sx2}} - \frac{P_{x2}}{P_{sx2}}}{1 - \frac{P_{x2}}{P_{sx2}}}$$

Because the working section pressure is constant, this can be written in terms of the known Mach number functions,

$$\eta_D = \frac{\left(\frac{P_{x2}/P_{sx2}}{P_{x1}/P_{sx1}}\right)\left(\frac{P_{s2}}{P_{sx1}}\right) - \frac{P_{x2}}{P_{sx2}}}{1 - \frac{P_{x2}}{P_{sx2}}}$$

It is found that

$$\eta_D = \frac{\left(\frac{.8807}{.8596}\right)(.9236) - .8807}{1 - .8807} = 0.55$$

From Equation (37), the dimensionless electric work parameter was

$$\frac{\frac{qV}{\rho}}{C_p T_{s1}} = \left(\frac{\lambda}{1+\lambda}\right)\eta = \left(\frac{.164}{1.164}\right)(.05) = 7.04 \times 10^{-3}$$

For air, $C_p = 1004$, and with $T_{s1} = 340°K$,

$$\frac{qV}{\rho} = 2400$$

For the second experimental case, the driver Mach number was 1.0 (a simple convergent nozzle was used). Based on measured plenum pressures and secondary flow wall pressure at the injection station, the driven flow Mach number was 0.65 while the driver flow Mach number was 1.27. This is interpreted as an underexpanded driver nozzle flow with $P_1/P_2 = 1.41$. The mass flow ratio was 0.71 and the area ratio was $A_1/A_2 = 0.333$. The initial and final mixed flow Mach numbers were 0.69 and 0.65, respectively. The generator efficiency was 2.2% and the electric work parameter was 2930. The diffuser efficiency calculated for this case was 0.42.

These two cases give lower values of equivalent diffuser efficiency than the value of 0.6 calculated from a third set of experimental data.[h]

d. Performance Calculation Procedure

It is assumed for the following calculations, that $\eta_D = 0.55$ can be used to represent the losses due to flow non-uniformities and viscous effects. The following procedure can then be used to calculate the performance of any EFD machine.

The input parameters are molecular weight and γ of the two fluids, the area ratio A_1/A_2, and the driver and driven flow Mach numbers. The mass flow ratio is then calculated by the following rearrangement of Equation (22)

$$\lambda = \frac{M_1}{M_2} \frac{\sqrt{\frac{T_2}{T_{s2}}}}{\sqrt{\frac{T_1}{T_{s1}}}} \sqrt{\frac{\gamma_1 R_2 T_{s2}}{\gamma_2 R_1 T_{s1}}} \quad \frac{A_1}{A_2} \tag{38}$$

in which P_1 is assumed equal to P_2. The mixed flow molecular weight is calculated from Equation (30)

$$(MW)_x = \frac{\lambda+1}{\frac{\lambda}{(MW)_1} + \frac{1}{(MW)_2}} \tag{30}$$

and the mixed flow value of γ is found from Equation (28)

$$\gamma_x = \frac{\lambda \gamma_1 + \gamma_2}{1+\lambda} \tag{28}$$

The stagnation temperature ratio relative to the driven flow is then calculated from the following rearrangement of Equation (27) combined with Equation (29),

$$\frac{T_{sx1}}{T_{s2}} = \frac{\frac{(MW)_x}{(MW)_2} + \lambda \frac{(MW)_x}{(MW)_1}}{1+\lambda} \tag{39}$$

Then the initial mixed flow Mach number is found from Equation (26), combined with Equation (29),

$$\mu(M_{x1}) = \frac{(1+\lambda)\sqrt{\frac{(MW)_2}{(MW)_x}\frac{T_{sx1}}{T_{s2}}}\,\mu(M_2)}{1+\lambda\sqrt{\frac{(MW)_2}{(MW)_1}\frac{T_{s1}}{T_{s2}}}\,\frac{\mu(M_2)}{\mu(M_1)}} \tag{40}$$

$$\mu(M_{x1}) \equiv \frac{M_{x1}\sqrt{\gamma_{x1}}}{\left(1+\gamma_{x1}M_{x1}^2\right)\sqrt{\frac{T_{x1}}{T_{sx1}}}} \tag{25}$$

is used to find M_{x1} from the calculated value of $\mu(M_{x1})$. The ratios T_{x1}/T_{sx1} and P_{x1}/P_{sx1} are then computed from the well known Mach number functions

$$\frac{T_{x1}}{T_{sx1}} = \left[1+\left(\frac{\gamma_{x1}-1}{2}\right)M_{x1}^2\right]^{-1} \tag{41}$$

and

$$\frac{P_{x1}}{P_{sx1}} = \left[1+\left(\frac{\gamma_x-1}{2}\right)M_{x1}^2\right]^{-\frac{\gamma_{x1}}{\gamma_{x1}-1}} \tag{42}$$

The mixed flow stagnation pressure relative to that of the driven flow is then found by use of Equation (31).

$$\frac{P_{sx1}}{P_{s2}} = \frac{P_s(M_{x1})}{P_s(M_2)} \frac{\left[1+\lambda\sqrt{\frac{(MW)_2}{(MW)_1}\frac{T_{s1}}{T_{s2}}}\,\frac{\mu(M_2)}{\mu(M_1)}\right]}{\left(1+\frac{A_1}{A_2}\right)} \tag{43}$$

The definition of diffuser efficiency

$$\eta_D \equiv \frac{\frac{P_{s2}}{P_{sx2}} - \frac{P_{x2}}{P_{sx2}}}{1 - \frac{P_{x2}}{P_{sx2}}}$$

can be rearranged to give

$$\frac{P_{x2}}{P_{sx2}} (\eta_D - 1) = \eta_D - \frac{P_{s2}}{P_{sx2}} \tag{44}$$

But, for $P_{x1} = P_{x2}$ (in the constant pressure working section),

$$\frac{P_{s2}}{P_{sx2}} = \frac{\frac{P_{x2}}{P_{sx2}}}{\frac{P_{x1}}{P_{sx1}} \frac{P_{sx1}}{P_{s2}}} \tag{45}$$

Combining Equations (44) and (45) gives

$$\frac{P_{x2}}{P_{sx2}} = \frac{\eta_D}{\frac{1}{\frac{P_{x1}}{P_{sx1}} \frac{P_{sx1}}{P_{s2}} - (1-\eta_D)}} \tag{46}$$

which is then used to find M_{x2} according to Equation (43) with subscripts 2 and the corresponding temperature ratio T_{x2}/T_{sx2}. Equation (36) can then be used to find the generator efficiency,

$$\eta = \left(\frac{1+\lambda}{\lambda}\right) \left(\frac{\gamma_x}{\gamma_1}\right) \left(\frac{\gamma_1 - 1}{\gamma_x - 1}\right) \left(\frac{MW_1}{MW_x}\right) \frac{T_{sx1}}{T_{s1}} \left[1 - \frac{\frac{T_{x1}}{T_{sx1}}}{\frac{T_{x2}}{T_{sx2}}}\right] \tag{36}$$

which has used the fact that $T_{x1} = T_{x2}$ in the generator working section. Finally Equation (37) is used to calculate the dimensionless electric work term

$$\frac{\frac{qV}{o}}{C_p T_{s1}} = \left(\frac{\lambda}{1+\lambda}\right) \eta \qquad (37)$$

e. Calculated Efficiencies for a Mercury/Hydrogen System

Figure 51 shows the performance characteristics of an EFD generator having a mercury driver jet at Mach number 2 and T_{s1} = 1150°K, with a driven flow at T_{s2} = 320°K. The efficiency, electric work term and working section area ratio are shown for the possible range of driven flow mach numbers for A_1/A_2 = 0.01 and 0.02. Within the range of Mach numbers shown, for each area ratio, the electric power extraction and stagnation pressure losses are such that the diffuser exit pressure is just equal to the driven flow stagnation pressure. At the lower limit of this range the working section area ratio approaches infinity as the exit Mach number approaches zero (i.e., the flow is brought to rest by the electric body force). At the upper limit of the available Mach number range the diffuser exit pressure has dropped to the secondary flow plenum pressure with no power extraction and the generator efficiency is zero.

The maximum theoretical generator efficiency occurs when the flow in the working section has been brought to rest. Some efficiency loss must be accepted in order to reduce the area ratio to an acceptable value. If a value of 1.5 is used as a criterion, the generator efficiency for the area ratio 0.01 case drops from the maximum value of 41.7% to 39%. For the more compact, area ratio 0.02 configuration, at the same working section area ratio, the efficiency is 34.5% as compared to its maximum value of 36.9%.

A practical difficulty, not treated in this one pre-dimensional flow analysis, should be noted for the case of high temperature, high Mach number mercury driving low temperature, low Mach number hydrogen. This is that velocities of the two streams are nearly equal so that mixing in a reasonable flow length may not be feasible. The velocity ratio can be expressed as

$$\frac{v_1}{v_2} = \frac{M_1}{M_2}\sqrt{\frac{\gamma_1}{\gamma_2}\,\frac{MW_2}{MW_1}\,\frac{T_{s1}}{T_{s2}}\left(\frac{\frac{T_1}{T_{s1}}}{\frac{T_2}{T_{s2}}}\right)}$$

Another criterion is the electric work parameter which is:

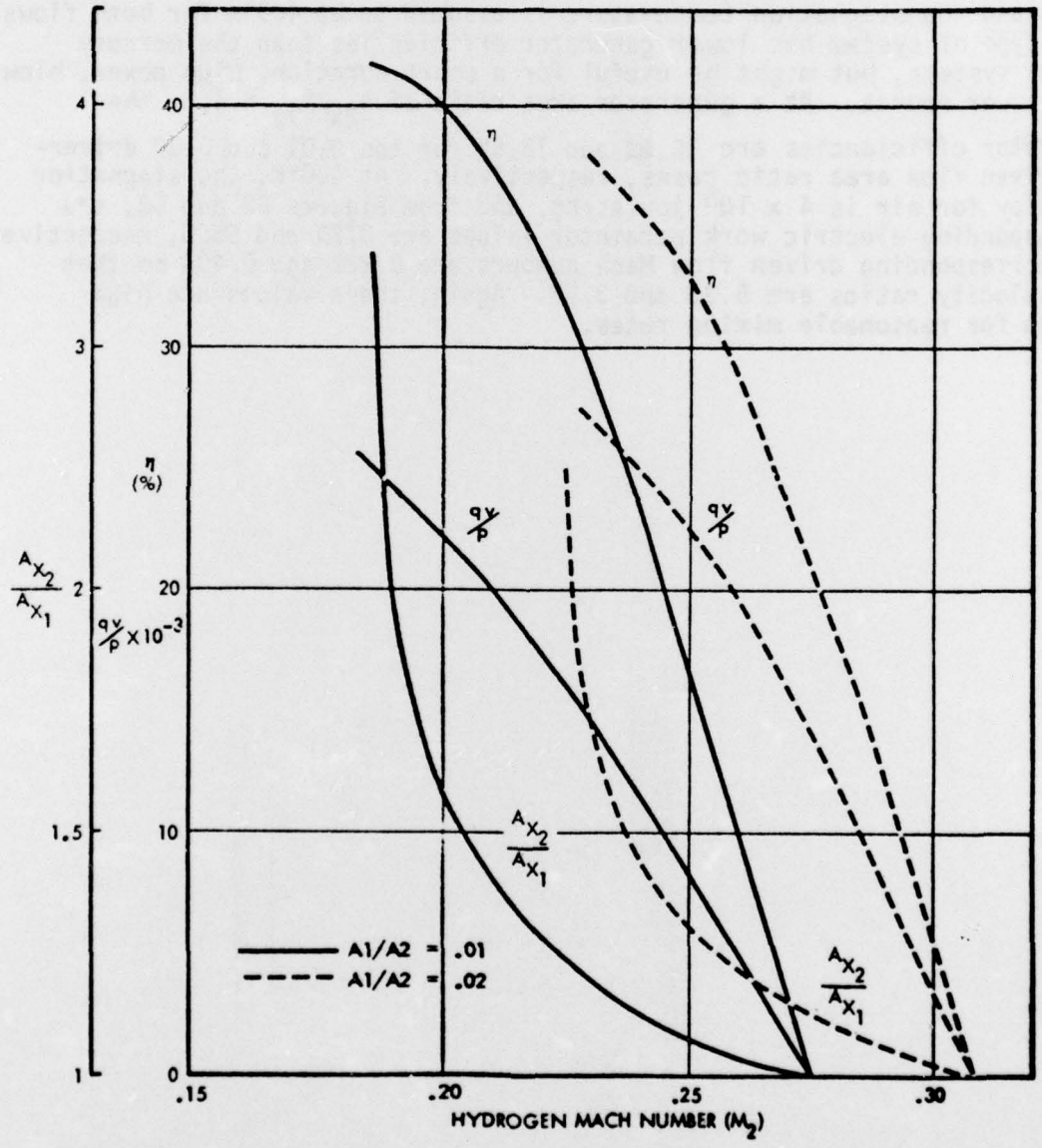

Figure 51. Mach Number 2 Mercury Driver, Hydrogen Driven Flow, For Two Area Ratios (T_{s1} = 1150°K, T_{s2} = 320°K)

For the 0.01 area ratio case (M_1 = 2.0, M_2 = 0.203), v_1/v_2 = 1.30 while for the 0.02 area ratio case (M_1 = 2.0, M_2 = 0.237), v_1/v_2 = 1.11.

f. Calculated Efficiencies for a Single Fluid System

For this system the same fluid is used for both the driver and driven flows and the stagnation temperature is assumed to be 400°K for both flows. This type of system has lower generator efficiencies than the mercury driver systems, but might be useful for a short duration, high power, blow-down power source. At a generator area ratio of A_{2x}/A_{1x} = 1.5, the generator efficiencies are 10.8% and 13.5% for the 0.01 and 0.02 driver-to-driven flow area ratio cases, respectively. At 400°K, the stagnation enthalpy for air is 4 x 10^5 joules/kg, and from Figures 52 and 53, the corresponding electric work parameter values are 3720 and 6560, respectively. The corresponding driven flow Mach numbers are 0.282 and 0.404 so that the velocity ratios are 5.33 and 3.75. Again, these values are high enough for reasonable mixing rates.

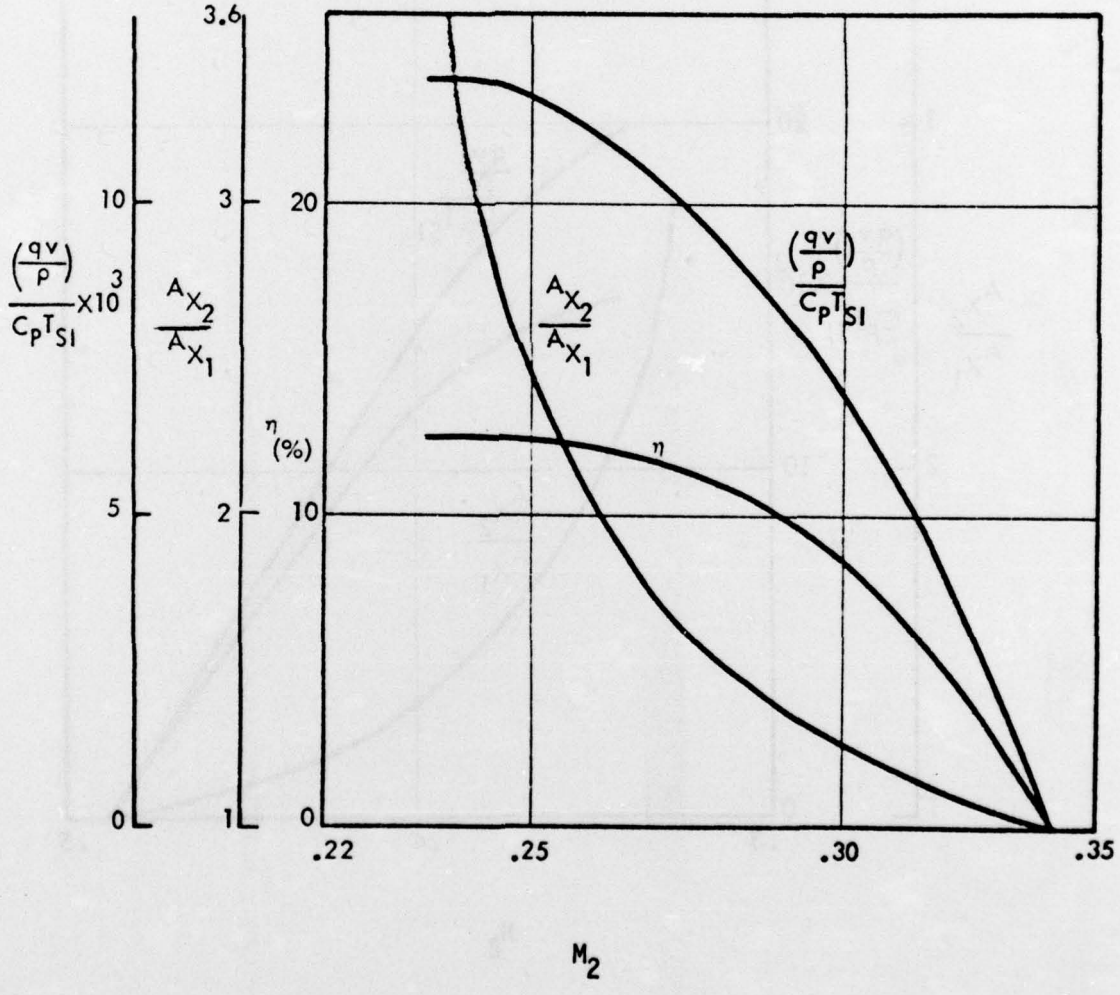

Figure 52. Performance of Single Fluid Generator (A_1/A = 0.01, γ = 1.4)

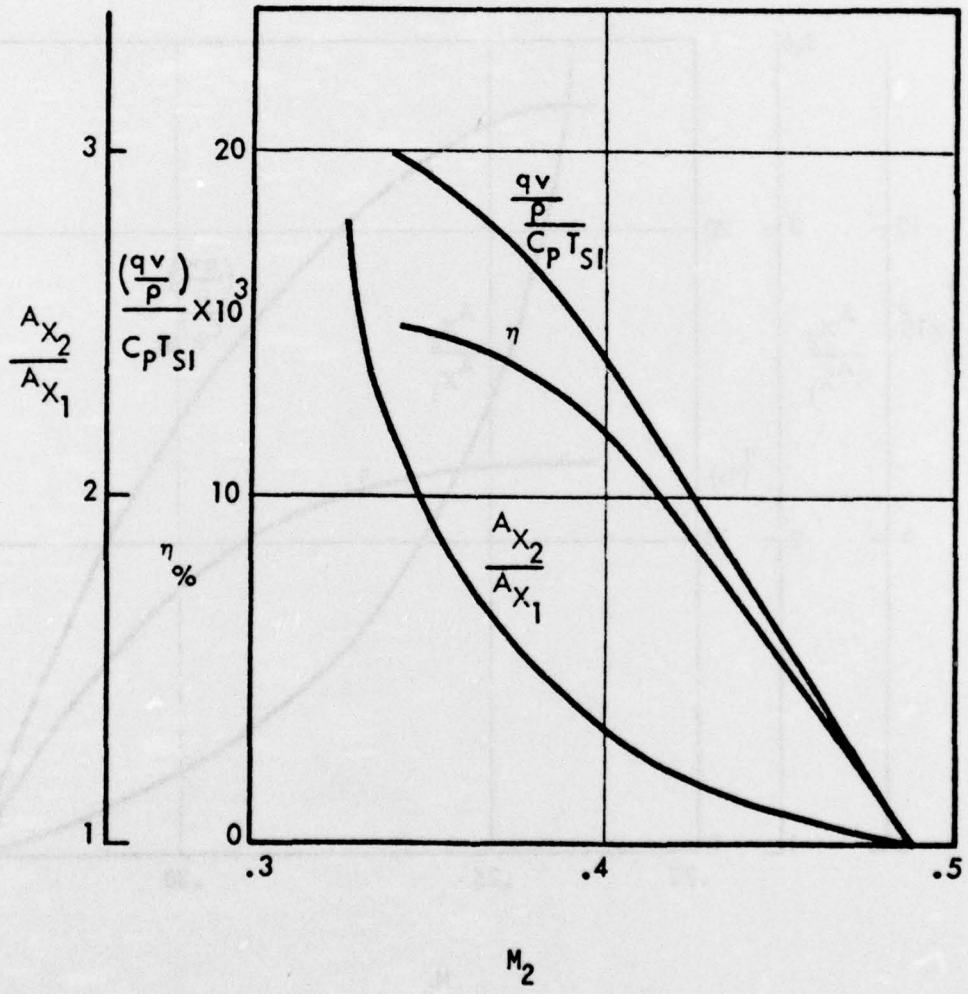

Figure 53. Performance of Single Fluid Generator (A_1/A_2 = 0.02, γ = 1.4)

SECTION VI

CONCLUSIONS

The experimental work in this study was performed with an axisymmetrical EFD generator using air as the working fluid and water for the charge carriers. The study developed a better understanding of the mechanisms of operation. The details of the droplet nucleation, growth and charging are understood and the droplet size and densities are known. The role of the less than linear increase of air breakdown strength as the gas pressure is increased beyond 400 psia is explained. The aerodynamic losses associated with the mixing of the three flows in this type of generator are better understood through comparison of the experiments with analysis.

This basic understanding has exposed limitations that prevent the present EFD generator system from becoming an efficient device to convert thermal power to electrical power. These are

1) Operation is restricted to low gas temperatures, thus limiting the energy available for conversion.

2) Of this low available energy, a Mach number 1 expansion converts only a small portion to kinetic energy.

3) A large fraction of this low kinetic energy is lost by aerodynamic mixing associated with the free-jet generator working section that must be used because solid insulating duct walls cannot support the required high field strengths.

4) Little of the remaining kinetic energy can be converted to electricity because the electrical body force acting on the gas is limited by the maximum electrical fields that can be applied without breakdown of the gas.

These factors allow the EFD generator using Mach number 1 air near room temperature to extract as electricity only a few percent of the heat energy of the gas. Improvement is achieved on point (2) above by increasing the Mach number. Analysis indicates about 10% enthalpy extraction is possible at Mach number 2. Improvement on all the above points may be achieved by using high temperature mercury vapor expanding at Mach number 2 into cooled recirculating hydrogen gas. Analysis indicates this system is capable of over 30% enthalpy extraction. This system, however, has had less experimental study than the Mach number 1 air/water generator. Analyses presented here indicate the production of charged mercury colloid carriers of the proper mobility will be difficult.

LIST OF RECENT A. F. SPONSORED

EFD REPORTS

Huberman, M. N., et al., "Study on Electrofluid Dynamic Power Generation", ARL TR 74-0119, Oct 1974, Aerospace Research Laboratories, WPAFB, Ohio.

Huberman, M. N., et al., "Study on Electrofluid Dynamic Power Generation", ARL TR 75-0200, June 1975, Aerospace Research Laboratories, WPAFB, Ohio.

Minardi, J. E., and Bauer, P. T., "Computer Studies of Electrofluid Dynamic Generators", ARL TR 75-0138, June 1975, Aerospace Research Laboratories, WPAFB, Ohio.

Solbes, A., "Research On Charged Alkali Colloids for Aerospace Vehicle and Ground Based Power Generators", ARL TR 74-0125, Oct. 1974, ARL TR 75-0004, Jan 1975, Aerospace Research Laboratories, WPAFB, Ohio.

Lawson, M. O., et al., "Report on Progress in Achieving Direct Conversion of a major Fraction of Sonic Flow Kinetic Power into Electric Power by Electrofluid Dynamic (EFD) Processes", 9th Inter-Society Energy Conversion Engineering Conference, San Francisco, Cal., Aug. 1974.

BIBLIOGRAPHY

(a) Lawson, M. and Von Ohain, H. Journal of Engineering for Power, Pg 205, Apr. 1971

(b) G. D. Stein and P. P. Wegener, J. Chem. Phys. 46, 3685 (1967)

(c) Reid, R. C. and Sherwood, T. K., The Properties of Gases and Liquids, 2nd Ed., p377, McGraw-Hill, New York, 1966

(d) Hirth, J. P. and Pound, G. M., Progress in Materials Science, Vol. II-Condensation and Evaporation, Nucleation and Growth Kinetics, MacMillan Co., New York, 1963

(e) Hill, P. G., "Condensation of Water Vapor During Supersonic Expansion in Nozzles", J. Fluid Mech, Vol. 25, part 3, pp 593, 1966

(f) A du Pont synthetic fiber.

(g) Griffith, R. W. "Experimental Charge Production in a 2-D EFD Generator" ARL-TR-74-0002

(h) Ernest Fretter, Universal Energy Systems, Inc., Private Communication

(i) ARL TR 75-0004

☆ U. S. GOVERNMENT PRINTING OFFICE: 1976 — 757-001/61